Localized Surface Plasmon Resonance and Vibrational Spectroscopic Study of Trenbolone Acetate Dopant Towards Its Rapid and Label-free Detection

Degree: Doctor of Philosophy (PhD)

Duration: (2020/2021 – 2023/2024)

HEI: University of South Africa

Partner Institution: iThemba-Labs-National Research Foundation of South Africa

Applicant: Juma Moses Wabwile

Student No: 14799642

Supervisors: **Date & Signature**

1. Prof. Malik Maaza

   Supervisor

2. Prof. Simon Mokhotjwa Dhlamini

   Co-Supervisor

@ Nov 2024

DECLARATION

Name:	JUMA MOSES WABWILE
Student Number:	14799642
Degree:	PhD in Physics

The exact wording of the title of the thesis as appearing on the electronic copy submitted for examination:

“**Localized Surface Plasmon Resonance and Vibrational Spectroscopic Study of Trenbolone Acetate Dopant Towards its Rapid and Label-free Detection**”

I declare that the above thesis is my work and that all the sources that I have used or quoted have been indicated and acknowledged using complete references.

I further declare that I submitted the thesis to originality-checking software and that it falls within the accepted requirements for originality.

I further declare that I have not previously submitted this work, or part of it, for examination at Unisa for another qualification or at any other higher education institution.

(*The thesis will not be examined unless this statement has been submitted.)*

PhD Fellow Date & Signature

Moses Wabwile Juma

Dedication

To:

- My wife Esther and sons Felician and Fabian Juma for being my constant source of inspiration and having endured my role as a distant husband and father.
- The Juma family led by my dad; Mr. G.J Mukwano Snr. and my mum Beatrice Mukitang'a, my all-time cheerleaders even in my lowest moments.
- My late grandfather, Simon "Omwana" Wanyonyi Okhwa Marango for allowing me a second chance in my high school life by paying my school fees. Your death was kin to a burnt library.
- My high school Physics teacher Mr. John Nalianya to whom I credit my academic resilience and passion for physics. May all teachers be as motivating as you were 20 years ago.

Acknowledgment

Firstly, I would like to thank God for giving me the strength and good health to finish my PhD. He remains a faithful father.

Secondly, I wish to thank my supervisors Prof. Malik Maaza; the UNESCO/UNISA African Chair in Nanoscience and Nanotechnology, and Prof Simon Dhlamini Mokhotjwa whose constant guidance has helped me to reach this far. I am glad to have benefited from their remarkable insights and positive criticism that made me a better Ph.D. candidate. I also sincerely appreciate Dr. Zephania Birech of the Laser Physics and Spectroscopy research group at the Department of Physics - University of Nairobi for suggesting this interesting research topic and guiding me through the publications of this Ph.D. work. I would also be negligent not to appreciate Dr. Cecil Ouma Moro and Dr. Nangamso Nathaniel Nyangiwe who helped with density functional theory and introduced me to Materials Studio.

I appreciate the National Research Foundation (NRF) under the TWAS-NRF African Renaissance Program for funding this research. Similarly, I appreciate the following institutions/organizations for providing resources that were key in this research; iThemba LABS, the Department of Physics - University of Nairobi, and the Electron Microscope Unit; University of Cape Town. All the institutions provided resources and a conducive environment that helped me to achieve my research objectives.

I thank members of my research group; Dr. Hamza Mohammed (post Doc), Nancy Mwikali Mwenze (PhD candidate), Annah Ondieki Moraa (PhD candidate), and Caro Misoy (MSc. Student) both at the MRD in iThemba LABS and the Laser Physics and Spectroscopy Research group at the Department of Physics; University of Nairobi for creating a vibrant and supportive research environment.

I wholeheartedly appreciate my high school physics teacher Mr. John Nalianya, a man who turned an “E” student into an “A” student. I appreciate him for making me love physics at a time when I felt like giving up on life and academia twenty years ago. My high school teacher, spiritual teacher, and mentor taught me to love God, always believe in myself, and have a special love for physics. I forever remain indebted.

Abstract

Biomolecular sensing and interaction monitoring have formed the basis for label-free analytical methodologies. The methodology involves the immobilization of the molecular receptor or biomolecule binding on the substrate without interference from modified analytes. The advantages of label-free methods explain their usage in biomedical and analytical techniques. In this work, localized surface plasmon resonance (LSPR) and vibrational-based optical techniques; Raman, FTIR, and surface-enhanced Raman spectroscopy (SERS) have been demonstrated as feasible methods applied in the detection of trenbolone acetate, anabolic androgenic steroid prohibited by the World Anti-doping Agency (WADA) due to its potential to enhance muscle mass and positively alter an athlete's endurance ability, resulting in unfair competition. Laser ablation in Liquid (LAL) was employed to synthesize silver nanoparticles from pristine silver granules. The nanoparticles were then characterized using SEM-EDS, TEM, LIBS, XRD, and EDXRF. SEM and TEM showed that the average particle size was 22nm. The silver nanoparticles were then used as the surface on which trenbolone acetate was adsorbed, leveraging their large surface area relative to their volume, giving ample sites for the molecule to attach. After adsorption, the plasmon band of silver nanoparticles was monitored with the help of UV-VIS spectroscopy. The results showed that after binding with the molecule, an average wavelength redshift of + 18nm of the plasmon band was noted. The value of the shift in the localized surface plasmon band exponentially reduces at lower concentrations before increasing with the increase in the concentration of trenbolone acetate until a saturation point is reached. Besides the shift in the LSPR band position, the band-broadening behavior of the Tren/Ac complex was monitored, showing an inverse exponential relation with analyte concentration. The results demonstrated that mixing silver nanoparticles with trenbolone acetate changes the refractive index of the dielectric environment and the impact can be monitored using UV-VIS spectroscopy.

Raman, FTIR, and surface-enhanced Raman spectroscopy were also employed to characterize the molecule. The Raman and FTIR spectra were obtained experimentally and also simulated with the help of density functional theory (DFT) implemented in Gaussian 09W software package. The results showed that the simulated spectra had a 99% similarity with what was obtained experimentally. Vibrational Energy Distribution Analysis (VEDA) helped to properly assign the vibrational bands to their functional groups through potential energy distribution (PED). Proper assigning of the molecule marks the hallmark of understanding unique vibrational bands that act as a fingerprint for the molecule. Such knowledge is particularly key in the anti-doping campaign since it allows declassifying trenbolone acetate from other steroids that have similar structural traits. The spectral characterization of the molecule was followed by surface-enhanced Raman spectroscopic studies with silver nanoparticles being used as a substrate. The electromagnetic field potential of silver nanoparticles allowed signal amplification of the trenbolone signal by X11. The signal was even enhanced when SERS was coupled to dry coating deposition Raman. The SERS mixture was drop-casted on an Aluminium foil hydrophobic surface resulting in X60 signal enhancement. The SERS amplification was achieved due to the effective tunability of trenbolone Acetate on silver nanoparticles. The orientation of trenbolone Acetate on silver nanoparticles was monitored by observing shifts in active SERS bands and through HOMO-LUMO studies of the molecule. SERS showed that some bands such as 1618cm^{-1}, 1748cm$^{-1,}$ and 2058cm^{-1} reported an average of 8nm blue shift in the wavenumbers. This region is assigned to the C=O ketone group which is attached to the acetate part of the steroid. The frontier molecular orbital analysis showed that the energy gap of trenbolone acetate was 3.798eV while the chemical potential of the molecule was 2.094 eV. Consequently, trenbolone acetate can easily participate in a chemical reaction since its potential is lower than the energy gap. The HOMO-LUMO also showed that O^{2-} is the most electronegative and hence the most active adsorbing site in the molecule. The chemical reaction between Ag^{+} and O^{2-} created an Ag$_2$O complex that influences both the plasmon behavior and the enhancement tendency in SERS. Based on the results of the synthesis and characterization of the silver nanoparticles, their use in surface plasmon resonance and as substrates in SERS, and finally the adsorption studies of Tren Act/ AgNPs complex using DFT, it is possible to develop a cost-effective analytical technique for androgen anabolic steroids. The work suggests using the results as a framework for developing a biosensor prototype for on-site analytical detection of performance-enhancement drugs prohibited in sports competitions.

Declaration..i
Dedication..ii
Acknowledgements..iv
Abstract..v
List of tables…………………………………………………………………… …ix
List of figures………………………………………………………..… ……x
List of abbreviations…………………………………………………………… …. xi
Publications………………………………………………………………... …. xii

Table of Contents

1 Introduction 1
  1.1 Background 1
  1.2 Statement of the Problem 7
  1.3 Problem Justification.. 8
  1.4 Aim of the Study and Objectives 9
    1.4.1 Specific Objectives 9
  1.5 Thesis Layout 10
2 Literature Review 17
  2.1 The World Anti-doping Agency (WADA).. 17
  2.2 The Prohibited List.. 18
    2.2.1 Class S1: Anabolic Agents 19
    2.2.2 Trenbolone Acetate 20
    2.2.3 Long-term Effects of Trenbolone Acetate.. 21
    2.2.4 Conventional Techniques for Detecting Trenbolone Acetate 22
  2.3 Steroid Detection Analytical Techniques 23
  2.4 Surface Enhanced Raman as an Analytical Technique in Doping 25
    2.4.1 Surface Enhanced Resonance Raman Scattering.. 26
    2.4.2 Surface Enhanced Raman Scattering Substrates.. 27
  2.5 Drop Coating Deposition as a Complementary Technique to SERS 29
    2.5.1 Gold, silver, and copper as Colloidal Materials for SERS substrates.. 30

2.6 Fabrication of Silver Nanoparticles 33
  2.6.1 Physical Methods 33
  2.6.2 Chemical Methods 33
  2.6.3 Biological Method 34
2.7 Localized Surface Plasmon Resonance Spectroscopy 35
  2.7.1 Shifts in the LSPR Band 35
  2.7.2 Broadening of the LSPR Band 37
  2.7.3 Silver Nanoparticles as a Core Shell 38
2.8 DFT Aided Vibrational Spectroscopy 38
  2.8.1 Adsorption Studies of Analytes on Silver Nanoparticles 39
3 Theoretical Background and Characterization Techniques 52
3.1 Introduction 52
3.2 The Theory of Raman Spectroscopy 52
  3.2.1 Classical Theory and mathematic Explanation of Raman Spectroscopy 54
3.3 Theory of Surface-Enhanced Raman Spectroscopy 56
  3.3.1 Electromagnetic Enhancement Mechanism 57
  3.3.2 Chemical Enhancement Mechanism 58
3.4 Localized Surface Plasmon Resonance 59
3.5 Theory of Laser Ablation in Liquid Technique 61
3.6 Characterization Techniques 64
  3.6.1 Microscope-Based Characterization Technique 65
  3.6.2 Spectroscopy-based Characterization Techniques 70
  3.6.3 X-Ray Based Characterization Technique 74
3.7 Density Functional Theory 77
  3.7.1 The Basis Set Selection 78
  3.7.2 DFT in air and using a solvent 79
4 Materials and Methods 85
4.1 Materials 85
  4.1.1 Trenbolone Acetate 85
  4.1.2 Silver Nanoparticles 85
4.2 Instrumentation 86
  4.2.1 Raman Spectrometer 86

4.2.2 FTIR Spectroscopy 86
4.3 Computational Details 86
4.3.1 DFT Analysis of Trenbolone Acetate 87
4.3.2 Geometry Optimization 87
4.3.3 Dmol$_3$ in Materials Studio 88
5 Results and Discussion 91
5.1 Laser Ablation in Liquid and Characterization of Synthesized Silver Nanoparticles 91
5.1.1 Colloidal Silver Nanoparticles 92
5.1.2 Characterization of Silver Nanoparticles 93
5.1.3 Raman Spectroscopy 101
5.1.4 Fourier Transform Infrared Spectroscopy 105
5.1.5 Energy Dispersive X-Ray Spectroscopy 106
5.1.6 Energy Dispersive X-ray Fluorescence 108
5.1.7 Laser-Induced Breakdown Spectroscopy 109
5.1.8 Scanning Electron Microscopy (SEM) 111
5.1.9 Transmission Electron Microscopy (TEM) 113
5.1.10 Conclusion 115
5.2 Localized Surface Plasmon Resonance in Detecting Trenbolone Acetate 117
5.2.1 Investigating the Beer-Lambert Law 117
5.2.2 Detection Limit of Trenbolone Acetate Using Absorbance Measurements 120
5.2.3 Optimizing AgNPs: Trenbolone Acetate Ratio 121
5.2.4 Impact of Trenbolone Acetate on the LSPR Band 123
5.2.5 Change in the Intensity of the Plasmon Band 124
5.2.6 Red-shift in the LSPR Band 125
5.2.7 Effect of Trenbolone Acetate on FWHM Band Broadening Behavior 126
5.2.8 Core-Shell Structure of Silver Nanoparticles 128
5.2.9 Conclusion 130
5.3 Silver Nanoparticles as Substrates Used in Surface-Enhanced Raman Spectroscopy 132
5.3.1 Raman Spectra of Trenbolone Acetate and Tren Ac/AgNPs Complex 132
5.3.2 Surface Enhanced Raman Spectra of Trenbolone Acetate 135
5.3.3 Orientation of Tren Ac on Silver Nanoparticles using SERS 136
5.3.4 Theoretical Analysis of SERS using DFT 139

5.3.5 Conclusion 142
5.3.6 Drop-Coating Deposition Raman Spectroscopy 143
5.3.7 Principal Component Analysis to Confirm Signal Distribution 146
5.3.8 DCDR and SERS as Complementary Techniques 147
5.3.9 Conclusion 148
5.4 Density Functional Theory Study of Trenbolone Acetate 150
5.4.1 Simulated and Experimental FTIR Spectra of Trenbolone Acetate 150
5.4.2 Simulated and Experimental Raman Spectra of Trenbolone Acetate 151
5.4.3 Vibrational Assignment and PED using VEDA 4 Program 153
5.5 Adsorption of Trenbolone Acetate on Ag (1 1 1) Surface; A DFT Study 157
5.5.1 Introduction 157
5.5.2 Computational Details 158
5.5.3 The Unit Cell and Surface Construction 159
5.5.4 Adsorption Energy 161
5.5.5 Quantum Chemical Calculations 163
5.5.6 Density of States 167
5.5.7 Mulliken Charge Distribution and Bond Length 170
5.5.8 Conclusion 172
6 General Conclusions and Future Studies 183
6.1 General Conclusions 183
6.2 Future Studies 185

List of Tables

Table 2-1: Part of the List of Prohibited substances according to WADA. 18

Table 5-1: Miller indices from XRD Spectra. 94

Table 5-2: Band assignment for simulated Raman and FTIR spectra of trenbolone acetate...... 153

Table 5-3: Adsorption energies of the surface, adsorbate, and surface + Adsorbate................. 161

Table 5-4: Optimized structure of Trenbolone Acetate and the frontier molecular orbital density distributions.. 163

Table 5-5: HOMO and LUMO chemical parameters describing the interaction between Tren Ac and AgNPs. 165

List of Figures

Figure 1-1: Procedure followed when using conventional analytical techniques to test and detect doping 6

Figure 3-1:The diagrammatic representation of the energy transfer model showing Reyleigh, Stokes and Anti-stokes Raman scattering Thorsten et al., [3] 54

Figure 3-2:Schematic of the electromagnetic field enhancement used in SERS. 58

Figure 3-3: Schematic of the charge transfer for chemical enhancement 59

Figure 3-4: Diverse applications that can benefit from metallic nanoparticles synthesized using Laser ablation in the Liquid approach. The red dotted circle depicts the application in this thesis. Adopted from: National Library of Medicine 62

Figure 3-5: A simplified laser-liquid ablation set up. The laser source is focused on the metal target placed in water. 62

Figure 3-6: Mechanism of the formation of nanoparticles using laser ablation in liquid 64

Figure 3-7: Principle of the SEM system employed in characterizing prepared silver nanoparticles. 66

Figure 3-8: Schematic Diagram showing the working of Transmission Electron Microscopy.... 69

Figure 3-9: Schematic diagram which shows how a UV-VIS spectroscopy works. 71

Figure 3-10: FTIR Spectrometer system. 73

Figure 3-11: Diffracted X-Ray Beam after hitting the sample. 75

Figure 3-12: Schematic Diagram of an X-ray diffractometer. 76

Figure 4-1:Molecular model of Trenbolone acetate molecule with the atom numbering system as appears in VEDA 4 program. 88

Figure 5-1: Observed color change on the silver nanofluids prepared at different ablation times. 92

Figure 5-2: XRD Spectra of laser ablated silver nanoparticles. 94

Figure 5-3:Absorbance spectrum of silver colloids for different ablation times by the same energy (200mJ) and pulse repetition frequency (5Hz). 97

Figure 5-4:UV-Vis spectra of AgNPs at different ablation energies and 20-minute ablation time and 5Hz frequency. 98

Figure 5-5:UV-Vis spectra of AgNPs at different repetition rates with time maintained at 1 hour and energy at 200mJ. 100

Figure 5-6: Raman spectra of silver nanoparticles using 532nm and 785nm laser strengths. 102

Figure 5-7: Characteristic Raman spectra of silver nanoparticles on Aluminium foil, calcium fluoride glass, and microscope glass, using a 532nm laser, 10 seconds exposure time, and 5 accumulations. The spectra have not been background subtracted to show the similarity......... 104

Figure 5-8: FTIR Spectra of Silver Nanoparticles. 106

Figure 5-9:EDS spectra of silver NPs optimized at different ablation times. 107

Figure 5-10: EDXRF Spectra of synthesized silver nanoparticles indicating the peak position of silver. 108

Figure 5-11: LIBS spectra for silver nanoparticles showing Ag emission lines. 110

Figure 5-12: SEM image of synthesized Nanoparticles; 10a, at 2 hours laser ablation, 10b at 5 hours laser ablation and 10 c and 10 d are for 8 hours laser ablation; X200 and X100 magnification respectively. 112
Figure 5-13: Histograms showing particle sizes from TEM analysis (inset: TEM images) for silver nanoparticles ablated at 8 hours (left) and 4 hours (right) with particle sizes 11nm and 16nm respectively. 113
Figure 5-14: Histogram showing the size of silver nanoparticles ablated at 2 hours; average particle size is 21nm.......... 114
Figure 5-15: Impact of ablation time on particle size and the absorbance of the plasmon band of silver nanofluid. 115
Figure 5-16:UV-VIS spectra of Trenbolone showing the absorbance band at 349nm (A) and the effect of concentration to signal intensity (B; the inset shows the calibration for concentrations between 0.1ppm to 70ppm) depicting the limit of Lambert-Beer Law. 118
Figure 5-17:UV-VIS spectra of trenbolone for the biosensing region of interest (A) and on the calibration curve (B). 120
Figure 5-18:Ratio of Tren Ac to Silver nanoparticles (A) and the influence of AgNPs concentration on the Tren Ac band position (B). 122
Figure 5-19: 5-19A; Influence of Varying Tren Ac Concentrations on the LSPR Position of AgNPs (inset: absorbance band of AgNPs) and the 5-19B is the LSPR shift.......... 124
Figure 5-20: How LSPR bands contract with the increasing concentrations of the trenbolone acetate 127
Figure 5-21: The EDS Spectra of AgNPs with atomic weight percentage concentration of Atoms 128
Figure 5-22; The EDS Spectra of Tren Ac Adsorbed on AgNPs with the atomic weight percentage concentrations 129
Figure 5-23: Raman spectrum of trenbolone acetate. 133
Figure 5-24: Raman and surface-enhanced Raman spectra of trenbolone acetate and Tren Ac when mixed with silver nanoparticles 135
Figure 5-25: Comparison of SERS and Raman spectra of Trenbolone acetate at different concentrations 137
Figure 5-26: Structure of Ag-10 cluster optimized with BL3YP/LANL2DZ. 140
Figure 5-27 SERS simulated spectra for the Ag 10 Tren complex calculated at the B3LYP/LANL2DZ level. 140
Figure 5-28: Impact of aliquot volume on the size of the coffee ring on both a dried drop on Aluminium foil and glass slide (5-28a) and the impact on the spectral intensity for spectra taken on the edge of the ring after drying on Aluminium foil.......... 143
Figure 5-29:The optical image of a dried coffee ring of a probe mixed with silver nanoparticles.145
Figure 5-30:Principal component analysis and loadings plot for data acquired at the edge (red) and center (blue) of the coffee ring after the drying of trenbolone acetate and silver nanoparticle SERS mixture. 146
Figure 5-31:Comparing the signal intensity of 3ppm trenbolone acetate using 785nm conventional Raman, SERS in liquid, and SERS after drying a 2µl aliquot mixture of silver nanoparticles and probe on Al foil.......... 147

Figure 5-32: Experimental and Simulated Raman spectra of trenbolone Acetate. 152
Figure 5-33: Schematic representation of the optimized Bulk Silver unit cell. 159
Figure 5-34: Trenbolone acetate adsorbed on Ag (1 1 1) slab with the side and the top view. Color code; oxygen: red, grey: carbon, and white: hydrogen 160
Figure 5-35: The TDOS was calculated using DFT-D/GGA formalism for Ag (a), Trenbolone acetate (b), and Ag/Tren Ac complex (c). 168
Figure 5-36: Mulliken Charge distribution (A) and bond length (B) for Trenbolone acetate molecule. 171

List of Symbols & Abbreviations

AgNPs – Silver Nanoparticles

AAS – Androgen Anabolic Steroids

DFT – Density Functional Theory

DCDR – Drop Coating Deposition Raman

EDS – Energy dispersive X-ray spectroscopy

EDXRF – Energy dispersive X-ray fluorescence spectroscopy

FT-IR – Fourier transmission infrared spectroscopy

FWHM – Full width at Half Maximum

HOMO – Highest occupied molecular orbital

HPLC - High-performance liquid chromatography

LAL – Laser ablation in Liquid

LIBS – Laser-Induced Breakdown Spectroscopy

LSPR – Localized surface plasmon resonance

LUMO – Lowest unoccupied molecular orbital

PED – Potential Energy Distribution

SPR – Surface plasmon resonance

SEM – Scanning electron microscope

SERS - Surface-enhanced Raman spectroscopy

SEF – Signal Enhancement factor

TEM – Transmission electron microscope

UV/Vis/NIR – Ultraviolet-visible near-infrared spectroscopy

WADA – World Anti-Doping Agency

Tren Ac – Trenbolone Acetate

Tren Ac/ AgNPs – Trenbolone acetate/ silver nanoparticles complex.

VEDA – Vibrational Energy Distribution Analysis

List of Publications Included in this Thesis

1. **Juma, M.W.**, Birech, Z., Mwenze, N.M. *et al.* Localized surface plasmon resonance sensing of Trenbolone acetate dopant using silver nanoparticles. *Sci Rep* **14**, 5721 (2024). https://doi.org/10.1038/s41598-024-56456-w
2. **Juma, M. W**., Nancy, M. M., Birech, Z., Ondieki, A. M., Maaza, M., & Mokhoztwa, D. (2023). Using laser ablation in liquid (LASIS) method to synthesize silver nanoparticles for SERS applications. *Materials Today: Proceedings*. https://doi.org/10.1016/j.matpr.2023.07.372
3. **Juma, M. W (2024)**. Surface Enhanced Raman Spectroscopy (SERS) Coupled to Drop-Coating Deposition Raman (DCDR)As Applicable in Doping Detection: Case of Trenbolone Acetate – **under review in IOP Publishing**
4. **Juma, M.W,** Zephania Birech, Nancy Mwikali Mwenze, Annah Moraa Ondieki, Hamza Elsayed Ahmed Mohamed, Mokhotjwa Simon Dhlamini and Malik Maaza, (2024) – **under review in Results in Chemistry**.

List of Publications Not Included in the Thesis

5. Ondieki, A. M., Birech, Z., Kaduki, K. A., Mwangi, P. W., **Juma, M.**, & Chege, B. M. (2023). Label-free assaying of testosterone and growth hormones in blood using surface-enhanced Raman spectroscopy. *Vibrational Spectroscopy*, *129*, 103605.
6. Mwenze, N. M., **Juma**, M., Maaza, M., Birech, Z., & Dhlamini, M. S. (2023). Laser liquid ablation for silver nanoparticles synthesis and conjugation with hydroxychloroquine for COVID-19 treatment. *Materials Today: Proceedings*.

7. Mwenze, N. M., Birech, Z., **Juma**, M., Morad, R., Cloete, K. J., Ondieki, A., ... & Maaza, M. (2024). Electronic and vibrational spectroscopic study complemented with the computational evaluation of hydroxychloroquine mixed with silver nanoparticles. *Results in Chemistry*, *10*, 101711.
8. Ondieki, A. M., Birech, Z., Kaduki, K. A., Mwangi, P. W., Mwenze, N. M., **Juma**, M., ... & Maaza, M. (2023). Fabrication of surface-enhanced Raman spectroscopy substrates using silver nanoparticles produced by laser ablation in liquids. *Spectrochimica Acta Part A: Molecular and Biomolecular Spectroscopy*, *296*, 122694.

1 Introduction

1.1 Background

There is a growing tendency towards using portable diagnostic tools in routine point-of-care analytical frameworks. The growing desire for such analysis has led to the growth of label-free approaches that often allow the development of biosensors using minimal sample preparation approaches and by eliminating expensive reagents used as labels [1]. Konoplev *et al*., [2] argued that label-free detection has emerged as an alternative approach to traditional label-based analytical methods. Label-free analysis techniques are preferred since they eliminate the need for chemical labels like fluorescent dyes, radioisotopes, or epitope tags, which can alter the natural properties and activities of molecules under study [3]. Furthermore, label-free techniques measure inherent properties of molecules, such as mass and dielectric properties, without modifying them, allowing for more accurate and reliable analytical outcomes [4].

Label-free analytical methodologies depend on their molecular biophysical properties such as the refractive index of the surrounding environment like in the case of localized surface plasmon resonance/ surface plasmon resonance or molecular charge to monitor the presence and activities of a molecule. Amir *et al*., [5] explains that using label-free analysis in biosensing allows molecular interactions by monitoring mechanical, electrical, or optical signals without the use of label probes. The author notes that the approach is fast, non-destructive, and requires minimal samples to achieve the required routine analysis.

The localized surface plasmon resonance (LSPR) technique is an example of a label-free analysis that uses metal nanoparticles for the sensitive detection of biomaterials [6]. LSPR is a phenomenon often observed on nanoparticles of metals like gold and silver providing a sensitive detection approach. For instance, Choi *et al*., [6] explained that dopamine which is considered a neurotransmitter in some diseases can be detected using the LSPR approach. Traditionally, dopamine is hard to detect at low concentrations due to the sensitivity limitation of conventional sensing techniques. The LSPR worked by monitoring the intensity changes of the analyte concentration. Nguyen *et al*., [7] also demonstrated that LSPR allows for instantaneous evaluations of how molecules interact with better accuracy and sensitivity, making it a powerful tool for biosensing applications [8].

Besides localized surface plasmon resonance (LSPR) and surface plasmon resonance (SPR), another label-free approach is vibrational spectroscopy which can be extended to biosensing applications [9]. Vibrational spectroscopy which includes Raman and mid/near-infrared spectroscopy has found great utility in analytical applications thanks to their sensitivity and ability to provide vibrational information with minimal sample volumes [10]. The techniques are also known to be non-destructive and as such, help to maintain the sample integrity. Both infrared and Raman spectroscopy leverage their characteristic vibrations in understanding the molecular structure of the substance under study Bunaciu *et al*., [11], Netchacovitch *et al*., [12]. Vibrational spectroscopy can be used to study a wide variety of samples, providing both qualitative and quantitative analysis of the molecule under study. Unlike mass spectroscopic or chromatography-based spectroscopy techniques, vibrational spectroscopy can be used to identify the content of a molecule in situ and non-destructively without the need for sample pre-treatment [13]. Such benefits have increased the use of vibrational-based analytical techniques.

Raman spectroscopy is a vibrational-based approach that is widely used for qualitative and quantitative analysis in biomedical applications. A vibrational Raman spectrum has a highly resolved and unique vibrational signature of the scattering molecule [14]. Its application can be done in molecules of any kind or matrix, including solutions, biomolecules, and solids (crystals and also powders). Such benefits are even more realized with the hand-held and portable Raman spectrometers that can be applied in the natural environment like in the food industry [15]. Raman spectroscopy has also been combined with statistical analytical techniques like partial least square discriminant analysis (PLS-DA) to provide fingerprints for the detection and quantification of drug traces in latent fingermarks [16]. Amin *et al*., [16] noted that Raman is an effective tool that can be leveraged for discriminatory analysis when separating specific drug traces from a pool of suspected/concealed drugs. Besides Raman, FTIR is another vibrational technique that has been employed in the detection and identification of drugs such as hazardous narcotic drugs and other psychoactive substances. Williams *et al*., [17] explain that FTIR helps to identify the chemical fingerprint of samples through chemical bond vibrations. Consequently, the technique can be applied in identifying unknown samples. Previous studies have shown the ability of both Raman and FTIR to be used in profiling illicit drugs like cocaine [18].

However, despite having benefits like being rapid and non-destructive, vibrational approaches; especially Raman suffer from a low signal-to-noise ratio since it is a relatively weak scatterer [19]. The noise in the Raman spectral data often limits its application, especially in quantitative analysis. To solve such challenges, techniques like surface-enhanced Raman spectroscopy singly or in combination with Drop coating Deposition Raman spectroscopy are often used.

Surface-enhanced Raman spectroscopy (SERS) can leverage nanostructured materials to achieve better signal enhancement [20]. The technique aids in the structural fingerprinting of analytes at low concentrations with the help of nanoparticles that offer their plasmon-mediated amplification of electrical and chemical enhancement. SERS provides a ray of applications, thanks to being ultra-sensitive and with high selectivity. Using SERS allows the enhancement of the desired signal to a tune of 10^{15} magnitude amplification [21]. SERS spectroscopy has been used to analyze various biosamples which include identifying cancer markers Chen *et al.,* [22], drug detection and drug delivery Liu *et al*., [23], and other in-vivo measurements that offer a range of medical applications and point-of-care diagnostics [24]. SERS works by utilizing plasmonic nanostructures that can enhance the nonlinear response through the localization of the incident field into hot spots that achieve better light-matter interaction. Therefore, SERS not only provides information about the chemical composition of a material under investigation by exploring the existing bond types but rather also helps to lower the detection limit in single molecule detection [25], [26]. Plasmonic nanoparticles like gold and silver provide a localized electric field when placed close to or when adsorbed to the target analyte. Based on the highlighted benefits, vibrational-based techniques, including surface-enhanced Raman can be utilized in the detection of drugs abused by sportsmen. Teodor *et al*., [27], and Alvarez-Puebla *et al*., [28] have already demonstrated the use of SERS in the classification of highly related performance enhancers. The authors noted that using SERS improves the intensity of any signal, increasing the accuracy of the analyte detection. The novelty of SERS as a label-free approach is based on SERS-active substrates for direct molecule identification through spectral characterization [29].

Doping, which has been banned by the World anti-doping agency (WADA) is a process through which athletes improve their performance by consuming foreign substances that have performance-enhancement capabilities. Doping is part of cheating and fraud to competitors, the sport itself, and the general public [30]. The World Anti-Doping Agency (WADA) has the mandate of ensuring fairness in sports by fighting the illegal use of doping materials as defined by the World Anti-doping Code [31]. Sports performance is based on four major components; the skills that competitors possess, strength, endurance, and recovery. Every sport leverages a distinct combination of these elements [32]. Unfortunately, such performance characteristics also correspond to the most common and yet effective forms of doping. For instance, sports activities that require explosive power are often susceptible to the use of androgen dopants since such dopants can increase muscle mass and strength. On the other hand, sports activities that leverage endurance use dopants that are likely to improve oxygen capacity in the body tissues [33]. Androgen anabolic steroids are some of the most common drugs that are abused by sportsmen and they include; testosterone, nandrolone, stanozolol, and their derivative forms like trenbolone acetate [34]. The use of such drugs in sports or for recreational purposes can also result in serious adverse effects like cardiovascular disease, neuroendocrine disorders, and neuropsychiatric conditions that can lead to increased premature mortality rates [33].

Such forms of drug abuse are controlled by testing athletes using matrices such as urine or saliva sampled during contests. The collected samples are then analyzed to explore the identity and quantity of the banned substances in analytical laboratories that have been credited by the World Anti-doping Agency[35]. Such laboratories differ from other conventional laboratories due to the huge number of samples that are to be analyzed within notable complex matrices. Furthermore, the concentrations are also often very low, calling for very sensitive analytical techniques. The analytical techniques often aim to analyze the drug's contents within the biological matrix; serum, saliva, or plasma to give a more successful approach to their doping detection or therapeutic monitoring [36]. Conventional techniques like High-performance liquid chromatography (HPLC), Enzymatic assays like ELISA, and isotope Ratio Mass Spectrometry have all been shown to be unreliable due to the large sample volume required and the pre-concentration that threatens the sample integrity. The process often adopted in doping analysis by use of these techniques is shown in Figure 1-1.

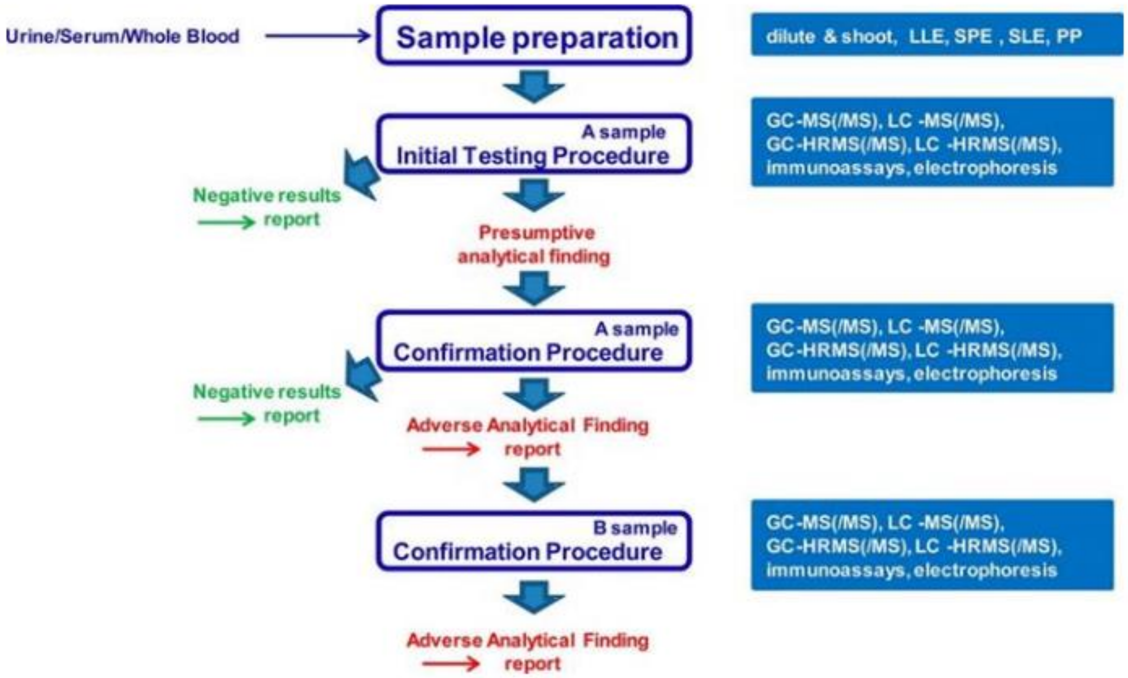

Figure 1-1: Procedure followed when using conventional analytical techniques to test and detect doping Athanasiadou et al., [37].

As indicated in step 1, the dilute and shoot stage requires among other steps, the pre-concentration of the sample. Such pre-concentration requires large sample volumes that may not be applicable in doping routine analysis. Spectroscopic-based techniques emerge as possible alternatives to these conventional analytical methods. FTIR combined with chemometric techniques has been shown to have great potential in doping analysis [38]. Amin *et al*., [16] recently showed the possibility of using Raman and surface-enhanced Raman spectroscopy in the detection and identification of drug traces in human urine. Despite these demonstrated capabilities, one of the challenges of vibrational-based spectroscopy especially Raman and SERS in bioanalytical detection is the lack of reference data that can be used to compare the vibrational modes of the target molecule [39].

Proper vibrational band assignment is regarded as a prerequisite for confident analysis in spectroscopy-based analytical methods [40]. For molecules whose spectroscopic data is not found in the literature, theoretical calculations are often required to ascertain the Raman and FTIR vibrational modes and to provide an in-depth assessment of the adsorption behavior of the nanoparticles with the target analyte when using nanoparticles as substrates for surface-enhanced Raman spectroscopy. Density Functional Theory (DFT) is one of the theoretical approaches that aid in interpreting the Raman, FTIR, and SERS spectra of the adsorbed molecules [41]. One of the key drivers of DFT is its reliance on molecular complexes of the ligands and how they get adsorbed on the metal surface. The adsorption behavior can be monitored with the help of DFT, giving an idea of changes in vibrational positions as depicted in frequency shifts of the Raman scatter bands [42]. Furthermore, with DFT, it is possible to identify molecular sites that have a significant contribution in interacting with the nanoparticles/metal surface. DFT is also important in providing information about low-frequency vibrations that may not be observed experimentally.

1.2 Statement of the Problem

The technology to detect performance-enhancement drugs and other illegal substances has improved significantly[43]. The number of athletes being caught in violation of sports regulations set up by the World Anti-doping Agency (WADA) continues to increase as a result of the development of new and more efficient analytical techniques and an increase in the number of accredited analytical laboratories. Most of the techniques look at not only the banned substances but also the metabolites that come up after the main compounds are broken down. The biological matrices that have been used to detect some of the drugs include urine, saliva, and blood.

Although many techniques have been used for analytical purposes, most suffer from the need to have big sample volumes besides being time-consuming and destroying the integrity of the sample. Consequently, there is a need to develop a sensitive and more rapid technique that leverages a small sample volume for the detection and quantification of drugs abused in sports as a key contribution to the analytical framework of the World Anti-doping Agency.

1.3 Problem Justification

Label-free analytical techniques such as localized surface plasmon resonance and vibrational spectroscopic techniques like Raman, FTIR, and SERS provide remarkable capability in the analytical detection of drugs abused in sports without the need for labels. LSPR has the advantage of being highly sensitive and allowing real-time monitoring with better specificity. LSPR allows the detection of biomolecular interactions without the need for chemical labels, enabling the detection of minute changes in the local refractive index near metallic nanostructures. On the other hand, the vibrational modes provided by the techniques are unique to the specific steroid molecules and as such, can act as a fingerprint for molecule identification. The identified bands also contribute to the spectral library used in characterizing a range of steroids that can be abused by athletes. To enhance the capability of these spectroscopy-based techniques, theoretical analysis using density functional theory is also suggested. Using DFT is based on the fact that the inadequacy of reference standards and spectral libraries makes it challenging to develop new spectroscopic-based analytical approaches that can be used by the World Antidoping Agency (WADA) in its anti-doping efforts. The challenge is even more compounded by the similar structural traits that many anabolic androgenic steroids (AAS) have, which provide their structural behavior comparable to their endogenous analogs. Therefore, complementing DFT with spectroscopic techniques provides potential for better characterization of the banned substances.

Biosensing of the target androgen anabolic steroid is also explored using localized surface plasmon resonance sensing (LSPR). By measuring the shifts in the band position of the localized surface plasmon resonance band, and changes in the band width and intensity of the plasmon band when an analyte is adsorbed on the nanoparticles, it is possible to detect concentration levels of an injected drug. Combining experimental and theoretical analysis and leveraging the localized surface plasmon resonance spectroscopy will be key in developing a rather rapid and label-free approach to detecting other dopants to fight unfairness in sports competition.

1.4 Aim of the Study and Objectives

This work aims to demonstrate the viability of spectroscopy-based techniques; Raman, FTIR, and SERS that leverage silver nanoparticle plasmonic and use LSPR in suggesting the development of a sensitive and label-free analytical technique for the detection of androgen anabolic steroids.

1.4.1 Specific Objectives

The specific objectives of the work are:

I. To synthesize silver nanoparticles from pristine silver granules using the laser ablation in Liquid (LAL) technique with water as the solvent.

II. To characterize the synthesized nanoparticles using techniques like UV-VIS, Raman spectroscopy, LIBS, SEM-EDS, and TEM.

III. To demonstrate the use of localized surface plasmon resonance spectroscopy (LSPR) of silver and silver Nanoparticles/Trenbolone acetate conjugate in the label-free detection of Trenbolone acetate.

IV. To use silver nanoparticles as substrates in surface-enhanced Raman spectroscopy (SERS) to develop a rapid and label-free approach in the detection of trenbolone acetate steroid.

V. To explore the adsorption behavior of trenbolone acetate on silver nanoparticle colloids using density functional theory (DFT) to give insights into molecular interactions towards LSPR and surface-enhanced Raman spectroscopic sensing.

1.5 Thesis Layout

Chapter 1: Provides an introduction and background to the thesis.

Chapter 2: Presents an in-depth Literature Review including the existing gap that the work seeks to address.

Chapter 3: Discusses a theoretical framework of laser ablation and characterization techniques.

Chapter 4: Theoretical and Experimental Procedures.

Chapter 5: Results and Discussion – divided into sub-sections as per the five objectives of the study.

Chapter 6: Summarizes the research Findings and Reveals Future work.

References

[1] Y. W. Kwon *et al.*, “Application of Proteomics in Cancer: Recent Trends and Approaches for Biomarkers Discovery,” *Front. Med.*, vol. 8, Sep. 2021, doi: 10.3389/fmed.2021.747333.

[2] G. Konoplev *et al.*, “Label-Free Physical Techniques and Methodologies for Proteins Detection in Microfluidic Biosensor Structures,” *Biomedicines*, vol. 10, no. 2, Art. no. 2, Feb. 2022, doi: 10.3390/biomedicines10020207.

[3] S. Ray, G. Mehta, and S. Srivastava, “Label-free detection techniques for protein microarrays: Prospects, merits and challenges,” *Proteomics*, vol. 10, no. 4, pp. 731–748, Feb. 2010, doi: 10.1002/pmic.200900458.

[4] N. Maccaferri *et al.*, “Ultrasensitive and label-free molecular-level detection enabled by light phase control in magnetoplasmonic nanoantennas,” *Nat. Commun.*, vol. 6, no. 1, p. 6150, Feb. 2015, doi: 10.1038/ncomms7150.

[5] A. Syahir, K. Usui, K. Tomizaki, K. Kajikawa, and H. Mihara, “Label and Label-Free Detection Techniques for Protein Microarrays,” *Microarrays*, vol. 4, no. 2, pp. 228–244, Apr. 2015, doi: 10.3390/microarrays4020228.

[6] J.-H. Choi, J.-H. Lee, B.-K. Oh, and J.-W. Choi, “Localized surface plasmon resonance-based label-free biosensor for highly sensitive detection of dopamine,” *J. Nanosci. Nanotechnol.*, vol. 14, no. 8, pp. 5658–5661, Aug. 2014, doi: 10.1166/jnn.2014.8830.

[7] H. H. Nguyen, J. Park, S. Kang, and M. Kim, “Surface Plasmon Resonance: A Versatile Technique for Biosensor Applications,” *Sensors*, vol. 15, no. 5, pp. 10481–10510, May 2015, doi: 10.3390/s150510481.

[8] K. V. Hackshaw, J. S. Miller, D. P. Aykas, and L. Rodriguez-Saona, “Vibrational Spectroscopy for Identification of Metabolites in Biologic Samples,” *Molecules*, vol. 25, no. 20, p. 4725, Oct. 2020, doi: 10.3390/molecules25204725.

[9] W. Querido, S. Kandel, and N. Pleshko, “Applications of Vibrational Spectroscopy for Analysis of Connective Tissues,” *Molecules*, vol. 26, no. 4, Art. no. 4, Jan. 2021, doi: 10.3390/molecules26040922.

[10] A. A. Makki *et al.*, “Qualitative and quantitative analysis of therapeutic solutions using Raman and infrared spectroscopy,” *Spectrochim. Acta. A. Mol. Biomol. Spectrosc.*, vol. 218, pp. 97–108, Jul. 2019, doi: 10.1016/j.saa.2019.03.056.

[11] A. A. Bunaciu, H. Y. Aboul-Enein, and Ş. Fleschin, “Vibrational Spectroscopy in Clinical Analysis,” *Appl. Spectrosc. Rev.*, vol. 50, no. 2, pp. 176–191, Feb. 2015, doi: 10.1080/05704928.2014.955582.

[12] L. Netchacovitch *et al.*, “Vibrational spectroscopy and microspectroscopy analyzing qualitatively and quantitatively pharmaceutical hot melt extrudates,” *J. Pharm. Biomed. Anal.*, vol. 113, pp. 21–33, Sep. 2015, doi: 10.1016/j.jpba.2015.01.051.

[13] R. Deidda *et al.*, “Vibrational spectroscopy in analysis of pharmaceuticals: Critical review of innovative portable and handheld NIR and Raman spectrophotometers,” *TrAC Trends Anal. Chem.*, vol. 114, pp. 251–259, May 2019, doi: 10.1016/j.trac.2019.02.035.

[14] R. S. Das and Y. K. Agrawal, “Raman spectroscopy: Recent advancements, techniques and applications,” *Vib. Spectrosc.*, vol. 57, no. 2, pp. 163–176, Nov. 2011, doi: 10.1016/j.vibspec.2011.08.003.

[15] W. White, “Identification of cave minerals by Raman spectroscopy: new technology for non-destructive analysis,” *Int. J. Speleol.*, vol. 35, no. 2, Jan. 2006, doi: http://dx.doi.org/10.5038/1827-806X.35.2.6.

[16] M. Amin, E. Al-Hetlani, and I. Lednev, “Detection and identification of drug traces in latent fingermarks using Raman spectroscopy,” *Sci. Rep.*, vol. 12, p. 3136, Feb. 2022, doi: 10.1038/s41598-022-07168-6.

[17] S. F. Williams, R. Stokes, P. Leung Tang, and A. M. Blanco-Rodriguez, “Detection & identification of hazardous narcotics and new psychoactive substances using Fourier transform infrared spectroscopy (FTIR),” *Anal. Methods*, vol. 15, no. 26, pp. 3225–3232, 2023, doi: 10.1039/D3AY00766A.

[18] N. V. S. Rodrigues, E. M. Cardoso, M. V. O. Andrade, C. L. Donnici, and M. M. Sena, “Analysis of seized cocaine samples by using chemometric methods and FTIR spectroscopy,” *J. Braz. Chem. Soc.*, vol. 24, pp. 507–517, Mar. 2013, doi: 10.5935/0103-5053.20130066.

[19] J. Jehlička, P. Vítek, H. G. M. Edwards, M. Heagraves, and T. Čapoun, “Application of portable Raman instruments for fast and non-destructive detection of minerals on outcrops,” *Spectrochim. Acta. A. Mol. Biomol. Spectrosc.*, vol. 73, no. 3, pp. 410–419, Aug. 2009, doi: 10.1016/j.saa.2008.09.004.

[20] X. X. Han, R. S. Rodriguez, C. L. Haynes, Y. Ozaki, and B. Zhao, “Surface-enhanced Raman spectroscopy,” *Nat. Rev. Methods Primer*, vol. 1, no. 1, Art. no. 1, Jan. 2022, doi: 10.1038/s43586-021-00083-6.

[21] J. Langer *et al.*, “Present and Future of Surface-Enhanced Raman Scattering,” *ACS Nano*, vol. 14, no. 1, pp. 28–117, Jan. 2020, doi: 10.1021/acsnano.9b04224.

[22] H. Chen *et al.*, “Recent advances in surface-enhanced Raman scattering-based microdevices for point-of-care diagnosis of viruses and bacteria,” *Nanoscale*, vol. 12, no. 42, pp. 21560–21570, Nov. 2020, doi: 10.1039/D0NR06340A.

[23] L. Liu, Y. Tang, S. Dai, F. Kleitz, and S. Zhang Qiao, “Smart surface-enhanced Raman scattering traceable drug delivery systems,” *Nanoscale*, vol. 8, no. 25, pp. 12803–12811, 2016, doi: 10.1039/C6NR03869G.

[24] B. Sharma, R. R. Frontiera, A.-I. Henry, E. Ringe, and R. P. Van Duyne, “SERS: Materials, applications, and the future,” *Mater. Today*, vol. 15, no. 1, pp. 16–25, Jan. 2012, doi: 10.1016/S1369-7021(12)70017-2.

[25] R. Zhang *et al.*, “Chemical mapping of a single molecule by plasmon-enhanced Raman scattering,” *Nature*, vol. 498, no. 7452, Art. no. 7452, Jun. 2013, doi: 10.1038/nature12151.

[26] L. Song *et al.*, “Amplifying the signal of localized surface plasmon resonance sensing for the sensitive detection of Escherichia coli O157:H7,” *Sci. Rep.*, vol. 7, no. 1, Art. no. 1, Jun. 2017, doi: 10.1038/s41598-017-03495-1.

[27] I. Izquierdo-Lorenzo, I. Alda, S. Sanchez-Cortes, and J. V. Garcia-Ramos, “Adsorption and Detection of Sport Doping Drugs on Metallic Plasmonic Nanoparticles of Different Morphology,” *Langmuir*, vol. 28, no. 24, pp. 8891–8901, Jun. 2012, doi: 10.1021/la300194v.

[28] R. Alvarez-Puebla, J. Vásquez, bo Cui, T. Veres, and H. Fenniri, “SERS Classification of Highly Related Performance Enhancers,” *ChemMedChem*, vol. 2, pp. 1165–1167, May 2007, doi: 10.1002/cmdc.200700085.

[29] X. X. Han, Y. Ozaki, and B. Zhao, “Label-free detection in biological applications of surface-enhanced Raman scattering,” *TrAC Trends Anal. Chem.*, vol. 38, pp. 67–78, Sep. 2012, doi: 10.1016/j.trac.2012.05.006.

[30] C. Blank, K. Weber, I. D. Boardley, T. Abel, W. Schobersberger, and L. B. Patterson, “Doping in Paralympic sport: perceptions, responsibility and anti-doping education experiences from the perspective of Paralympic athletes and parasport coaches,” *Front. Sports Act. Living*, vol. 5, p. 1166139, Jul. 2023, doi: 10.3389/fspor.2023.1166139.

[31] M. Al Ghobain, “The use of performance-enhancing substances (doping) by athletes in Saudi Arabia,” *J. Fam. Community Med.*, vol. 24, no. 3, pp. 151–155, 2017, doi: 10.4103/jfcm.JFCM_122_16.

[32] M. P. de Araujo, “Androgen Abuse among Recreational Athletes,” *RBGO Gynecol. Obstet.*, vol. 41, no. 12, pp. 679–681, Dec. 2019, doi: 10.1055/s-0039-3401007.

[33] T. Gagliano-Jucá and S. Basaria, “Abuse of anabolic steroids: A dangerous indulgence,” *Curr. Opin. Endocr. Metab. Res.*, vol. 9, pp. 96–101, Dec. 2019, doi: 10.1016/j.coemr.2019.10.002.

[34] Z. Wenbo and Z. Yan, “The Uses of Anabolic Androgenic Steroids Among Athletes; Its Positive and Negative Aspects- A Literature Review,” *J. Multidiscip. Healthc.*, vol. 16, pp. 4293–4305, Dec. 2023, doi: 10.2147/JMDH.S439384.

[35] “What We Do,” World Anti Doping Agency. Accessed: Feb. 23, 2024. [Online]. Available: https://www.wada-ama.org/en/what-we-do

[36] S. McLean, D. B. Desmond, and P. M. Salmon, “An analysis of the sports performance enhancing substances available on the darknet,” *Perform. Enhanc. Health*, vol. 11, no. 2, p. 100246, Jun. 2023, doi: 10.1016/j.peh.2023.100246.

[37] I. Athanasiadou, P. Kiousi, N. Kioukia-Fougia, E. Lyris, and Y. S. Angelis, “Current Status and Recent Advantages in Derivatization Procedures in Human Doping Control,” *Bioanalysis*, vol. 7, no. 19, pp. 2537–2556, Oct. 2015, doi: 10.4155/bio.15.172.

[38] F. K. Algethami, S. M. Eid, K. M. Kelani, M. R. Elghobashy, and M. K. Abd El-Rahman, “Chemical fingerprinting and quantitative monitoring of the doping drugs bambuterol and terbutaline in human urine samples using ATR-FTIR coupled with a PLSR chemometric tool,” *RSC Adv.*, vol. 10, no. 12, pp. 7146–7154, doi: 10.1039/c9ra10033d.

[39] A. H. Nguyen, E. A. Peters, and Z. D. Schultz, “Bioanalytical applications of surface-enhanced Raman spectroscopy: de novo molecular identification,” *Rev. Anal. Chem.*, vol. 36, no. 4, p. 20160037, Dec. 2017, doi: 10.1515/revac-2016-0037.

[40] N. Nenadis and M. Z. Tsimidou, “Perspective of vibrational spectroscopy analytical methods in on-field/official control of olives and virgin olive oil,” *Eur. J. Lipid Sci. Technol.*, vol. 119, no. 1, p. 1600148, 2017, doi: 10.1002/ejlt.201600148.

[41] M. Muniz-Miranda, F. Muniz-Miranda, M. C. Menziani, and A. Pedone, “Can DFT Calculations Provide Useful Information for SERS Applications?,” *Molecules*, vol. 28, no. 2, p. 573, Jan. 2023, doi: 10.3390/molecules28020573.

[42] A. A. El-Saady, N. Roushdy, A. A. M. Farag, M. M. El-Nahass, and D. M. Abdel Basset, “Exploring the molecular spectroscopic and electronic characterization of nanocrystalline Metal-free phthalocyanine: a DFT investigation,” *Opt. Quantum Electron.*, vol. 55, no. 7, p. 662, May 2023, doi: 10.1007/s11082-023-04877-8.

[43] Y. Lu, J. Yan, G. Ou, and L. Fu, “A Review of Recent Progress in Drug Doping and Gene Doping Control Analysis,” *Molecules*, vol. 28, no. 14, p. 5483, Jul. 2023, doi: 10.3390/molecules28145483.

2 Literature Review

This section provides an in-depth review of the literature on the topic and helps to unearth the existing gaps in the topic and how the recent research helps to fill this gap.

2.1 The World Anti-doping Agency (WADA)

The World Anti-doping Agency (WADA) was established in 1999 in the quest to promote fairness in competitive sports. The agency was set up to ensure athletes do not engage in doping, thereby guaranteeing fairness across diverse sporting events [1]. The motivation for the agency's establishment was the 1998 Tour de France event where a cyclist; Willy Voet was arrested for transporting performance-enhancement drugs during the event [2]. After his arrest, an inquest was established with the history of doping being unearthed. The event led to the hosting of the World Conference on Doping by the International Olympic Committee. In 1999, there was a conference where participants called on the formation of a board that could help to promote fairness in sports by fighting doping [3]. Consequently, the World Anti-Doping Agency was set up with the first mandate being to ensure anti-doping efforts were enforced in the Sydney Olympiad in 2000. WADA was established with the support of governments, inter-governmental agencies, and private organizations that envisioned a doping-free sport internationally [4]. Some of the key aspects that define WADA's mandate are to carry out scientific research, evaluate the capacity of laboratories to carry out anti-doping campaigns, and generally, promote anti-doping strategies [5].

The World Athletic Guide gives athletes and coaches what is expected of them and ensures they are accountable for their actions. One of the items in the guide is the prohibited list which itemizes the drugs that are classified as performance enhancers and as such, prohibited by WADA. WADA also uses its powers to protect athletes' rights to participate in sports activities that are free of any doping, promoting health and leading to fairness and equality in competition worldwide. The World Anti-Doping Code also develops programs used in the detection and deterrence of doping activities.

2.2 The Prohibited List

The World Anti-doping Agency keeps an updated list of substances classified as dopants and which have been banned in sporting competitions. The list itemizes substances that have been banned in and out of competition, including banned substances for specific sporting activities. All signatories of the WADA Code must ensure adherence to the list by setting out key prevention measures to reduce doping. The prohibited list is created and then confirmed by a group of experts who include the Health, Medical, and Research Committee as well as WADA's Executive Committee [6]. A summary of some of the prohibited substances according to WADA and the different classes to which they belong is provided in Table 2-1.

Table 2-1: Part of the List of Prohibited substances according to WADA.

Class	**Substance category**	**Example**	**When banned**
S0	Substances classified as non-approved	BPC-157, 2,4-Dinitrophenol (DNP) and Troponin Activators	All times
S1	Anabolic substances	Androgen anabolic steroids like testosterone, Danazol, Stanozolol, and Trenbolone. Other anabolic agents like Clenbuterol	All times
S2	Peptide hormones, growth factors, related substances,	Erythropoietin, peptide hormones, and their releasing factors	All times
S3	Beta-2 agonists	Inhaled salbutamol	All times

S4	Hormone and metabolic modulators	Anastrozole and Toremifene	All times
S5	Diuretics and masking agents	Acetazolamide and Vaptans	All times

Other drugs that have been prohibited fall under class M1 which is composed of drugs that manipulate blood and blood components, M2 for chemical and physical manipulation, S6 which are stimulants and banned during competition and S7 and S8 which are narcotics and cannabinoids respectively also banned in-competition [6]. A detailed analysis of class S1 which is the class of interest for this research is discussed in the next section.

2.2.1 Class S1: Anabolic Agents

Anabolic agents form class S1 of the substances in the banned list according to WADA and comprise substances banned both within and out of competition. The drugs include androgens like testosterone and methenolone that are endogenously produced or their derivatives that are synthetically manufactured. Anabolic steroids are a type of anabolic agent that are synthetic versions of the male hormone testosterone. The two form a vast majority of the drugs that are used in sports to enhance performance.

Anabolic-androgen steroids have attracted attention as doping substances due to their ability to reduce protein breakdown and increase protein synthesis and have androgenic effects like increasing muscle mass by activating the androgen receptor [7]. The use of androgen anabolic steroids is popular and Joseph and Kristina [8] assert that at least 1-3% of U.S. inhabitants use such steroids with more estimates being reported for younger users. Some of the reasons for the widespread use of steroids include their ability to improve athletic capability, enhance personal appearance, and masculinity, and give confidence among peers. The widespread usage of such drugs is often against the known side effects including affecting all the body organs and hampering their functions. Anabolic androgenic steroids (AAS) are known to have long-term toxicity that involves the cardiovascular and reproductive system and as such, the continued use of AAS is regarded as a published health issue. One of the commonly abused androgen anabolic steroids is Trenbolone acetate.

2.2.2 Trenbolone Acetate

Trenbolone is a performance-enhancement drug that belongs to the class of synthetic anabolic androgenic steroids (AAS) due to its anabolic properties like increasing muscle size and muscle strength [9]. The World Antidoping Agency categorizes Trenbolone as an anabolic androgenic steroid under S1 1 in its list of prohibited drugs.

Laura *et al*., [10] stated that trenbolone acetate is the commonly investigated androgenic hormone due to its application in veterinary medicine where it is used to increase animal muscle mass. The hormone is administered as an injection into the muscles and is used for its strong anabolic and androgenic effects and is also a prodrug of trenbolone [11]. The drug has also been extensively used to fatten cattle and as such, their metabolites can easily be traced in dairy products. Durhan *et al*., [11] noted that unlike other forms of trenbolone such as trenbolone enanthate, trenbolone acetate doesn’t convert to estrogenic metabolite hence leading to a lack of estrogenic side effects.

Besides being a dopant abused in sports, trenbolone is used for veterinarian purposes and has been abused in breeding cattle. The androgen anabolic steroid (AAS) medication which is commonly used for muscle enhancement among bodybuilders has also found its way as a dopant abused in sports. In countries such as South Africa, the drug can be obtained easily over the shop counter, especially for bodybuilders.

2.2.3 Long-term Effects of Trenbolone Acetate

Trenbolone is an approved veterinary scheduled drug that is illicitly used by humans. The drug is also referred to as Finajet and is among the commonly encountered drugs in the illicit market [9]. Trenbolone acetate has been used in the form of Finaplix H pellets by bodybuilders who call it Fina [12]. Their ability to increase muscle mass has increased their illicit use. Other drugs that are commonly abused include boldenone, nandrolone, testosterone, and stanozolol. Using these drugs has been associated with physical side effects that include high blood pressure due to elevated cholesterol levels, severe acne, increased risks of premature balding, low sexual function as well as testicular atrophy [13]. Among males, administering androgenic steroids also increases the risks of abnormal breasts in males. Females are also likely to develop male traits including a deeper voice, fewer menstrual cycles, and smaller breasts [14]. Therefore, besides resulting in unfair competition in sports, trenbolone acetate, and other androgenic anabolic steroids result in notable negative side effects which calls for the development of more reliable and sensitive detection techniques.

A case in point depicting the negative side effects of trenbolone acetate is that of a young man who had a myocardial infarction. The 23-year-old athlete presented to the emergency care setting with pain radiating from the left arm accompanied by severe nausea. Some of the vital signs the patient manifested include high blood pressure, faster heart rate which was 105 per minute, and high respiratory rate. A physical exam also showed that the patient had sweated and his lungs were clear on auscultation. The conclusion drawn from the examination was that the patient had overused trenbolone acetate which had impaired his breathing. The case in point demonstrates the negative side effects of using trenbolone acetate, including the risks of cardiovascular disease [14]. The mortality rate is also noted to be high among abusers of androgen-anabolic steroids [15]. Consequently, better analytical techniques for detecting androgen anabolic steroids are necessary due to the increasing prevalence of their use, especially among recreational gym-goers and athletes. Despite the rise in usage, the detection and subsequent quantification of anabolic-androgenic steroids remains a challenge highlighting the need for the scientific community to develop more rapid and reliable analytical methodologies [16].

2.2.4 Conventional Techniques for Detecting Trenbolone Acetate

LC-MS-based techniques are often employed to analyze trenbolone and its subsequent metabolites. Thevis *et al*., [17] demonstrated that tren Arc and its metabolites can be detected in the range of 1 – 10ng/ml in urine while Tudela *et al*., [18] also detected trenbolone metabolites in less than 10ng/ml in the same matrix. The metabolite identification based on hydrogen isotope ratio mass spectrometry was also developed and successfully used by Thevis *et al*., [17].

The detection of trenbolone acetate dopant in the traditional drug testing approaches is complex as approaches that use gas chromatography/ mass spectrometry (GC/MS) are said to be complicated due to the unspecified derivation products as well as artifacts [19]. Putz *et al*., [19] note that current GC/MS procedures used for analytic steroids and other metabolites, especially in human urine have not managed to detect trenbolone and its metabolites as a result of the problems with derivatization. Furthermore, there is a lack of enough literature that explains the biotransformation of trenbolone acetate in humans [20]. Methods like liquid chromatography and mass spectrometry have relatively high limits of detection which are way above the threshold set by the world anti-doping agency. According to WADA, the lowest allowable detection range for performance-enhancement steroids and other drugs needs to be between 1 to 10ng/ml [17]. Therefore, techniques that can detect the dopants to this level are always desired. The lowest limit of detection is in this case defined as the lowest measurable/detectable amount based on reasonable statistical levels and a signal-to-noise ratio that is equal to or more than 3 [21].

The number of studies on how to detect trenbolone by spectroscopic techniques is quite limited. However, vibrational studies of trenbolone have already been done with the Raman frequencies assigned between 1550cm^{-1} and 1600cm^{-1}. Furthermore, although the vibrational spectroscopic studies of synthetic anabolic steroids have been presented, there is currently no research that has reported on trenbolone despite the dopant being commonly abused by sports athletes.

2.3 Steroid Detection Analytical Techniques

There has been a significant improvement in the technology used to detect performance enhancement [22]. The number of athletes being caught in drug enhancement continues to increase as new analytical methods remain to be developed [23]. The improvement in technology is reflected in the ability to detect not only the banned substances but also their metabolites. The samples that have been used to detect these drugs include urine, saliva, and blood. The analytical technique to be used depends on the biological sample [24].

Gas Chromatography and Gas Chromatography-Mass Spectrometry were the first analytical techniques employed in the 1970s for qualitative and quantitative analysis of banned substances [25]. By the 1988 Olympic Games, GCMS could be used to detect narcotics, stimulants, and beta blockers [26]. The analytical technique is still usable in identifying steroids and other volatile drugs owing to the lipophilic and nonpolar nature of the steroid hormones. The main undoing of Gas Chromatography includes the time-consuming derivatization of nonvolatile molecules and the lengthy times, as well as the limitation on the sample type and size as large and polar molecules, may not be possible to analyze [27].

The second technique is Liquid Chromatography-Mass Spectrometry (LC-MS) which allows the detection of previously untraceable drugs [28]. However, the challenge with this technique remains being expensive, its insensitive, and subsequent inability to detect low concentrations besides bulky sample sizes [29]. The method also needs preconcentration and purification treatments as a result of the low analyte concentrations and the complexity of the mixtures [29]. Mass spectroscopy has revolutionized the detection of various compounds/substances used as dopants in sports. However, the challenge that exists is the inability to identify new designer androgens since their chemical signature is largely unknown [30]. Another method is the use of RNA testing which are new tests that have been developed by both the University of Brighton and Duke University that leverage the use of RNA testing in predicting patterns in the aging of blood. The alternative method has also been proven to be effective in detecting levels of performance-enhancement drugs [24].

The use of Biomarker tests emerges as new assays and analytical methodologies in the detection and quantification of steroids and hormones in samples [31]. Biomarkers are described as measurable markers through which diseases can be detected. Some of the commonly employed biomarker tests for drug abuse are the use of doping-specific hormones as well as erythropoietin abnormalities [32]. Despite the notable strides made in the detection of dopants in different samples, protein analytes especially peptide hormones remain a challenge for the anti-doping agency [33]. Rapid analytical techniques are desired especially in dealing with the high number of doping control samples as well as the short response time in sports events.

2.4 Surface Enhanced Raman as an Analytical Technique in Doping

Vibrational spectroscopy has found great utility in biomedical applications, including disease diagnostics and point-of-care analysis. With SERS, the target analyte is adsorbed on metallic nanostructures like gold (Au) and silver (Ag) that help to enhance the Raman signal, allowing the ultra-sensitive detection of performance-enhancement substances. Feng *et al*., [34] combined liquid phase extraction and surface-enhanced Raman spectroscopy to address the doping detection challenges often associated with traditional doping detection approaches. Feng *et al* noted that SERS is a powerful approach that can be used to assess saliva content in a routine analysis. With SERS, the target analytes get adsorbed on the metallic nanostructures like gold or silver hence enhancing the Raman signal. Furthermore, Feng *et al*., [34] successfully detected clenbuterol, methadone, oxycodone, and chlordiazepoxide in human saliva and urine with the limit of detection ranging from 10-50ng/mL. Liquid phase extraction was first used to isolate the target compound before SERS was used achieving a rapid and accurate detection of the four doping substances. The research demonstrated the potential that SERS has for on-site rapid detection of drugs abused in sports.

The use of SERS for the analytical detection of doping drugs at trace levels can be implemented with the final goal being to develop an analytical method for drug detection using SERS [35]. The method being used for the analytical detection of dopants using SERS has already been demonstrated by Wang *et al*., [36]. In making SERS, Au, and Ag are often used as surface enhancers due to their stronger SERS efficiency. SERS can be used for tests that need both univocal identification and higher sensitivity for the target substances.

Adsorption and detection of sport doping drugs have been demonstrated using different nanoparticles. Izquierdo *et al*., [36] confirmed the effective use of the adsorption and detection of probenecid (PB) which is a drug used as a masking agent in sports doping using vibrational spectroscopy. The modeled FTIR and Raman spectra were first assigned using density functional theory calculations before a detection protocol was developed based on SERS. The study noted that it is possible to use SERS to detect PB at concentrations as low as 1.2mg/ml. Izquierdo *et al*., [36] also explored the adsorption of clenbuterol, salbutamol, and terbutaline on metal surfaces by using the surface-enhanced Raman scattering technique. Characterization of the drugs had already been done using vibrational Raman spectroscopy with the support of density functional theory calculations. Consequently, SERS was employed to enhance the signals and improve the detection limit of the target dopants. Therefore, while SERS can be effective in detecting and quantifying the concentrations of the target analyte, it can be more effective when coupled with other techniques like density functional theory calculations that explore the vibrational frequencies. In practice, the use of SERS means the adsorption of the analyte/molecule on the metallic surface.

2.4.1 Surface Enhanced Resonance Raman Scattering

Surface Enhanced Resonance Raman Scattering (SERRS) is a powerful approach used in doping analysis, particularly in the field of anti-doping and forensic analysis. This technique leverages the enhanced Raman scattering effect to detect and analyze substances like anabolic-androgenic steroids (AAS) in biological samples. The use of SERRS in doping analysis offers a sensitive and specific method that can be integrated into routine anti-doping procedures, enhancing the detection capabilities for prohibited substances.

2.4.2 Surface Enhanced Raman Scattering Substrates

The invention of SERS has seen different substrates being used to enhance the target Raman signals. Some of the substrates used to achieve Raman signal enhancement include roughened electrodes, colloids, and thin films.

2.4.2.1 Electrodes

Electrodes were extensively used as SERS substrates since it was easy to control their surface potential. However, for optimal SERS efficiency, proper treatment of the electrodes is necessary. Electrochemical electrodes are metal surfaces that allow for spectroscopic study of electrochemically active molecules. For instance, Fleischmann *et al.*, [37] and his group at the University of Southampton carried out a Raman spectroscopic study and expected a high signal intensity by adsorbing molecules on roughened metal electrodes. Using the technique, Fleischmann *et al.*, [37] reported a high-quality Raman spectrum of pyridine which was electrochemically roughened on a silver electrode. The authors noted that the electrochemical roughening of the metal surface resulted in an increase in the surface area of the electrode allowing single-molecule detection. In many cases, electrodes are made using polycrystalline silver wires, providing hot spots that help to achieve higher signal enhancement. The surface is then mechanically polished, then chemical etching procedure is carried out on the metal electrode. The type of electrolyte used on the metal surface provides the electrical potential and dictates the amount of charge passed during oxidation. It is that charge that determines the level of SERS enhancement.

2.4.2.2 Metal Films

The other kind of substrate that can be used to achieve SERS enhancement is metal films. Some of the common metal sheets that provide the thin film surface for signal amplification include silver, gold, and copper [38].

2.4.2.3 Colloids

Colloidal nanoparticle suspensions are some of the widely used classes of substrates used in surface-enhanced Raman spectroscopy. One of the advantages of colloidal nanoparticles is the fact that they provide notable hot spots with a wider detection volume as compared to metal sheets. Despite such benefits, the aggregation behavior of the nanoparticles with the target analyte is complex and dictates the SERS signal intensity. Ryan *et al.*, [39] emphasizes the need to understand the factors that govern the behavior of the colloidal nanoparticles for an effective formation and for controlling the aggregation of nanoparticles. The colloidal nanoparticles in aqueous solution are often combined with the analyte of interest. Solutions of metallic colloids which are often made of silver or gold form the simplest and yet effective way of forming a SERS substrate. Since colloids are easy to produce in the laboratory, they form the easiest and most effective SERS substrate. Single-molecule SERS detection was initially made from metallic colloids in water. Besides the ease of formation, metallic colloids are also preferred as SERS substrates since they can easily be manipulated for analytical purposes.

The colloidal systems are made of particles whose diameters range from 1 to 100nm. The nanoparticles are often negatively charged due to the adsorbed anions [40]. The nanoparticles tend to have a high surface area to volume ratio, which enhances the interaction between the analyte molecules and the metal surface, leading to a stronger Raman signal [41]. Similarly, the colloidal nanoparticles exhibit strong plasmonic properties, which can be tuned by controlling the size, shape, and composition of the nanoparticles. Metallic nanoparticles can be easily synthesized and functionalized with various chemical groups, allowing for the creation of highly reproducible and uniform substrates [42]. The other benefit of metallic nanoparticles is the ability to directly estimate the extinction spectrum. However, colloidal nanoparticles have the disadvantage of instability due to their aggregation and the settling out of the solution when mixed with an adsorbate. The other disadvantage is the inability to control the surface potential that depends on the solution potential.

The colloidal nanoparticle substrates and analyte interaction form the basis for signal enhancement. Molecules that have functional groups like -SH, $-NH_2$, $-NH_4^+$, -COO-, -CN, and the carbonyl groups have been shown to strongly bind to metallic nanoparticles [43]. Such strong binding results in a strong signal-to-noise ratio, a critical measure in surface-enhanced Raman spectroscopy. Since some molecules loosely attach to the substrate, understanding the binding behavior is key in explaining the SERS mechanism.

2.5 Drop Coating Deposition as a Complementary Technique to SERS

Drop-coating deposition Raman spectroscopy (DCDRS) has previously been used singly or in combination with surface-enhanced Raman spectroscopy for analytical purposes. DCDRS is based on the measurement of a sample that has been pre-concentrated by being dried on a hydrophobic surface. The advantage of DCDRS is that it requires small sample volumes to achieve higher sensitivity as compared to what conventional Raman can give. Eva *et al.*, [44] noted that with DCDRS, it is possible to detect Raman signals from weak Raman scatters or materials at very low concentrations. Resonance Raman spectroscopy and surface-enhanced Raman were defined as undesirable techniques by Zhang *et al*., [45] owing to their problems with spectral alteration, high background, and strong fluorescence signal as well as the possibility of photochemical damage. DCDR has been demonstrated to be effective in understanding the composition of biological molecules like amino acids, proteins, and peptides. Analysis of molecular mixtures and complex solutions have also been demonstrated with the help of drop-coating deposition, Raman. Since DCDR allows the detection of molecules in complex mixtures, the method can be extended to routine doping analysis where the chemical and structural properties of a target drug are key. While investigating food and organic contamination, Kuizovara *et al*., [46] noted that contaminants such as melamine and thiram fungicides could be detected using drop-coating deposition Raman spectroscopy and not classical Raman under the same experimental conditions. Drop coating deposition Raman was found to be effective in achieving a better detection limit for these contaminants in their complex matrices. The authors concluded that the sensitivity of DCDR is comparable to or even better than that of surface-enhanced Raman spectroscopy. Kuisova *et al*.,[44] further noted that DCDRS can be combined with SERS to provide a complementary approach that achieves an even higher signal intensity for sub-ppb concentrations being detected in a mixture of other molecules.

2.5.1 Gold, silver, and copper as Colloidal Materials for SERS substrates

As mentioned in the previous sections, gold, silver, and copper are some of the most common metals often used in SERS, albeit with different enhancement capabilities. Gold and copper can be used for radiations within the near-infrared region while silver is applicable for excitations ranging from the visible to near-infrared [47]. When compared to copper and gold, silver has a higher plasmon quality and experiences better chemical stability.

Gold nanoparticles were used as potential substrates in detecting rhodamine 6G (R6G) as a probe molecule. Narode *et al*., [48] noted that the design and optimization of efficient substrates is challenging. Gold nanoparticles have been used for their distinct chemical and physical attributes that allow them to be used as chemical and biological sensors. The nanoparticles can be synthesized straightforwardly and their stability is easier to achieve. Gold nanoparticles also provide a high surface-to-volume ratio with excellent biocompatibility using appropriate ligands. Similarly, their properties can be easily tuned based on their size, shape, and the surrounding environment allowing a detectable resonance signal [49]. Saha *et al*., [49] further explained that once proper optimization is made, the surface plasmon resonance shifts that are attributed to localized surface plasmon hot spots between the nanoparticles and the SERS signal are used to explore the biosensing ability of gold nanoparticles.

Despite its use, gold may not be preferred in routine doping analysis due to toxicity concerns. Alkilany and Murphy [50] have shown that gold nanoparticles less than 2 nm in diameter can trigger cellular damage, necrosis, mitochondrial damage, and oxidative stress in cell lines. The underlying interactions of gold nanoparticles with physiological fluids are a major undoing for the nanoparticles when applicable in routine doping analysis. The low water solubility property of gold nanoparticles was particularly a main undoing for its use in biosensing applications. Similarly, gold is expensive making it challenging to be used as a target material for laser ablation in a liquid approach.

Copper nanoparticles also possess a localized surface plasmon resonance effect. However, the localized surface plasmon resonance applications based on copper nanoparticles are limited since copper is prone to oxidation. Similarly, the absorption of copper (I) oxide and copper (II) oxide, the interband transition of electrons from 3d to 4s overlap, and the LSPR of CuNPs, all make the LSPR of CuNPs difficult to identify [51]. Although inexpensive, copper nanoparticles are generally perceived to possess weak and broad LSPR characteristics, making it challenging to achieve strong and narrow resonance lines typically desired for effective biosensing applications [52]. Such disadvantages make copper nanoparticles undesirable substrates for biosensing applications.

Silver nanoparticles emerge as the most commonly used substrates in localized surface plasmon resonance spectroscopy. Among the precious metals, silver is preferred since it has the longest electronic lifetime. Electronic lifetime in this case defines the time that silver can maintain its electronic properties without degrading. In the context of localized surface plasmon resonance (LSPR), achieving a long electronic lifetime is crucial for enhancing the sensitivity and stability of plasmonic applications [53]. The ability of silver nanoparticles to sustain their electronic characteristics over an extended period is advantageous for various applications, including biosensing and imaging. In plasmon sensing, silver nanoparticles are also preferred due to their high sensitivity to refractive index changes, which is crucial for detecting minute variations in the surrounding environment [54]. This sensitivity enhances the accuracy and precision of LSPR-based biosensing applications. The other benefit of silver nanoparticles is their plasmonic interaction with light resulting in greater field enhancements and tunable resonances in the visible-to-near-infrared regions. This strong interaction enhances the sensitivity and effectiveness of LSPR sensors based on silver nanoparticles [55]. Silver nanoparticles are also preferred in localized surface plasmon resonance sensing since it has the largest negative real dielectric constant compared to other plasmonic materials and most sensitive to changes in the local refractive index [56].

2.6 Fabrication of Silver Nanoparticles

A variety of fabrication techniques have been reported for the synthesis of different nanoparticles, including silver nanoparticles. The methods include physical, biological, and chemical synthesis approaches.

2.6.1 Physical Methods

Physical methods are fabrication methods that provide nanoparticles from large-sized materials/ bulk materials without atomic control. Physical methods have the advantage of producing particles with uniform size distribution and the absence of solvent contamination. Some of the physical methods used to synthesize nanoparticles include evaporation-condensation, sedimentation process, ball milling, and laser ablation method [57]. Among the physical methods, laser ablation is preferred due to the absence of chemical reagents in the solution, allowing the production of pure and uncontaminated nanoparticles. Laser ablation also provides high production rates and produces particles with a specific size and shape by tuning ablation parameters. Although one of the challenges of laser ablation is the aggregation/agglomeration behavior of nanoparticles, the approach is often used since it achieves nanoparticles with the desired physical attributes. Similarly, like other green synthesis methods, laser ablation is environmentally friendly.

2.6.2 Chemical Methods

Chemical approaches for synthesizing nanoparticles are those that involve chemicals in the production of nanoparticles. Unlike physical synthesis methods, chemical methods provide a better yield of the nanoparticles. The most common chemical method is one involving chemical reduction. For silver nanoparticles, chemical methods may involve adding precursors that help to stabilize and regulate the growth of nanoparticles [58, p. 7]. The method often influences the intrinsic properties of the synthesized nanoparticles. Some of the commonly used precursors for making silver nanoparticles are citrates and acetates of silver. Stabilizing agents are often used to ensure the nanoparticles are stable as they are suspended in solution and to reduce the risks of sedimentation and agglomeration. Since most of the precursors used in chemical method synthesis are toxic, the method is less preferred in making nanoparticles whose purity is important. Their toxic by-products are also a threat to the environment.

2.6.3 Biological Method

The biological method is a fast-growing method for synthesizing nanoparticles by leveraging plants, fungi, and bacteria. Bacterial methods can reduce metal ions released into the environment. Green synthesis involves using biological sources like plants, bacteria, yeasts, molds, and microalgae to synthesize nanoparticles. Plants, in particular, have shown great potential for nanoparticle biosynthesis due to their speed and stability compared to microorganisms [59]. On the other hand, plant extracts can be used as reducing agents to synthesize nanoparticles like silver, gold, platinum, and titanium. This method is cost-effective, environmentally friendly, and safe for humans. Biological methods are economical, energy-saving, and produce low-cost products that are safe for human health and the environment. They also allow for large-scale synthesis of nanoparticles. However, despite the many advantages that come with using green synthesis methods, the need for strong reducing agents, the need for identification and isolation of strong bioactive molecules makes the method undesirable for synthesizing nanoparticles [60].

2.7 Localized Surface Plasmon Resonance Spectroscopy

LSPR can be defined as an optical approach that is generated once the light gets trapped inside the conductive nanoparticles which are generally smaller than the light wavelength. The interaction is often a result of the interaction between incident light and electrons that resonate in the conduction band. LSPR is a powerful approach for chemical and biological sensing and is also used in electromagnetic field enhancement that achieves surface-enhanced Raman scattering and other surface-enhanced spectroscopic techniques [61].

LSPR is an important candidate for developing plasmonic biosensors that have good sensitivity. The technique works through its sensitivity to the local environment, including the shape and size of the nanoparticle. With LSPR, the movement of electrons through the internal metal framework is restricted inducing a collective electron charge oscillation [62]. Consequently, there is an absorbance of light within the UV-VIS band and an appearance of an extinction band. The LSPR biosensing strategy is tracked by monitoring the changes/shifts in the extinction bands with the nature of the LSPR detection being dependent on the composition, shape, and size of the nanoparticles. One of the advantages of LSPR in biosensing is that the technique provides a higher surface area for the immobilization of the sensing probes [62].

2.7.1 Shifts in the LSPR Band

The ultimate aim of biosensing is to have a system that generates optimal signals using the lowest possible analyte concentration. The shape, size, type of metal nanoparticle, and the interaction of the analyte with the nanoparticle dictate the extinction spectrum and the refractive index sensitivity to the environment. The specific properties can be optimized to achieve the optimal localized surface plasmon resonance signal for any analyte being detected.

The shift in the LSPR band is one of the key aspects that is often evaluated in using LSPR biosensing. In this sensing mode, UV-VIS spectroscopy is employed where wavelengths of light that cause collective oscillation to happen are monitored. The changes in shifts in extinction wavelengths are monitored by assessing the continued influence of the refractive index of the adlayer due to the adsorption of the target analyte. Willets *et al*., [61] note that wavelength shifts are crucial in LSPR spectroscopy as they indicate changes in the local environment surrounding the nanoparticles. By monitoring these shifts, researchers can gain insights into interactions between nanoparticles and analytes, enabling sensitive detection and analysis of various substances. The ability to tune the LSPR peak wavelength based on nanoparticle characteristics makes LSPR spectroscopy a powerful tool for chemical and biological sensing applications.

LSPR peak shifts as a plasmonic sensor were demonstrated by Wu *et al*., [63] who adsorbed rhodamine 6G (R6G) on silver nano prisms. The research revealed that the enhancement of the LSPR peak shifts as a function of wavelength had three peaks while UV-Vis revealed that R6G had only two peaks. The conclusion drawn was that the analyte adsorbed on the nanoparticle not only enhances the LSPR peak shift but also provides more information on the adsorbing nature of the target analyte on the nanoparticle. Han *et al*., [64] exploited the resonant effect for biosensing. The authors explained that CYP101 which is a drug inhibitor that helps to metabolize drugs in the liver had a strong absorption at 417nm and redshifts by 8nm when bound by an inhibitor and 27nm when bound with a substrate [65]. Goul *et al*., [66] notes that the shift is a result of the change in the local refractive index which causes a red shift in the maximum wavelength.

Riboh *et al*., [67] also note that the shift in extinction wavelength of the LSPR spectrum of triangular silver nanoparticles whose size is between 50 to 90nm can be used to probe the interaction between an antigen that is confined within a surface, of a biotin and solution-phase antibody. Riboh et al., [67] content that the exposure of the silver nanotriangles to the target analyte results in a 38 nm red shift in the LSPR wavelength. The change in band position was evaluated against the concentration of the adsorbent. Peak shift can be used to track the response from the molecular binding and molecular aggregation. However, Deng *et al*., [68] note that in very small shifts induced by molecular binding, it is challenging to monitor such shifts for molecules that have very low molecular weight. The poor resolution in peak positions increases such challenges.

2.7.2 Broadening of the LSPR Band

The broadening of the LSPR band is one of the key considerations when leveraging localized surface plasmon resonance for sensing applications. The full width at half maximum can be defined based on the Figures of merit (FOM) indicator. The FOM is defined as the sensitivity divided by bandwidth in the case of a wavelength shift or by reference intensity in the case of an intensity shift as defined in Equation 2.1.

$$FOM_{\lambda} = \frac{S_{\lambda}}{FWHM} \qquad 2.1$$

Sensitivity on the other hand is defined in Equation 2.2.

$$S_{\lambda} = \frac{\Delta\lambda}{\Delta n} \qquad 2.2$$

Both sensitivity and figures of merit are dependent on the wavelength and shift in intensity. A higher resonance shift will be preferred at a small change in the refractive index for optimal sensitivity and figures of merit. Therefore, to achieve a good quality LSPR-based sensor, a large change in wavelength and a narrow resonance peak will be required [69]. The two factors explain the need to assess the full width and half maximum when assessing the quality of a localized surface plasmon-resonance-based sensor.

2.7.3 Silver Nanoparticles as a Core Shell

The core-shell structure of silver nanoparticles has played an important role in the nanoparticle’s utility in biomedical applications. Core-shell type nanoparticles are defined as materials that have an inner core structure as well as an outer shell that has different components. The core-shell structure of silver nanoparticles makes it unique in biomedical applications. The core-shell structure of silver nanoparticles is often measured using energy-dispersive X-ray spectroscopy. Nomoev *et al.*, [70] measured the concentration levels of silver and oxygen. The percentage concentration of these elements was higher for the unbound silver nanoparticle as compared to the bound silver nanoparticle. The interaction behavior of silver nanoparticles with a bound analyte helps to explain the core-shell structure of silver nanoparticles [71].

2.8 DFT Aided Vibrational Spectroscopy

The molecular structure information, the vibrational mode assignment, and the information on frontier molecular orbitals for any probe molecule are key in analyzing the complex structure of a molecule as well as the mechanism of enhancement defined in SERS [72]. Experimental SERS and conventional Raman often fail to provide molecular conformation and frontier molecular orbital data. The use of density functional theory has already been demonstrated to be effective in describing electronic states of atoms and molecules providing a complete understanding of the frontier molecular orbitals. DFT can be used to predict the spectrum information and provide molecular conformation. Using the B3LYP/6-311G** level of theory, Wu *et al.*, [73] successfully assigned vibrational modes of aflatoxin. Theoretical calculations have also been used to support experimental results in assigning both infrared and Raman vibrational bands. The highest occupied energy level and the lowest uncopied energy level have also been identified with the help of DFT making it possible to explore the enhancement mechanism of surface-enhanced Raman spectroscopy. Density function theory has been carried out using open-access software such as the Gaussian 09 program which gives a molecular electrostatic potential map that gives a detailed evaluation of the molecule and relevant charges. Potential energy distribution calculations are given by the vibrational energy distribution analysis (VEDA) program which allows the assigning of the vibrational spectra [74].

Modeling FTIR and Raman spectra using density functional theory calculations provides an opportunity for developing a SERS detection protocol. D'Arcangelo *et al*., [75] noted that it is possible to explore the spectroscopic properties of pharmaceutical ingredients commonly found in wastewater using density functional theory. The theoretical studies help in exploring the potential energy surface, identifying the stability of the structures, and accurately predicting the Raman response of the target pharmaceutical products in solution. Furthermore, the Raman and FTIR spectral information can be directly related to the concentration levels of the target pharmaceutical compounds.

2.8.1 Adsorption Studies of Analytes on Silver Nanoparticles

Analyzing the adsorption and binding behaviors of analytes on the surfaces of silver nanoparticles provides remarkable insights into their interaction mechanisms, knowledge that is valuable for designing surfaces with specific properties or functionalities based on nanoparticle interactions. While experimental techniques like X-ray photoelectron spectroscopy (XPS) and atomic force microscopy (AFM) can be used to understand this interaction, theoretical approaches like DFT and TD-DFT have emerged as reliable strategies for exploring nanoparticle/analyte interaction. Srisung *et al*., [76] explored the structure and interaction behavior of dithizone with silver nanoparticles by combining SERS and density functional theory calculations. The results showed that it is possible to decipher the interaction of dithizone on silver nanoparticles, including the molecular orientation during chemical interaction. Using DFT, the stable surface of the adsorption of dithizone on silver nanoparticles was explored.

SERS spectral features of alizarin adsorbed on silver nanoparticles were also explored by Dellini *et al.*, [77]. In this study, spectral features of the adsorbed analyte on the metallic nanoparticle were assessed at different species concentrations. The interpretation of experimental findings was done using DFT. The authors noted that by using DFT, it was possible to explore the shift of vibrational frequencies and the relative intensities when the analyte is adsorbed on the modeled Ag+ ion. The chemical interaction of alizarin and silver nanoparticles has also been modeled by Lofrumento *et al.*, [78] with the help of time-dependent density functional theory (TDDFT). The theoretically calculated SERS spectra were key in distinguishing the contribution of chemical and electronic enhancement mechanisms based on the assumption that the excitation energies of the clusters are comparable with the local plasmon energies of nanoparticles. Other than SERS, the UV-VIS, and Raman spectra were also calculated based on the assumption that the analyte was bound to silver nanoparticles through the oxygen atoms of the C=O functional groups in the molecule. Therefore, with the help of DFT and TD-DFT implemented in Gaussian or any program, it is possible to ascertain the vibrational frequencies of an analyte/nanoparticle complex and the SERS effect that is key in developing vibrational-based analytical techniques.

References

[1] M. van Bottenburg, A. Geeraert, and O. de Hon, “The World Anti-Doping Agency: Guardian of Elite Sport’s Credibility,” in *Guardians of Public Value: How Public Organisations Become and Remain Institutions*, A. Boin, L. A. Fahy, and P. ‘t Hart, Eds., Cham: Springer International Publishing, 2021, pp. 185–210. doi: 10.1007/978-3-030-51701-4_8.

[2] J. Mazanov, “*Vale* WADA, *ave* ‘World Sports Drug Agency,’” *Perform. Enhanc. Health*, vol. 2, no. 2, pp. 80–83, Jun. 2013, doi: 10.1016/j.peh.2013.08.014.

[3] “What We Do,” World Anti Doping Agency. Accessed: Feb. 23, 2024. [Online]. Available: https://www.wada-ama.org/en/what-we-do

[4] Y. Murofushi *et al.*, “The association between subjective anti-doping knowledge and objective knowledge among Japanese university athletes: a cross-sectional study,” *Front. Sports Act. Living*, vol. 5, Nov. 2023, doi: 10.3389/fspor.2023.1210390.

[5] D. Hughes, “The World Anti-Doping Code in sport,” *Aust. Prescr.*, vol. 38, no. 5, pp. 167–170, Oct. 2015, doi: 10.18773/austprescr.2015.059.

[6] “The Prohibited List,” World Anti Doping Agency. Accessed: Feb. 25, 2024. [Online]. Available: https://www.wada-ama.org/en/prohibited-list

[7] J. A. A. C. Heuberger and A. F. Cohen, “Review of WADA Prohibited Substances: Limited Evidence for Performance-Enhancing Effects,” *Sports Med. Auckl. Nz*, vol. 49, no. 4, pp. 525–539, 2019, doi: 10.1007/s40279-018-1014-1.

[8] J. Felix Joseph and M. Kristina Parr, “Synthetic Androgens as Designer Supplements,” *Curr. Neuropharmacol.*, vol. 13, no. 1, pp. 89–100, Jan. 2015.

[9] “Trenbolone - an overview | ScienceDirect Topics.” Accessed: Feb. 25, 2024. [Online]. Available: https://www.sciencedirect.com/topics/agricultural-and-biological-sciences/trenbolone

[10] L. A. Motsinger *et al.*, “Understanding the Effects of Trenbolone Acetate, Polyamine Precursors, and Polyamines on Proliferation, Protein Synthesis Rates, and the Abundance of Genes Involved in Myoblast Growth, Polyamine Biosynthesis, and Protein Synthesis in Murine Myoblasts,” *Biology*, vol. 12, no. 3, p. 446, Mar. 2023, doi: 10.3390/biology12030446.

[11] E. J. Durhan *et al.*, “Identification of Metabolites of Trenbolone Acetate in Androgenic Runoff from a Beef Feedlot,” *Environ. Health Perspect.*, vol. 114, no. Suppl 1, pp. 65–68, Apr. 2006, doi: 10.1289/ehp.8055.

[12] V. Wilson, C. Lambright, J. Ostby, and L. Gray, “In Vitro and in Vivo Effects of 17beta-Trenbolone: A Feedlot Effluent Contaminant,” *Toxicol. Sci. Off. J. Soc. Toxicol.*, vol. 70, pp. 202–11, Jan. 2003, doi: 10.1093/toxsci/70.2.202.

[13] L. O. Post, N. Bataller, M. Parkhie, and W. C. Keller, “Chapter 5 - Regulatory Toxicology,” in *Clinical Veterinary Toxicology*, K. H. Plumlee, Ed., Saint Louis: Mosby, 2004, pp. 28–45. doi: 10.1016/B0-32-301125-X/50008-X.

[14] K. Shahsavari nia, F. Rahmani, H. Ebrahimi Bakhtavar, Y. Hashemi Aghdam, and M. Balafar, “A Young Man with Myocardial Infarction due to Trenbolone Acetate; a Case Report,” *Emergency*, vol. 2, no. 1, pp. 43–45, 2014.

[15] P. C. A. Kam and M. Yarrow, “Anabolic steroid abuse: physiological and anaesthetic considerations,” *Anaesthesia*, vol. 60, no. 7, pp. 685–692, 2005, doi: 10.1111/j.1365-2044.2005.04218.x.

[16] R. L. Harries, G. De Paoli, S. Hall, and L. A. Nisbet, “A review of the analytical techniques for the detection of anabolic–androgenic steroids within biological matrices,” *WIREs Forensic Sci.*, vol. 6, no. 1, p. e1504, 2024, doi: 10.1002/wfs2.1504.

[17] M. Thevis, T. Kuuranne, H. Geyer, and W. Schänzer, “Annual banned-substance review: analytical approaches in human sports drug testing,” *Drug Test. Anal.*, vol. 7, no. 1, pp. 1–20, Jan. 2015, doi: 10.1002/dta.1769.

[18] E. Tudela, K. Deventer, L. Geldof, and P. Van Eenoo, “Urinary detection of conjugated and unconjugated anabolic steroids by dilute-and-shoot liquid chromatography-high resolution mass spectrometry,” *Drug Test. Anal.*, vol. 7, no. 2, pp. 95–108, Feb. 2015, doi: 10.1002/dta.1650.

[19] M. Putz, T. Piper, and M. Thevis, “Identification of Trenbolone Metabolites Using Hydrogen Isotope Ratio Mass Spectrometry and Liquid Chromatography/High Accuracy/High Resolution Mass Spectrometry for Doping Control Analysis,” *Front. Chem.*, vol. 8, 2020, Accessed: Feb. 22, 2024. [Online]. Available: https://www.frontiersin.org/articles/10.3389/fchem.2020.00435

[20] G. T. Ankley *et al.*, “A Critical Review of the Environmental Occurrence and Potential Effects in Aquatic Vertebrates of the Potent Androgen Receptor Agonist 17β-Trenbolone,” *Environ. Toxicol. Chem.*, vol. 37, no. 8, pp. 2064–2078, Aug. 2018, doi: 10.1002/etc.4163.

[21] I. R. Lewis and H. Edwards, *Handbook of Raman Spectroscopy: From the Research Laboratory to the Process Line*. CRC Press, 2001.

[22] S. Basaria, “Androgen Abuse in Athletes: Detection and Consequences,” *J. Clin. Endocrinol. Metab.*, vol. 95, no. 4, pp. 1533–1543, Apr. 2010, doi: 10.1210/jc.2009-1579.

[23] F. Mazzeo, F. D’Elia, and G. Raiola, “Drugs in sport: Doping development and ethical analysis,” *Sport Sci.*, vol. 11, pp. 106–112, Jan. 2018.

[24] L. S. M.Sc, “The Analytical Techniques Used to Detect Drug Misuse in Athletes,” AZoNano. Accessed: Feb. 25, 2024. [Online]. Available: https://www.azonano.com/article.aspx?ArticleID=5550

[25] W. Chen, X. Cheng, Y. Ma, and N. Chen, “Foodborne doping and supervision in sports,” *Food Sci. Hum. Wellness*, vol. 12, no. 6, pp. 1925–1936, Nov. 2023, doi: 10.1016/j.fshw.2023.03.001.

[26] J. Park *et al.*, “Drug testing at the 10th Asian Games and 24th Seoul Olympic Games,” *J. Anal. Toxicol.*, vol. 14, no. 2, pp. 66–72, 1990, doi: 10.1093/jat/14.2.66.

[27] E. Stojanović and D. Radovanović, “Historical development of analytical methods for anti-doping control,” *Phys. Educ. Sport Centuries*, vol. 4, no. 1, pp. 15–23, 2017, doi: 10.1515/spes-2016-0018.

[28] B. D. Ahrens, B. Starcevic, and A. W. Butch, “Detection of prohibited substances by liquid chromatography tandem mass spectrometry for sports doping control,” *Methods Mol. Biol. Clifton NJ*, vol. 902, pp. 115–128, 2012, doi: 10.1007/978-1-61779-934-1_10.

[29] C. Seger, “Usage and limitations of liquid chromatography-tandem mass spectrometry (LC-MS/MS) in clinical routine laboratories,” *Wien. Med. Wochenschr. 1946*, vol. 162, Nov. 2012, doi: 10.1007/s10354-012-0147-3.

[30] H. Geyer, W. Schänzer, and M. Thevis, “Anabolic agents: recent strategies for their detection and protection from inadvertent doping,” *Br. J. Sports Med.*, vol. 48, no. 10, pp. 820–826, May 2014, doi: 10.1136/bjsports-2014-093526.

[31] E. Olesti, J. Boccard, G. Visconti, V. González-Ruiz, and S. Rudaz, “From a single steroid to the steroidome: Trends and analytical challenges,” *J. Steroid Biochem. Mol. Biol.*, vol. 206, p. 105797, Feb. 2021, doi: 10.1016/j.jsbmb.2020.105797.

[32] A. Bodaghi, N. Fattahi, and A. Ramazani, “Biomarkers: Promising and valuable tools towards diagnosis, prognosis and treatment of Covid-19 and other diseases,” *Heliyon*, vol. 9, no. 2, p. e13323, Jan. 2023, doi: 10.1016/j.heliyon.2023.e13323.

[33] O. Barroso, D. J. Handelsman, C. Strasburger, and M. Thevis, “Analytical challenges in the detection of peptide hormones for anti-doping purposes,” *Bioanalysis*, vol. 4, no. 13, pp. 1577–1590, Jul. 2012, doi: 10.4155/bio.12.128.

[34] D. Feng *et al.*, “Ultrasensitive and rapid detection for multiple dopings in saliva and urine using surface-enhanced Raman spectroscopy,” *Spectrosc. Lett.*, vol. 56, no. 5, pp. 249–262, May 2023, doi: 10.1080/00387010.2023.2206474.

[35] S. Azimi and A. Docoslis, “Recent Advances in the Use of Surface-Enhanced Raman Scattering for Illicit Drug Detection,” *Sensors*, vol. 22, no. 10, p. 3877, May 2022, doi: 10.3390/s22103877.

[36] I. Izquierdo-Lorenzo, I. Alda, S. Sanchez-Cortes, and J. V. Garcia-Ramos, “Adsorption and Detection of Sport Doping Drugs on Metallic Plasmonic Nanoparticles of Different Morphology,” *Langmuir*, vol. 28, no. 24, pp. 8891–8901, Jun. 2012, doi: 10.1021/la300194v.

[37] M. Fleischmann, P. J. Hendra, and A. J. McQuillan, “Raman spectra of pyridine adsorbed at a silver electrode,” *Chem. Phys. Lett.*, vol. 26, no. 2, pp. 163–166, May 1974, doi: 10.1016/0009-2614(74)85388-1.

[38] I. Boginskaya *et al.*, “SERS-Active Substrates Nanoengineering Based on e-Beam Evaporated Self-Assembled Silver Films,” *Appl. Sci.*, vol. 9, no. 19, Art. no. 19, Jan. 2019, doi: 10.3390/app9193988.

[39] R. J. Murphy, D. Pristinski, K. Migler, J. F. Douglas, and V. M. Prabhu, “Dynamic light scattering investigations of nanoparticle aggregation following a light-induced pH jump,” *J. Chem. Phys.*, vol. 132, no. 19, p. 194903, May 2010, doi: 10.1063/1.3425883.

[40] J. D. Guingab, B. Lauly, B. W. Smith, N. Omenetto, and J. D. Winefordner, “Stability of silver colloids as substrate for surface enhanced Raman spectroscopy detection of dipicolinic acid,” *Talanta*, vol. 74, no. 2, pp. 271–274, Nov. 2007, doi: 10.1016/j.talanta.2007.06.001.

[41] E. Le Ru and P. Etchegoin, “Metallic colloids and other SERS substrates,” 2009, pp. 367–413. doi: 10.1016/B978-0-444-52779-0.00013-1.

[42] B. Tim, P. Błaszkiewicz, and M. Kotkowiak, “Recent Advances in Metallic Nanoparticle Assemblies for Surface-Enhanced Spectroscopy,” *Int. J. Mol. Sci.*, vol. 23, no. 1, p. 291, Dec. 2021, doi: 10.3390/ijms23010291.

[43] R. A. Sperling and W. J. Parak, “Surface modification, functionalization and bioconjugation of colloidal inorganic nanoparticles,” *Philos. Transact. A Math. Phys. Eng. Sci.*, vol. 368, no. 1915, pp. 1333–1383, Mar. 2010, doi: 10.1098/rsta.2009.0273.

[44] E. Kočišová and A. Kuižová, “Drop coating deposition Raman (DCDR) spectroscopy: fundamentals and potential applications,” *Appl. Spectrosc. Rev.*, vol. 0, no. 0, pp. 1–15, 2024, doi: 10.1080/05704928.2024.2314534.

[45] D. Zhang, Y. Xie, M. F. Mrozek, C. Ortiz, V. J. Davisson, and D. Ben-Amotz, “Raman Detection of Proteomic Analytes,” *Anal. Chem.*, vol. 75, no. 21, pp. 5703–5709, Nov. 2003, doi: 10.1021/ac0345087.

[46] A. Kuižová, M. Přikryl, M. Procházka, and E. Kočišová, “Drop coating deposition Raman (DCDR) spectroscopy of contaminants,” *Spectrochim. Acta. A. Mol. Biomol. Spectrosc.*, vol. 262, p. 120109, Dec. 2021, doi: 10.1016/j.saa.2021.120109.

[47] Y. Fleger and M. Rosenbluh, “Surface Plasmons and Surface Enhanced Raman Spectra of Aggregated and Alloyed Gold-Silver Nanoparticles,” *Int. J. Opt.*, vol. 2009, p. e475941, Jul. 2009, doi: 10.1155/2009/475941.

[48] Y. M. Narode, V. M. Mokashi, and G. K. Sharma, “Rhodamine 6G capped gold nanoparticles: A fluorescent probe for monitoring the radiation induced oxidation of Glutathione,” *J. Lumin.*, vol. 201, pp. 479–484, Sep. 2018, doi: 10.1016/j.jlumin.2018.05.011.

[49] K. Saha, S. S. Agasti, C. Kim, X. Li, and V. M. Rotello, “Gold Nanoparticles in Chemical and Biological Sensing,” *Chem. Rev.*, vol. 112, no. 5, pp. 2739–2779, May 2012, doi: 10.1021/cr2001178.

[50] A. M. Alkilany and C. J. Murphy, “Toxicity and cellular uptake of gold nanoparticles: what we have learned so far?,” *J. Nanoparticle Res.*, vol. 12, no. 7, pp. 2313–2333, Sep. 2010, doi: 10.1007/s11051-010-9911-8.

[51] “Effects of oxidation on the localized surface plasmon resonance of Cu nanoparticles fabricated via vacuum coating,” *Vacuum*, vol. 184, p. 109965, Feb. 2021, doi: 10.1016/j.vacuum.2020.109965.

[52] P. Zheng, H. Tang, B. Liu, S. Kasani, L. Huang, and N. Wu, “Origin of strong and narrow localized surface plasmon resonance of copper nanocubes,” *Nano Res.*, vol. 12, no. 1, pp. 63–68, Jan. 2019, doi: 10.1007/s12274-018-2178-6.

[53] M. A. Ordal *et al.*, “Optical properties of the metals Al, Co, Cu, Au, Fe, Pb, Ni, Pd, Pt, Ag, Ti, and W in the infrared and far infrared,” *Appl. Opt.*, vol. 22, no. 7, pp. 1099–1119, Apr. 1983, doi: 10.1364/AO.22.001099.

[54] Y. Li, Q. Liao, W. Hou, and L. Qin, “Silver-Based Surface Plasmon Sensors: Fabrication and Applications,” *Int. J. Mol. Sci.*, vol. 24, no. 4, Art. no. 4, Jan. 2023, doi: 10.3390/ijms24044142.

[55] S. K. Gahlaut, A. Pathak, and B. D. Gupta, “Recent Advances in Silver Nanostructured Substrates for Plasmonic Sensors,” *Biosensors*, vol. 12, no. 9, p. 713, Sep. 2022, doi: 10.3390/bios12090713.

[56] S. Unser, I. Bruzas, J. He, and L. Sagle, “Localized Surface Plasmon Resonance Biosensing: Current Challenges and Approaches,” *Sensors*, vol. 15, no. 7, pp. 15684–15716, Jul. 2015, doi: 10.3390/s150715684.

[57] F. Bensebaa, “Chapter 3 - Dry Production Methods,” in *Interface Science and Technology*, vol. 19, F. Bensebaa, Ed., in Nanoparticle Technologies, vol. 19. , Elsevier, 2013, pp. 147–184. doi: 10.1016/B978-0-12-369550-5.00003-3.

[58] Z. Zhang and P.-C. Lin, “Chapter 7 - Noble metal nanoparticles: synthesis, and biomedical implementations,” in *Emerging Applications of Nanoparticles and Architecture Nanostructures*, A. Barhoum and A. S. H. Makhlouf, Eds., in Micro and Nano Technologies. , Elsevier, 2018, pp. 177–233. doi: 10.1016/B978-0-323-51254-1.00007-5.

[59] K. Parveen, V. Banse, and L. Ledwani, “Green synthesis of nanoparticles: Their advantages and disadvantages,” *AIP Conf. Proc.*, vol. 1724, no. 1, p. 020048, Apr. 2016, doi: 10.1063/1.4945168.

[60] S. Mukherjee and C. R. Patra, “Biologically synthesized metal nanoparticles: recent advancement and future perspectives in cancer theranostics,” *Future Sci. OA*, vol. 3, no. 3, p. FSO203, May 2017, doi: 10.4155/fsoa-2017-0035.

[61] K. A. Willets and R. P. Van Duyne, “Localized surface plasmon resonance spectroscopy and sensing,” *Annu. Rev. Phys. Chem.*, vol. 58, pp. 267–297, 2007, doi: 10.1146/annurev.physchem.58.032806.104607.

[62] M. Forough, E. Bilgen, and Ö. Persil Çetinkol, “Chapter 6 - Biosensors for nucleic acid detection,” in *Advanced Sensor Technology*, A. Barhoum and Z. Altintas, Eds., Elsevier, 2023, pp. 173–233. doi: 10.1016/B978-0-323-90222-9.00021-2.

[63] C. Wu, E. Chen, and J. Wei, “Surface enhanced Raman spectroscopy of Rhodamine 6G on agglomerates of different-sized silver truncated nanotriangles,” *Colloids Surf. Physicochem. Eng. Asp.*, vol. 506, pp. 450–456, Oct. 2016, doi: 10.1016/j.colsurfa.2016.07.020.

[64] X. X. Han, R. S. Rodriguez, C. L. Haynes, Y. Ozaki, and B. Zhao, “Surface-enhanced Raman spectroscopy,” *Nat. Rev. Methods Primer*, vol. 1, no. 1, Art. no. 1, Jan. 2022, doi: 10.1038/s43586-021-00083-6.

[65] V. I. Chegel and A. M. Lopatynskyi, *Molecular Plasmonics: Theory and Applications*. Jenny Stanford Publishing, 2020.

[66] R. Goul *et al.*, “Quantitative analysis of surface enhanced Raman spectroscopy of Rhodamine 6G using a composite graphene and plasmonic Au nanoparticle substrate,” *Carbon*, vol. 111, pp. 386–392, Jan. 2017, doi: 10.1016/j.carbon.2016.10.019.

[67] J. C. Riboh, A. J. Haes, A. D. McFarland, C. Ranjit Yonzon, and R. P. Van Duyne, “A Nanoscale Optical Biosensor: Real-Time Immunoassay in Physiological Buffer Enabled by Improved Nanoparticle Adhesion,” *J. Phys. Chem. B*, vol. 107, no. 8, pp. 1772–1780, Feb. 2003, doi: 10.1021/jp022130v.

[68] S. Deng, P. Wang, and X. Yu, “Phase-Sensitive Surface Plasmon Resonance Sensors: Recent Progress and Future Prospects,” *Sensors*, vol. 17, no. 12, Art. no. 12, Dec. 2017, doi: 10.3390/s17122819.

[69] M. W. Juma, Z. Birech, N. M. Mwenze, A. M. Ondieki, M. Maaza, and S. D. Mokhotjwa, “Localized surface plasmon resonance sensing of Trenbolone acetate dopant using silver nanoparticles,” *Sci. Rep.*, vol. 14, no. 1, p. 5721, Mar. 2024, doi: 10.1038/s41598-024-56456-w.

[70] A. V. Nomoev *et al.*, “Structure and mechanism of the formation of core–shell nanoparticles obtained through a one-step gas-phase synthesis by electron beam evaporation,” *Beilstein J. Nanotechnol.*, vol. 6, pp. 874–880, Mar. 2015, doi: 10.3762/bjnano.6.89.

[71] M. Kahraman, Ö. Aydın, and M. Çulha, “Oligonucleotide-Mediated Au–Ag Core–Shell Nanoparticles,” *Plasmonics*, vol. 4, no. 4, pp. 293–301, Dec. 2009, doi: 10.1007/s11468-009-9105-3.

[72] R. Li, W. Ji, L. Chen, H. Lv, J. Cheng, and B. Zhao, “Vibrational spectroscopy and density functional theory study of 4-mercaptophenol,” *Spectrochim. Acta. A. Mol. Biomol. Spectrosc.*, vol. 122, pp. 698–703, Mar. 2014, doi: 10.1016/j.saa.2013.11.109.

[73] X. Wu, S. Gao, J.-S. Wang, H. Wang, Y.-W. Huang, and Y. Zhao, “The surface-enhanced Raman spectra of aflatoxins: spectral analysis, density functional theory calculation, detection and differentiation,” *Analyst*, vol. 137, no. 18, pp. 4226–4234, Aug. 2012, doi: 10.1039/C2AN35378D.

[74] M. H. Jamróz, “Vibrational Energy Distribution Analysis (VEDA): Scopes and limitations,” *Spectrochim. Acta. A. Mol. Biomol. Spectrosc.*, vol. 114, pp. 220–230, Oct. 2013, doi: 10.1016/j.saa.2013.05.096.

[75] G. D’Arcangelo, S. Legnaioli, F. Lipparini, and B. Campanella, “Raman, surface-enhanced Raman and density functional theory analyses of poorly soluble pharmaceuticals in water,” *Microchem. J.*, vol. 202, p. 110767, Jul. 2024, doi: 10.1016/j.microc.2024.110767.

[76] S. Srisung, N. Wasukan, M. Kuno, S. Somsri, and N. Tanjedrew, “Raman enhanced scattering and DFT studies on the adsorption behaviour of dithizone on silver nanoparticle,” *Inorg. Chem. Commun.*, vol. 126, p. 108480, Apr. 2021, doi: 10.1016/j.inoche.2021.108480.

[77] C. Gellini, M. Macchiagodena, and M. Pagliai, “Adsorption Geometry of Alizarin on Silver Nanoparticles: A Computational and Spectroscopic Study,” *Nanomaterials*, vol. 11, no. 4, p. 860, Mar. 2021, doi: 10.3390/nano11040860.

[78] C. Lofrumento, E. Platania, M. Ricci, M. Becucci, and E. M. Castellucci, “SERS Spectra of Alizarin Anion–Agn (n = 2, 4, 14) Systems: TDDFT Calculation and Comparison with Experiment,” *J. Phys. Chem. C*, vol. 120, no. 22, pp. 12234–12241, Jun. 2016, doi: 10.1021/acs.jpcc.5b12321.

3 Theoretical Background and Characterization Techniques

3.1 Introduction

This chapter provides an in-depth theoretical evaluation of both conventional Raman and surface-enhanced Raman spectroscopy (SERS) and the use of X-ray diffraction. The section also presents the basics of laser ablation in liquid, the theory of localized surface plasmon resonance sensing, and the different characterization techniques applied in this work. A detailed working of density functional theory (both in air and when simulation is done in the presence of a solvent like water) is also discussed. The working of transmission electron microscopy (TEM) will also be presented.

3.2 The Theory of Raman Spectroscopy

Raman spectroscopy can be explained from the basic principles of light interacting with matter. Such interaction can be used to explain both the Rayleigh scattering and Raman scattering where light is scattered elastically and inelastically, respectively. For elastic scattering which helps to explain Reighleigh, the energy of the incident photon and that of the scattered photon are the same. However, for inelastic scattering, there is a notable shift in the amount of energy after scattering. Although the change in energy of the photon can be very minimal, it helps to explain the principles of Raman spectroscopy [1]. The change in frequency of the scattered photons is also as a result of the vibrational and rotational states of the molecules after absorbing photons of sufficient energy.

In Raman, the inelastic scattering can be either a Stokes process or an anti-Stokes process. In Stokes Raman, an incident photon hv_o interacts with the molecular vibration hv_{vib}, and the scattering happens with a corresponding difference in energy $h(v_o - v_{vib})$ in what is called a redshift. The other one is the anti-Stokes Raman process where the photon absorbs enough photons before the photons get scattered with significantly more energy $h(v_o - v_{vib})$. Such a change in the number of photons is a blue shift which is important in explaining changes in the molecule as a result of both vibrational and rotational vibrations [2]. While this explanation is classical, quantum mechanically, the scattering is explained as a change in excitation state as particles move from a ground state to a virtual excited state.

As the sample absorbs enough amount of energy ΔE, the photons are then scattered with energy $hv - hv_{vib}$, which as explained before, explains Stoke's Raman. On the other hand, if the energy of the scattered photons is lower than the original number of photons, the photons will relax with energy$+hv_{vib}$, explaining anti-Stokes' Raman scattering. The energy level diagram describing the scattering process is described in *Figure 3-1*.

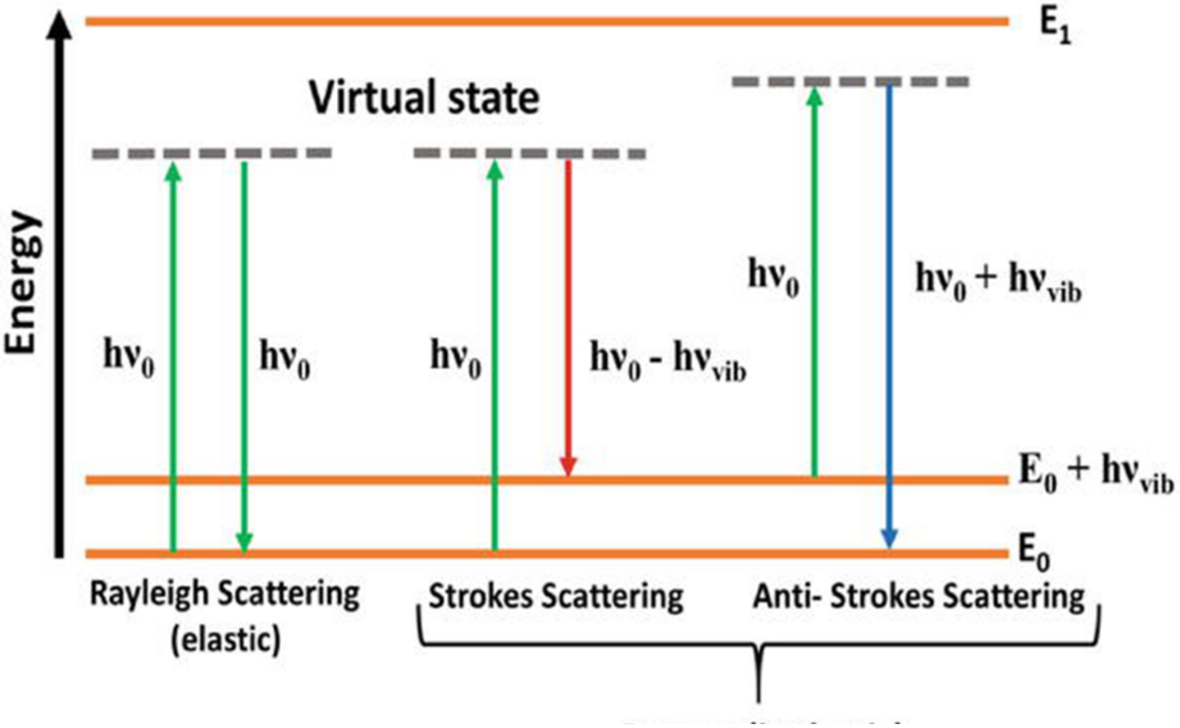

Figure 3-1:The diagrammatic representation of the energy transfer model showing Reyleigh, Stokes and Anti-stokes Raman scattering Thorsten et al., [3]

As indicated in Figure 3-1, the intensity of the anti-Stokes Raman scattering reduces rapidly as the shift in wavenumber increases. The reason is that the anti-Stokes Raman scattering entails transfer transitions to a rather lower energy state from a higher state populated with more electrons.

3.2.1 Classical Theory and mathematic Explanation of Raman Spectroscopy

The classical theory of Raman spectroscopy explains the Raman effect based on the polarizability of molecules and their interaction with an oscillating electric field of light. When a molecule is placed in an electric field E, it becomes polarized. The extent of polarization is given by the induced dipole moment μ, which is proportional to the polarizability α of the molecule [4]. These three variables are related as shown in Equation 3.1.

$$\mu = \alpha E \qquad 3.1$$

For an electromagnetic field that is strong enough, the electric field strength is given in Equation 3.2.

$$E = E_O \cos 2\pi \nu t \qquad 3.2$$

In equation 3.2, E_O denotes the amplitude of the electromagnetic wave. Equation 3.1 can be combined with equation 3.2 to replace E to give Equation 3.3

$$\mu = \alpha E_o \cos 2\pi \nu t \qquad 3.3$$

Equation 3.3 shows that when an EM radiation of enough frequency ν interacts with a sample, it introduces a molecular dipole moment that will oscillate with a similar frequency. However, the induced polarizability will change with small displacements from their equilibrium position giving molecular vibrations whose polarizability is defined by Equation 3.4.

$$\alpha = \alpha_o + (r - r_{eq})\frac{\partial \alpha}{\partial r} \qquad 3.4$$

Where, α_o describes the equilibrium polarizability, r_{eq} is the bond length given at the equilibrium position while r is the bond length at any given position. In the event of any harmonic motion by the molecule, the displacement is defined by Equation 3.5.

$$r - r_{eq} = r_{max} \cos 2\pi v_j\, t \qquad 3.5$$

$v_j$describes the frequency at which the molecule vibrates, r_{max} describes the optimal distance where different atoms based on their equilibrium positions. Equation 3.4 can be combined with 3.5 to give Equation 3.6.

$$\alpha = \alpha_o + \left(\frac{\partial \alpha}{\partial r}\right) r_{max} \cos 2\pi \nu_j t \qquad 3.6$$

Equation 3.6 can then be substituted into equation 3.2 to give;

$$\mu = \alpha E_o \cos 2\pi \nu t + E_o r_{max} \left(\frac{\partial \alpha}{\partial r}\right) \cos 2\pi \nu_j t \cos 2\pi \nu t \qquad 3.7$$

$$\mu = \alpha E_o \cos \underbrace{2\pi \nu t}_{\text{Reyleigh scattering}} + \frac{E_o}{2} r_{max} \left(\frac{\partial \alpha}{\partial r}\right) \cos\left[2\pi \underbrace{(\nu - \nu_j)}_{\text{Stokes scattering}} t\right] + \frac{E_o}{2} r_{max} \left(\frac{\partial \alpha}{\partial r}\right) \cos\left[2\pi \underbrace{(\nu + \nu_j)}_{\text{Anti-Stokes scattering}} t\right] \qquad 3.8$$

The combined equation 3.8 suggests that the excitation frequencies are based on the vibrational bond lengths and can be leveraged to give more information about the vibrational modes of any molecule of interest.

3.3 Theory of Surface-Enhanced Raman Spectroscopy

Conventional Raman is inherently weak due to the low probability of Raman scattering events occurring. Only about one in 10 million scattered photons undergo Raman scattering. This means that the Raman scattering cross-section, which represents the effective area for Raman scattering, is extremely small [5]. To resolve such a weakness, SERS is often used since it can achieve higher signal enhancements. The enhancement can be due to incident electric and magnetic photons perpendicularly interacting with metal nanoparticles or roughened surfaces that help to enhance signals. Target molecules attached to or near nanoparticles often experience plasmon resonances consequently amplifying Raman signals. In principle, SERS enhancement is a result of EM and chemical effects. EM enhancement is independent of the analyte while chemical enhancement is dependent on the probe and leverages the chemical interaction of the analyte on the metal surface.

3.3.1 Electromagnetic Enhancement Mechanism

EM enhancement explains a bigger percentage of the SERS enhancement effect. EM field enhancement is due to the roughness of the noble metal and its subsequent nanoparticle surfaces. Two phenomena can be used to explain EM field enhancement behavior in SERS as the material interacts with the roughened surface [6]. Firstly, close to the metal surface, there are electromagnetic waves that create a local field signal enhancement. Secondly, the radiation properties of the Raman dipole moment which was given in equation 3.1 can be affected by the metallic environment which consequently enhances the radiation signals. A critical evaluation of the two effects helps to explain the electromagnetic properties in SERS.

In local field enhancement, when EM radiations are directed at a metal surface that has a small positive imaginary and negative real dielectric constant, the EM field close to the metal surface is amplified. The amplification is a result of free electrons that oscillate freely resulting in surface plasmons that can be propagated in the X and Y planes of the dielectric material [7]. When nanoparticles are used instead of metal surfaces, an LSPR effect is realized due to the surface plasmons that are localized on the surface of a nanoparticle. The electromagnetic field enhancement mechanism is shown in Figure 3-2.

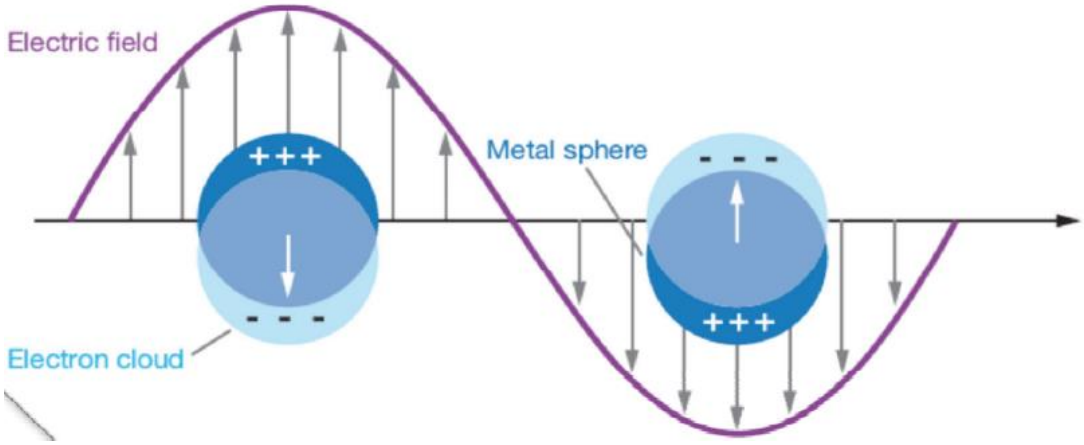

Figure 3-2:Schematic of the electromagnetic field enhancement used in SERS.

As shown in Figure 3-2, the enhancement in Raman signals is due to radiation fields interacting with the localized surface plasmons of the roughened surface or for nanoparticles. The LSPR is due to the resonance condition between the light's incident photons and the electron cloud generated from the nanoparticles. Consequently, there is a double oscillation of the conduction resulting in the large enhancement behavior witnessed in surface-enhanced Raman spectroscopy.

3.3.2 Chemical Enhancement Mechanism

In SERS, the chemical approach to signal enhancement aims to explain how signal enhancement is achieved through the exchange of chemical species between the analyte and adsorbent. The approach involves the formation of new electronic states or charge transfer transitions between the molecule and the metal surface, hence a better-scattering cross-section of the molecule. The approach is also defined as the charge transfer method where an electron-induced with sufficient energy moves from the Fermi level of the metal to the lowest unoccupied molecular orbital of adsorbate (LUMO) [8]. Similarly, the electron can move from the highest occupied molecular orbital (HOMO) to Fermin Level in retro-donation. The chemical enhancement mechanism often results in an enhancement in the order $10\text{-}10^2$. Figure 3-3 shows the HOMO and LUMO mechanisms for chemical enhancement.

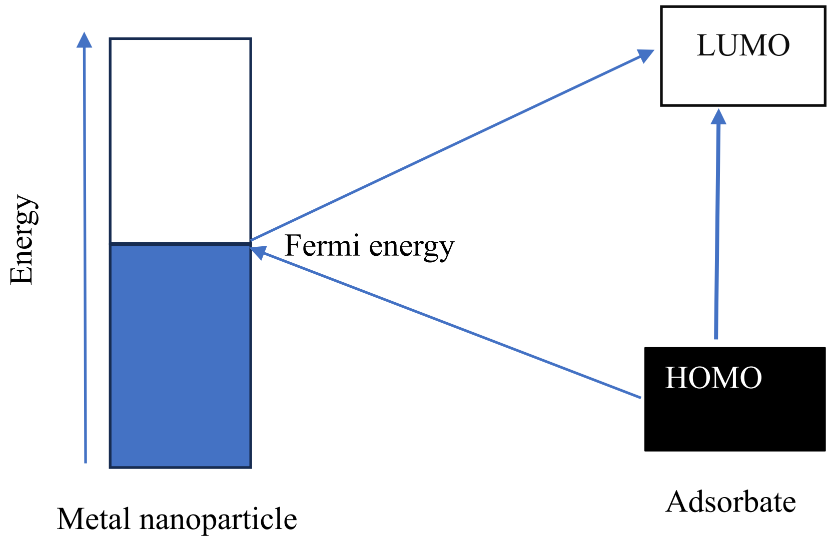

Figure 3-3: Schematic of the charge transfer for chemical enhancement

3.4 Localized Surface Plasmon Resonance

LSPR is an optical process that occurs when the light of sufficient energy interacts with conductive nanoparticles whose size is smaller than the wavelength of light. When such particles are irradiated with photons of sufficient energy, the oscillating electric field causes the conduction electrons in the nanoparticle to oscillate coherently, creating a localized surface plasmon [9]. Unlike the surface plasmon resonance where the induced plasmons oscillate along the metal-dielectric interface, in localized surface plasmon resonance, the induced plasmons oscillate locally to the nanostructure [10]. The absorption, which is wavelength selective eventually displays molar extinction coefficients that are as large as $3*10^{11}\mathrm{cm}^{-1}$.

LSPR can also be explained using the Mie scattering theory. The Mie solution to Maxwell's equation is important since it can be used to describe the scattering of an electromagnetic wave.

The theory also contends that the polarizability of a particle is a measure of its ability to be polarized by an external electric field. Equation 3.9 by Mariscal *et al*., [11] explains how the shape, and dimensions of the nanoparticles, and the overall environment impact the extinction.

$$E(\lambda) = \frac{24\pi N_A a^3 \varepsilon_m^{\frac{3}{2}}}{\lambda ln10}[\frac{\varepsilon_i}{(\varepsilon_r+\chi\varepsilon_m)^2+\varepsilon_i^2} \qquad 3.9$$

where N_A is the real density of the nanoparticle, a is its radius with the nanoparticle assumed to be spherical. ε_m is the medium's dielectric constant and it is assumed to be independent of the wavelength and it is also a positive/real integer. λ is the wavelength of the absorbing radiation while ε_i and ε_r are the imaginary and real parts of the dielectric function. Finally, χ is the nanostructure's aspect ratio.

The role of LSPR in detecting biomarkers in molecules and biosensing in general has already been demonstrated. One way in which the approach has been used in biosensing is by monitoring changes in the local environment of the surrounding nanoparticles and adsorbent. As analytes get adsorbed on the metal nanoparticles, there are measurable deviations in the localized surface plasmon resonance extinction wavelength since the adsorbed analyte will be dependent on the refractive index of the environment [9]. The refractive, index n relates with the extinction wavelength and dielectric constant as shown in equation 3.10.

$$\Delta\lambda_{max} = m\Delta n[1 - exp(-\frac{2d}{l_d})] \qquad 3.10$$

where, m describes the refractive index of the bulk and how it shifts as per the surrounding environment, d is the thickness of the adsorbate while l_d is the exponential decay length of the of the EM field. Therefore, monitoring the change in wavelength $\Delta\lambda_{max}$ which is a function of the decay length, the thickness of the adsorbate, and refractive index of the environment can help in explaining the role of LSPR in biosensing applications. The changes in the wavelength can be evaluated as a function of analyte concentration or time [12].

3.5 Theory of Laser Ablation in Liquid Technique

The laser ablation technique is one of the physical methods that has found great utility in synthesizing nanoparticles. Unlike biological and chemical mechanisms, the nanoparticles synthesized using laser ablation result in superior properties with the desired physical properties of the generated nanoparticles being easy to achieve [13]. Pulsed laser ablation also allows size control by changing the properties of the incident laser beam as well as the medium inside the ablation chamber. Laser ablation has also been used in the production of nanomaterials and the deposition of thin films. The continuous technique allows the production of colloid nanomaterials that are scalable and stable, advantages that have seen the technique attract diverse applications as shown in Figure 3-4.

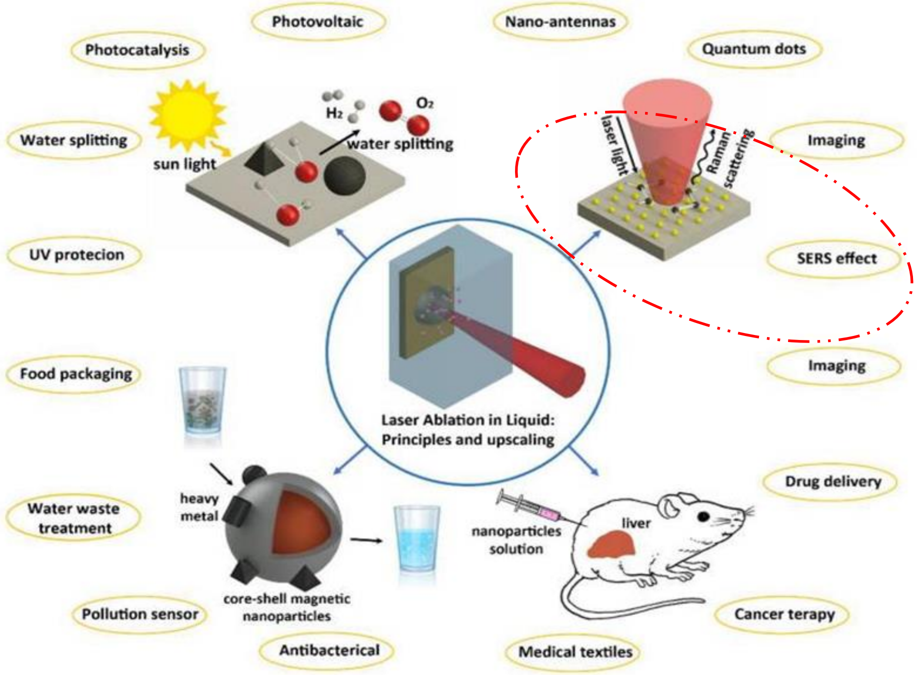

Figure 3-4: Diverse applications that can benefit from metallic nanoparticles synthesized using Laser ablation in the Liquid approach. The red dotted circle depicts the application in this thesis. Adopted from: National Library of Medicine

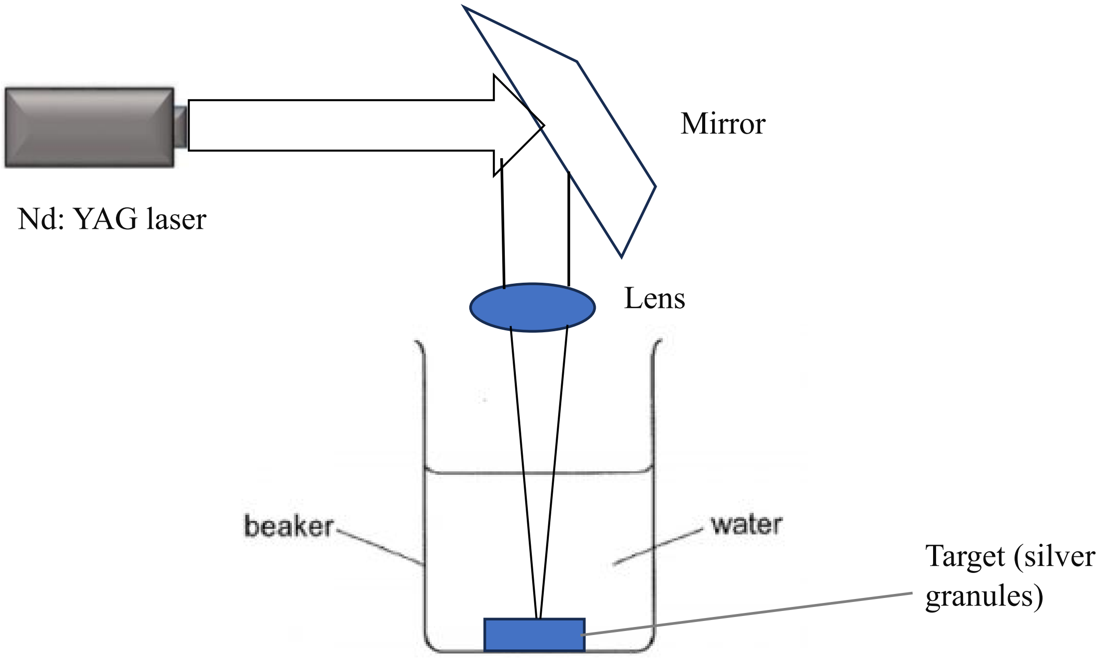

Figure 3-5: A simplified laser-liquid ablation set up. The laser source is focused on the metal target placed in water.

As shown in Figure 3-4, laser ablation in liquid has diverse applications including in water splitting, drug delivery, pollution sensing, and in surface-enhanced Raman spectroscopy applications [14]. Laser ablation in liquid is a technique that involves the interaction of a high-intensity laser beam with a solid target immersed in a liquid environment. The process is based on the principles of laser-solid interaction, which are modified by the presence of the surrounding liquid. When a high-intensity laser beam interacts with a solid target, it can lead to the ejection of material from the surface, forming a plasma plume. Figure 3-5 is the illustration of the laser ablation in liquid approach used in this work.

A Q-switch delayed laser source is directed at the target with sufficient energy such that particles are ejected from the ablated surface. The mechanism of generation of the nanoparticles is defined by different physical phases. As the laser irradiates the target, the absorption energy and temperature of the local liquid increase [15]. Consequently, the heated volume expands resulting in thermoelastic stress waves forming a vapor phase that comes in the form of bubbles. Most of the laser radiation is used in electron heating using inverse bremsstrahlung. Therefore, after irradiation, the ablated material changes to the plasma phase Maaza *et al.*, [15] and the generated nanoparticles are dependent on the nucleation rate of the bubbles. *Figure 3-6* shows the possible mechanism of how nanoparticles are generated using laser ablation in liquid technique.

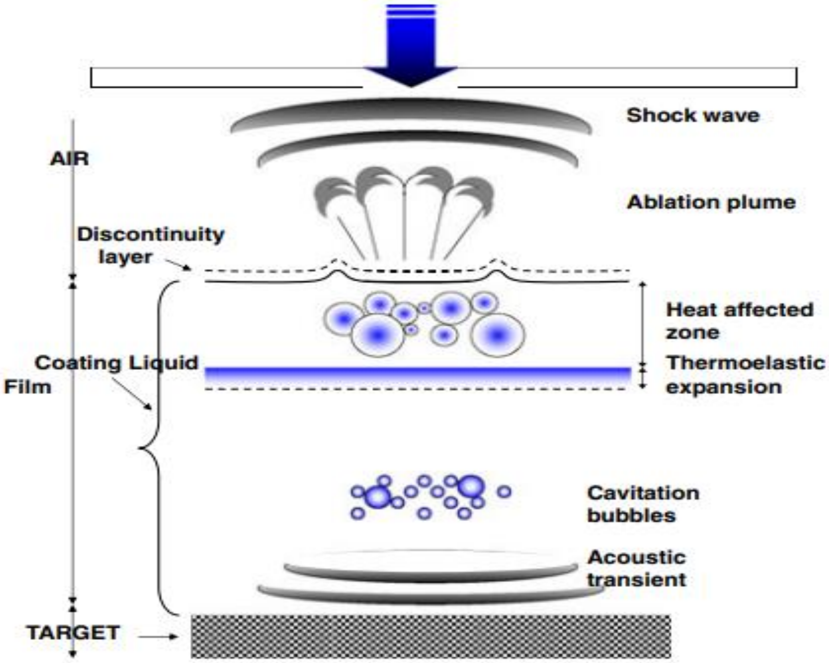

Figure 3-6: Mechanism of the formation of nanoparticles using laser ablation in liquid. Maaza *et al.,* [14]

As shown in Figure 3-6, the evaporated species undergo constant collision after they are ejected from the ablated metal surface. The collision leads to a plasma plume that forms the basis of laser ablation in liquid. Some of the factors that dictate the plume formation include the metal being irradiated, the liquid being used, and the energy of the laser [16]. In liquids, the plume can be quenched faster than in air. Therefore, there is a need for enough time to be allowed to achieve the target dynamic equilibrium [17]. Some of the optimization parameters that need to be evaluated using the laser ablation method are discussed under results and discussion.

3.6 Characterization Techniques

Characterization of a material is an important step through which the chemical, physical, and microstructure properties of a material are explored using a variety of analytical techniques.

Characterization forms the basic step through which the characteristics of a material are explored, and subsequently, the diverse applications that are likely to come from the characteristics of the material. The diverse analytical techniques provide critical insights into the properties of materials at both visible and invisible scales, aiding understanding of material behavior, developing new materials with specific properties, monitoring quality during processing, and evaluating performance in various applications.

This section will highlight a theoretical and practical description of the techniques that were employed in characterizing the prepared silver nanoparticles and the silver nanoparticle/trenbolone acetate complex. The characteristic techniques discussed in this section include scanning electron microscopy (SEM), Energy dispersive X-ray spectroscopy (EDS) and X-ray fluorescence spectroscopy (XRF), ultraviolet-visible spectroscopy (UV-VIS), Fourier-transform infrared spectroscopy (FTIR) and Raman spectroscopy.

3.6.1 Microscope-Based Characterization Technique

Microscope-based characterization techniques play a crucial role in analyzing materials at various scales. These techniques provide detailed insights into the structure and properties of materials.

3.6.1.1 Scanning Electron Microscope

Scanning electron microscopy has been used to characterize nanoparticles/nanomaterials due to its ability to provide high-resolution imaging of surfaces. SEM has been used to provide the surface morphology of the material. SEM uses an electron rather than light to image the surfaces. As shown in Figure 3-7, an electron beam is directed on the sample by heating a metallic filament to form an image.

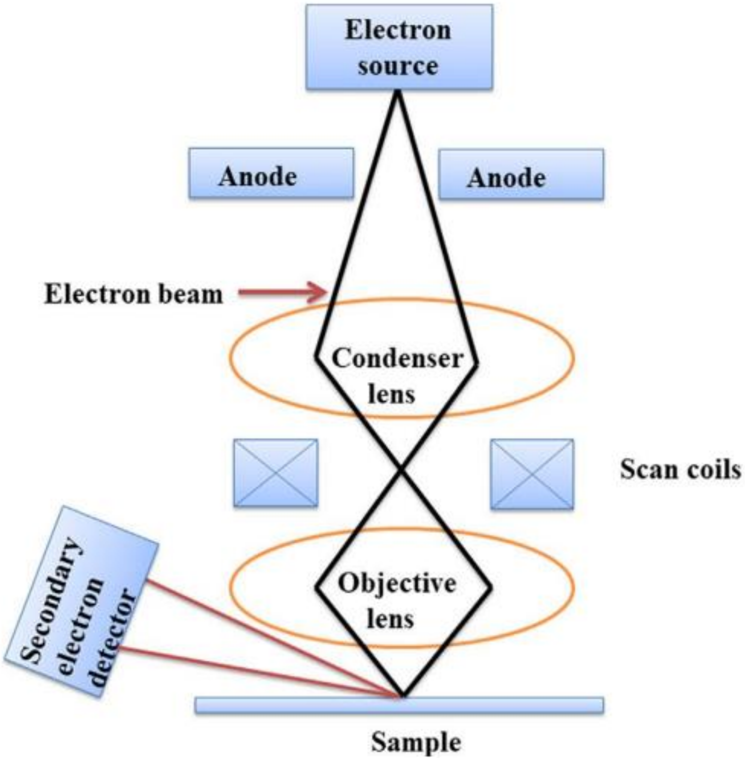

Figure 3-7: Principle of the SEM system employed in characterizing prepared silver nanoparticles.

The electron beams vertically/electromagnetically travel via the electromagnetic lenses which help to focus the beam on the sample. When the highly concentrated beam hits the sample surface, backscattered, secondary/auger, and X-rays are emitted. SEM leverages the backscattered electrons to examine the image of a sample which can be in the nanoscale. The electrons that have low energy are reflected giving insight into the material’s topography.

In this work, the surface morphology of the prepared silver nanoparticles and the AgNPs/trenbolone acetate complex was obtained with the help of scanning electron microscopy (SEM, Leo-Stero Scan 440). SEM produces images by scanning a focused beam of electrons over the surface of a sample and collecting the signals generated by the interactions between the electrons and the sample. The process begins with an electron gun at the top of the SEM column, which generates electrons through thermionic emission or field emission. These electrons are accelerated down the column by an electric field and focused by a series of electromagnetic lenses (condenser lenses and an objective lens) to create a fine beam. The focused electron beam is then deflected by scan coils in a raster pattern across the sample surface, scanning it line by line. The detected signals are processed and correlated with the beam's position on the sample. The processed signals are then used to create a grayscale image, which is displayed on a monitor in real time. The brightness of each pixel corresponds to the intensity of the detected signals.

3.6.1.2 Energy Dispersive X-Ray Spectroscopy

EDS was used together with SEM. EDS is a technique that allows elemental mapping of the sample, providing a reliable estimate of the proportion of elements in terms of concentration/intensity distributions. The EDS spectra provide the elemental composition using emitted X-rays from the material after the material absorbed a beam of electrons of sufficient energy. In the analysis, a high-energy beam of charged particles is focused on the material. The inner shells of the material are excited by electrons, providing the image of the sample. The SEM microscope is integrated with EDX and with an electron backscatter diffraction pattern detection and analysis system. EDS was employed on regions that were randomly selected on the sample surface using an acceleration voltage of between 7 to 10kV. The EDS characterization helped to provide profile maps of the elements and to perform sequence analysis of the particles from the regions of interest.

3.6.1.3 Transmission Electron Microscope

TEM is a powerful microscopy technique that uses electron beams to image and analyzes the structure of materials at the nanoscale. The technique works by transmitting electrons through thin sections of the sample, providing an idea about existing defects and the nature of the crystal. In TEM, electrons are accelerated at high voltage to high energy levels. The transmitted electrons form an image that is detected after interacting with the sample. Unlike a light microscope, TEM helps to achieve a much better resolution due to the smaller wavelength of electrons. A schematic diagram that demonstrates how TEM functions is provided in Figure 3-8.

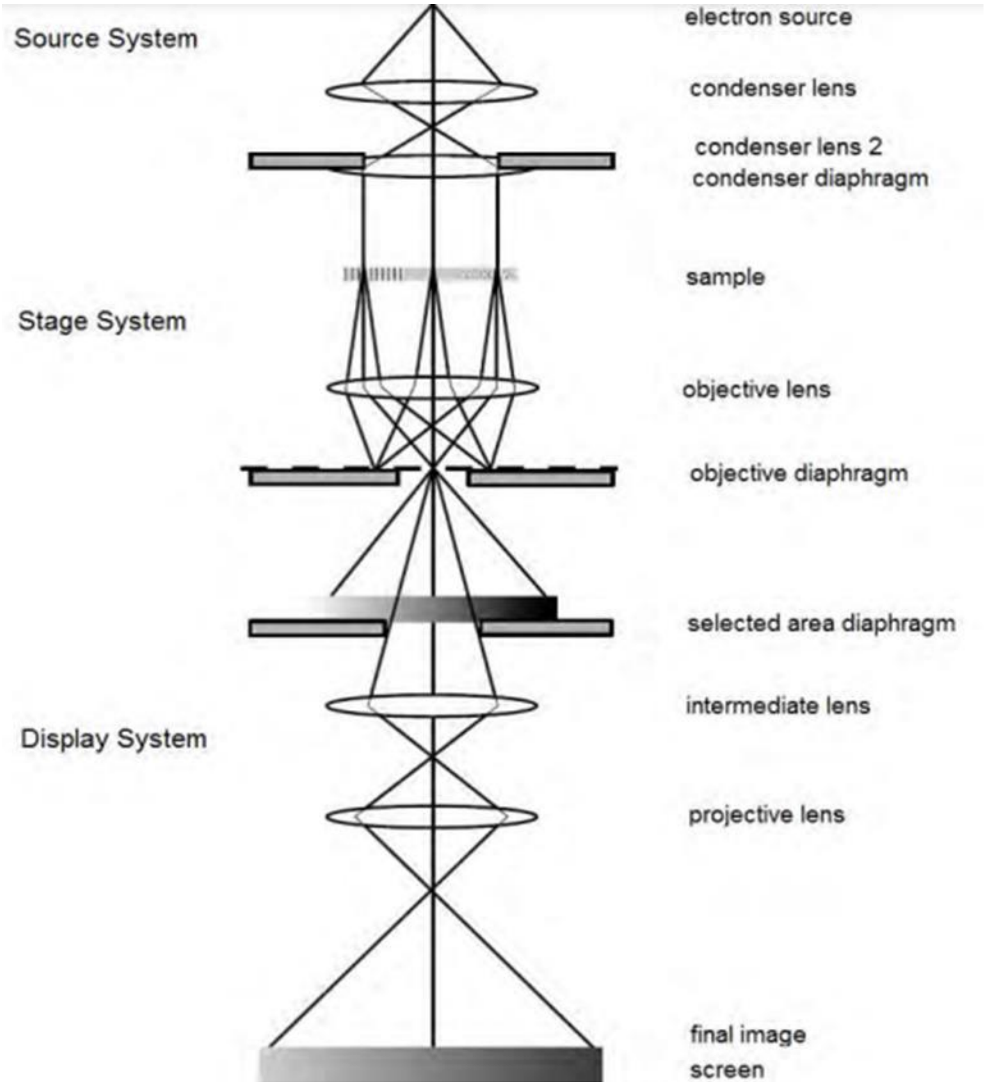

Figure 3-8: Schematic Diagram showing the working of Transmission Electron Microscopy (TEM) Da*s et al., [18]*

Figure 3-8 also shows the source of the electrons and how the lenses can be used to achieve diffraction patterns. As shown in the schematic, the TEM has a column equipped with different systems whose role is to control the beam being directed to the sample. The components are also important in producing images as well as diffraction patterns. The system is made of the source, a stage, and the display unit.

The source is by thermionic emission where electrons are released from the source gun before being directed to the sample through a system of lenses. The lenses aid in focussing the beam onto the sample on the stage system. After the lenses, there is an objective lens that creates the image from an electron signal which is transmitted through the sample where further magnification can be done. Thereafter, there is a system of several lenses that focus the image onto the CCD detector which projects the image for display on the digital screen.

3.6.2 Spectroscopy-based Characterization Techniques

Spectroscopy-based characterization techniques involve measuring a material's response to various frequencies of electromagnetic radiation to reveal its chemical composition, crystal structure, and photoelectric properties. This section will explore the theoretical analysis of the different spectral techniques employed in this work.

3.6.2.1 Ultraviolet-visible -NIR Spectroscopy

UV-Vis-NIR spectrophotometer is a reliable spectroscopic method often used to provide the optical properties of a material under study. The optical properties that the instrument analyses include absorbance, reflectance, and transmittance of the material. The technique works by assessing the interaction tendency of the sample with oncoming electromagnetic radiation. The UV-Vis-NIR spectroscopy wavelength range is from 200 to 2500nm which implies that it covers a wide range, from UV to NIR [19]. The ability of non-transparent materials to absorb, reflect, or scatter electromagnetic radiation makes it possible to explain the optical properties of the material. Figure 3-9 shows the typical schematic working of a UV-VIS spectrophotometer, with a detailed evaluation of how it provides optical characteristics of a material.

When characterizing nanoparticles, UV-VIS helps to provide a better picture of the plasmonic properties of the nanoparticles, including finding the optical band gap.

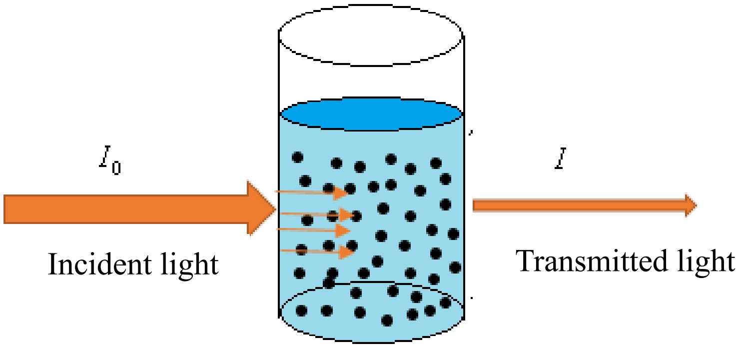

Figure 3-9: Schematic diagram which shows how a UV-VIS spectroscopy works.

The number of photons absorbed by a sample plays an important role in explaining the material's properties. Absorbance is described as the difference between the number of incident photons from the transmitted photons. The amount of light absorbed is also characteristic of the analyte concentration such that higher concentrations record better absorbance as defined by the Beer-Lambert law. The ratio of the intensity of light after passing through a sample to that before passing through the sample i.e. $\frac{I}{I_O}$ gives transmittance. The absorbance, which is often based on the transmittance can then be expressed as;

$$A = -log\frac{I}{I_o} \qquad 3.11$$

where A is the number of photons absorbed by a sample, I is the intensity of light after passing a sample, and I_o is the intensity of light after passing through a sample. Two external factors can be considered as key determinants when exploring absorbance. The first assumption is that the absorbance is directly proportional to the concentration of the solution for the sample employed in the experiment $A \propto c$. The second assumption is that absorbance has a direct correlation with the length of the light path which is also the same as the length l of the cuvette holding the sample ($A \propto l$). The two assumptions can be considered in Equation 3.11 to give Equation 3.12.

$$A = log\frac{I}{I_o} = \varepsilon cl \qquad 3.12$$

where ε is the constant of proportionality called molar absorptivity or the molar extinction coefficient that measures the probability of electronic transition. From equation 3.12, absorbance is directly related to the concentration of the adsorbing species as given by the Beer-Lambert law.

3.6.2.2 Fourier Transform Infrared Spectroscopy

FTIR spectroscopy works using infrared radiations that lie between visible and microwave radiation on the electromagnetic spectrum. Some of the infrared radiations are transmitted while others get absorbed which gives molecules their unique characteristic behavior. The working of FTIR in its characterization is based on the premise that every functional group/bond needs a different frequency for absorption [20]. Therefore, a characteristic peak is obtained for each of the functional groups or parts of the molecule under study.

When using FTIR, the light is often measured using an infrared spectrometer that produces an output of an infrared spectrum. The FTIR spectrum represents the graph of absorbed light against the wavelength. A block diagram depicting the mode of operation of FTIR is shown in Figure 3-10. Essentially, the FTIR uses an interferometer to measure the energy that goes into the sample.

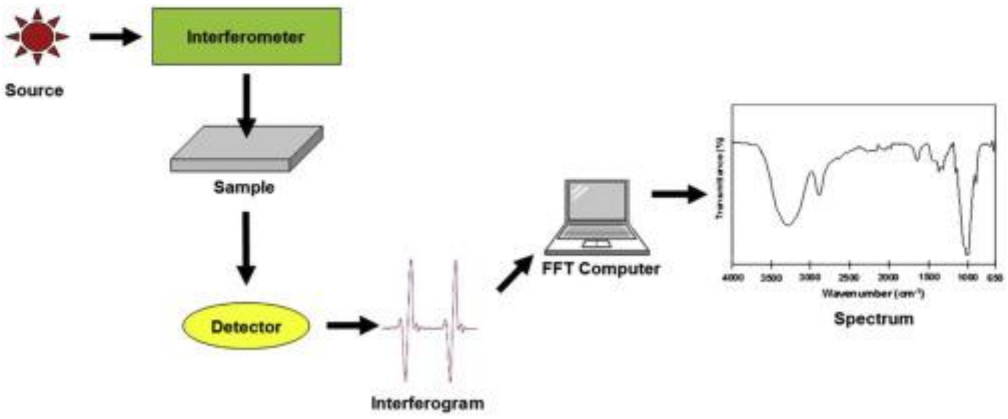

Figure 3-10: FTIR Spectrometer system.

3.6.2.3 Laser-Induced Breakdown Spectroscopy

Laser-induced breakdown Spectroscopy (LIBS) is a rapid, versatile, and sensitive analytical technique that uses a high-energy laser pulse to ablate a small amount of material from a sample's surface, creating a high-temperature plasma. The plasma emits light with characteristic wavelengths corresponding to the elements present in the sample. By analyzing the emitted light with a spectrometer, the elemental composition of the sample can be determined. A laser pulse of sufficient energy is focused on the sample, causing the removal of a small amount of material via thermal and non-thermal mechanisms, creating a microplasma. The ablated material interacts with the trailing portion of the laser pulse, forming a high-temperature plasma containing excited atoms, ions, and electrons. The emitted light is then recorded in the form of spectra/emission lines with the help of a CCD detector.

By comparing the intensities of the emission lines to those obtained from calibration standards, the concentrations of the elements in the sample can be determined. The difference in energy between the discrete energy levels occupied by the electrons in a given atom corresponds to specific energies described by the equation:

$$E = \frac{hc}{\lambda} \qquad 3.13$$

Where E describes the wavelength that can be observed visually in the resulting LIBS spectra, h is Planck's constant, c is the speed of light while λ is the wavelength.

3.6.3 X-Ray Based Characterization Technique

X-ray-based characterization techniques are essential in materials science for analyzing the structure and properties of materials. The focus of this section will be on the energy-dispersive X-ray fluorescence technique and X-ray diffraction that were used to characterize silver nanoparticles.

3.6.3.1 X-Ray Diffraction

X-ray diffraction is the most common approach used to study the crystal structure, chemical structure, and physical properties of materials under observation. Using X-rays, XRD helps in exploring the geometry and shape of molecules. It is based on the elastic scattering of X-rays from structures that have long-range order. The X-rays hitting the target sample get diffracted since the wavelength of the X-rays is of the same order as the inter-atomic spacing in the crystals [21]. Figure 3-11 show the schematic representation of the working of X-ray diffraction.

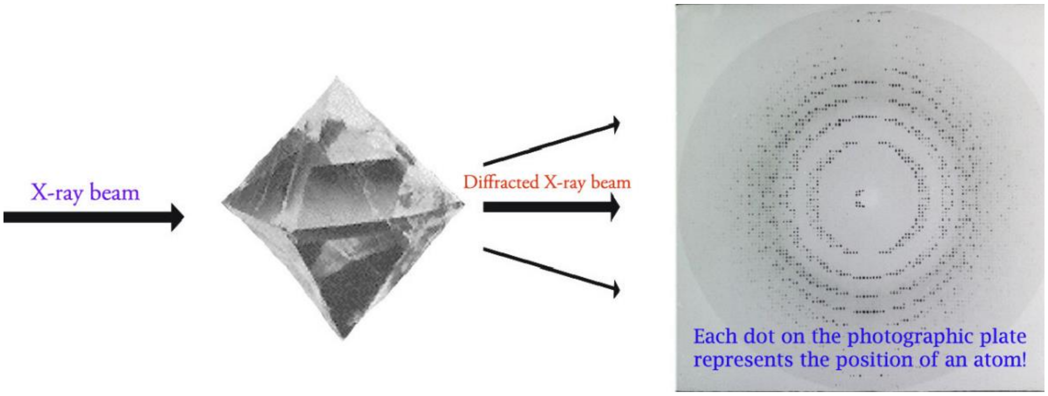

Each dot on the photographic plate represents the position of an atom!

Figure 3-11: Diffracted X-Ray Beam after hitting the sample.

When an X-ray beam strikes the orderly three-dimensional structures of atoms within a crystal, the majority of the X-rays will undergo destructive interference, effectively negating each other [22]. However, in certain specific orientations, the X-ray beams can interfere constructively, enhancing one another. It is this constructive interference of diffracted X-rays that generates the distinctive X-ray diffraction pattern, which is essential for determining the structure of the crystal.

According to Braggs, the X-rays are diffracted from a family of planes within a crystal and the relation can be given using Bragg's equation given in 3.14.

$$n(\lambda) = 2d\sin\theta \qquad 3.14$$

Here *n* is an integer (1,2, 3...n), λ is the wavelength, *d* is the distance between the atomic planes, and θ is the angle of incidence of the X-ray beams. For a given set of crystal lattice planes, the X-rays will be diffracted constructively if the path difference between the waves scattered from adjacent lattice planes is an integer multiple of the wavelength. This leads to the formation of a strong diffracted beam. When the particle size of the crystal is small, the diffracted beam tends to broaden. A schematic of an X-ray diffractometer is shown in Figure 3-12.

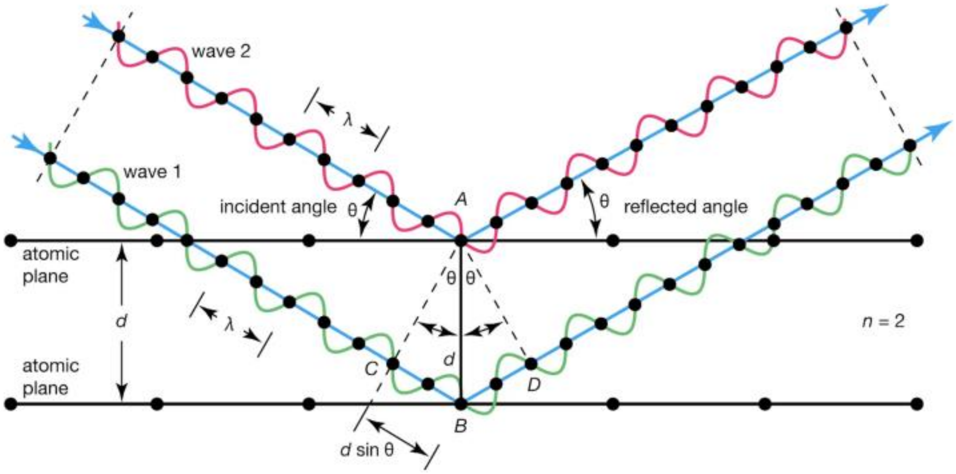

Figure 3-12: Schematic Diagram of an X-ray diffractometer.

The difference between the diffracted and incident X-ray beam dictated by the path length is significant since it provides more information about the structure, crystallography, and physical properties of the material under study. For this work, the XRD analysis was performed using an XPERT-PRO diffractometer system, which employed a monochromatic CuKα radiation source with a wavelength of 0.1541 nm. The diffraction pattern was measured within the angular range of 10 to 40 degrees, with a step size of 0.01671 degrees.

3.6.3.2 X-Ray Fluorescence

The XRF technique works through radiation interaction with a sample. The first principle of such interaction is through photoelectric absorption where the atoms fully absorb the radiation to produce X-rays whose energy gives information about the sample. The process of interaction of radiation with matter is described using Beer-Lambert law;

$$I_T = I_o e^{-\frac{\mu m}{A}} \qquad 3.15$$

where I_T is the intensity after transmission through matter, $is\ I_o$ the initial intensity, μ the mass attenuation coefficient, m is the mass of the sample, and A the irradiated area. Samples exposed to X-rays and gamma rays of shorter wavelengths are likely to undergo ionization of the atoms. The process of ionization involves electrons being ejected from the metal surface especially when the incident photons have energy that is higher than the ionization energy of the atoms. As the inner electron of the atoms is ejected, the atom becomes unstable. An outer electron then fills the hole left behind, releasing energy in the form of a photon. This emitted radiation has energy characteristics of the atoms present and is termed fluorescent radiation.

3.7 Density Functional Theory

DFT was developed in the 1960s as an alternative to the Hartree Fork providing better computational efficiency at lower costs. With DFT, it is possible to explore the properties of many-electron systems using functions of the spatially dependent electron density instead of wave functions. The theoretical model can be traced to the Thomas-Fermi model which assumes that an atom has uniform electron distribution.

In Hartree-Fock's theory, energy can be given in the form of equation 3.16.

$$E_{HF} = V + \langle hP \rangle + 1/2\langle PJ(P) \rangle - 1/2\langle PK(P) \quad 3.16$$

The individual terms can be defined as follows:

V describes the energy for the nuclear repulsion

$\langle hP \rangle$ - is kinetic plus potential

P describes the density matrix in the function

$1/2\langle PJ(P) \rangle$ - Classically, the function describes the electron Coulomb repulsion

$-1/2\langle PK(P) \rangle$ - Is negative since it is used to explain the exchange of energy due to the quantized nature of the electrons.

In DFT, it is important to consider the electron correlation energy, and as such, the equation can be changed to Equation 3.17.

$$E_{KS} = V + \langle hP \rangle + 1/2\langle PJ(P) \rangle + E_X[P] + E_C[P] \quad 3.17$$

where $E_X[P]$ describes the exchange component while $E_C[P]$ is correlational functionality.

3.7.1 The Basis Set Selection

Basis sets in the framework of density functional theory can be used for an accurate prediction of structural parameters and vibrational modes of a molecule under study. Choosing a basis set is crucial in DFT calculations because the accuracy and reliability of the results heavily depend on the quality and appropriateness of the basis set used. Since the system studied in this work was simply a single molecule with only 147 atoms, a 6-311++ G (d, p) basis set combined with the dispersion correlation functional Becke-Lee-Yang-Part (B3LYP) was considered. This basis set was selected since it has proven to be reliable and with improved accuracy in calculating geometries compared to other basis sets, making it suitable for obtaining precise molecular structures and properties. Similarly, when combined with the B3LYP functional, the 6-311++G (d, p) basis set offers good predictive power for the thermochemical properties of organic molecules, making it a popular choice for studying small organic molecules [23]. Greater basis sets have also been shown to be reliable since they provide better results as it is closer to the infinite basis set.

3.7.2 DFT in air and using a solvent

The use of Density Functional Theory (DFT) in air and employing any solvation process like the Integral Equation Formalism Polarizable Continuum Model (IEFPCM) in the original environment are significant considerations in computational chemistry. Like other solvation methods, IEFPCM accounts for the interaction between a solute molecule and its surrounding solvent environment, offering a practical way to simulate the effects of solvation during the interaction between the analyte and its environment.

Adekoya *et al*., [24] explains that when DFT is applied in the air, it allows for the accurate prediction of electronic properties and behaviors of molecules without considering the influence of solvation effects from the surrounding environment. This approach is particularly useful for studying isolated molecules or materials in vacuum or gas-phase conditions, providing a fundamental understanding of their intrinsic properties. Conversely, using IEFPCM in the original environment involves incorporating the effects of solvation into the computational model. This is crucial when studying molecules or materials in a solution or liquid phase, where interactions with the surrounding solvent significantly impact their behavior.

The IEFPCM method is the widely used method for modeling solvent effects. The IEFPCM method provides a computational approach that is efficient and helps to account for a solvent in DFT calculations by treating the solvent as a continuum with different dielectric constants. This approach allows for the consideration of the solvent's influence on the electronic structure and properties of molecules without explicitly including solvent molecules in the calculation, reducing the computational cost significantly.

In this work, DFT was carried out both in air and water using the IEFPCM solvation model. The overall aim of using the two approaches was to underscore the influence of water in predicting the vibrational behavior of the molecule. Including solvation effects in DFT analysis can help predict and interpret Raman and FTIR experimental results.

References

[1] G. Bruno, “Classical Theory of Rayleigh and Raman Scattering,” *Raman Eff.*.

[2] F. El-Diasty, “Coherent anti-Stokes Raman scattering: Spectroscopy and microscopy,” *Vib. Spectrosc.*, vol. 55, no. 1, pp. 1–37, Jan. 2011, doi: 10.1016/j.vibspec.2010.09.008.

[3] T. Schweizer, H. Kubach, and T. Koch, “Investigations to characterize the interactions of light radiation, engine operating media, and fluorescence tracers for the use of qualitative light-induced fluorescence in engine systems,” *Automot. Engine Technol.*, vol. 6, no. 3, pp. 275–287, Dec. 2021, doi: 10.1007/s41104-021-00092-3.

[4] J. R. Lombardi, “The theory of surface-enhanced Raman spectroscopy on organic semiconductors: J-aggregates,” *Chem. Phys. Lett.*, vol. 751, p. 137553, Jul. 2020, doi: 10.1016/j.cplett.2020.137553.

[5] K. Eberhardt, C. Stiebing, C. Matthäus, M. Schmitt, and J. Popp, “Advantages and limitations of Raman spectroscopy for molecular diagnostics: an update,” *Expert Rev. Mol. Diagn.*, vol. 15, no. 6, pp. 773–787, Jun. 2015, doi: 10.1586/14737159.2015.1036744.

[6] E. C. Le Ru, E. Blackie, M. Meyer, and P. G. Etchegoin, “Surface Enhanced Raman Scattering Enhancement Factors: A Comprehensive Study,” *J. Phys. Chem. C*, vol. 111, no. 37, pp. 13794–13803, Sep. 2007, doi: 10.1021/jp0687908.

[7] Y. S. Yamamoto, Y. Ozaki, and T. Itoh, “Recent progress and frontiers in the electromagnetic mechanism of surface-enhanced Raman scattering,” *J. Photochem. Photobiol. C Photochem. Rev.*, vol. 21, pp. 81–104, Dec. 2014, doi: 10.1016/j.jphotochemrev.2014.10.001.

[8] J. Kim *et al.*, “Study of Chemical Enhancement Mechanism in Non-plasmonic Surface Enhanced Raman Spectroscopy (SERS),” *Front. Chem.*, vol. 7, p. 582, Aug. 2019, doi: 10.3389/fchem.2019.00582.

[9] J. L. Hammond, N. Bhalla, S. D. Rafiee, and P. Estrela, “Localized Surface Plasmon Resonance as a Biosensing Platform for Developing Countries,” *Biosensors*, vol. 4, no. 2, pp. 172–188, Jun. 2014, doi: 10.3390/bios4020172.

[10] I. Ibrahim Zamkoye, B. Lucas, and S. Vedraine, “Synergistic Effects of Localized Surface Plasmon Resonance, Surface Plasmon Polariton, and Waveguide Plasmonic Resonance on the Same Material: A Promising Hypothesis to Enhance Organic Solar Cell Efficiency,” *Nanomaterials*, vol. 13, no. 15, p. 2209, Jul. 2023, doi: 10.3390/nano13152209.

[11] M. M. Mariscal, O. A. Oviedo, and E. P. M. Leiva, *Metal Clusters and Nanoalloys: From Modeling to Applications*. Springer Science & Business Media, 2012.

[12] J. C. Riboh, A. J. Haes, A. D. McFarland, C. Ranjit Yonzon, and R. P. Van Duyne, “A Nanoscale Optical Biosensor: Real-Time Immunoassay in Physiological Buffer Enabled by Improved Nanoparticle Adhesion,” *J. Phys. Chem. B*, vol. 107, no. 8, pp. 1772–1780, Feb. 2003, doi: 10.1021/jp022130v.

[13] S. Kumari *et al.*, “A comprehensive review on various techniques used for synthesizing nanoparticles,” *J. Mater. Res. Technol.*, vol. 27, pp. 1739–1763, Nov. 2023, doi: 10.1016/j.jmrt.2023.09.291.

[14] E. Fazio *et al.*, “Nanoparticles Engineering by Pulsed Laser Ablation in Liquids: Concepts and Applications,” *Nanomaterials*, vol. 10, no. 11, p. 2317, Nov. 2020, doi: 10.3390/nano10112317.

[15] M. Maaza *et al.*, “Valency control in MoO3−δ nanoparticles generated by pulsed laser liquid solid interaction,” *J. Nanoparticle Res.*, vol. 14, no. 2, p. 714, Jan. 2012, doi: 10.1007/s11051-011-0714-3.

[16] D. Diaz and D. W. Hahn, “Plasma chemistry produced during laser ablation of graphite in air, argon, helium and nitrogen,” *Spectrochim. Acta Part B At. Spectrosc.*, vol. 166, p. 105800, Apr. 2020, doi: 10.1016/j.sab.2020.105800.

[17] S. Cai *et al.*, “Expansion property of plasma plume for laser ablation of materials,” *J. Alloys Compd.*, vol. 773, pp. 1075–1088, Jan. 2019, doi: 10.1016/j.jallcom.2018.09.251.

[18] P. Das, “Optical Properties of Low Dimensional Structures Using Cathodoluminescence in a High Resolution Scanning Electron Microscope,” 2014. doi: 10.13140/RG.2.2.23943.39841.

[19] R. Anith Jose, D. Devina Merin, T. S. Arulananth, and N. Shaik, “Characterization Analysis of Silver Nanoparticles Synthesized from Chaetoceros calcitrans,” *J. Nanomater.*, vol. 2022, pp. 1–15, Sep. 2022, doi: 10.1155/2022/4056551.

[20] V. K. Undavalli, C. Ling, and B. Khandelwal, “Chapter 6 - Impact of alternative fuels and properties on elastomer compatibility,” in *Aviation Fuels*, B. Khandelwal, Ed., Academic Press, 2021, pp. 113–132. doi: 10.1016/B978-0-12-818314-4.00001-7.

[21] B. K. Mehta, M. Chhajlani, and B. D. Shrivastava, “Green synthesis of silver nanoparticles and their characterization by XRD,” *J. Phys. Conf. Ser.*, vol. 836, no. 1, p. 012050, Apr. 2017, doi: 10.1088/1742-6596/836/1/012050.

[22] A. A. Bunaciu, E. G. Udriştioiu, and H. Y. Aboul-Enein, “X-ray diffraction: instrumentation and applications,” *Crit. Rev. Anal. Chem.*, vol. 45, no. 4, pp. 289–299, 2015, doi: 10.1080/10408347.2014.949616.

[23] J. A. Plumley and J. J. Dannenberg, “A Comparison of the Behavior of Functional/Basis Set Combinations for Hydrogen-Bonding in the Water Dimer with Emphasis on Basis Set Superposition Error,” *J. Comput. Chem.*, vol. 32, no. 8, pp. 1519–1527, Jun. 2011, doi: 10.1002/jcc.21729.

[24] O. C. Adekoya, G. J. Adekoya, E. R. Sadiku, Y. Hamam, and S. S. Ray, “Application of DFT Calculations in Designing Polymer-Based Drug Delivery Systems: An Overview,” *Pharmaceutics*, vol. 14, no. 9, p. 1972, Sep. 2022, doi: 10.3390/pharmaceutics14091972.

4 Materials and Methods

This section explores the materials used in the study and the instrumentation used in synthesizing silver nanoparticles. The instrumentation of the Raman spectrometer and the FTIR system employed in the study was also explained. The last part is the computation approach to density functional theory and the use of Dmol$_3$ as employed using material Studio.

4.1 Materials

4.1.1 Trenbolone Acetate

Trenbolone acetate ([(8S,13S,14S,17S)-13-methyl-3-oxo-2,6,7,8,14,15,16,17-octahydro-1H-cyclopenta[a]phenanthren-17-yl] was sourced from Ultimate Precision Anabolic (UPA) and used without any further purification. The purity of trenbolone acetate as stated by the manufacturer was 99.99%. A syringe was employed to extract and dispense 2µl of trenbolone aliquot, including both pure samples and those with lower concentrations, onto a microscope slide wrapped in aluminum foil. Subsequently, Raman spectra were acquired by illuminating the sample, which had been allowed to dry on the prepared substrate (the aluminum foil-wrapped slide), using a laser.

4.1.2 Silver Nanoparticles

Analytical grade silver nanoparticles (99.9% pure) were acquired from Sigma Aldrich and ablated directly without any further purification. Silver granules were ablated in water using a Q-switch delayed 1064nm laser. The ablation time was optimized at 8 hours, the energy of the laser was 250mJ, and the pulse repetition frequency was 5Hz.

4.2 Instrumentation

4.2.1 Raman Spectrometer

All the Raman spectral measurements were carried out using a portable Raman spectrometer system (EZRaman-N portable Analyzer) from Enwave Optronics. The system is equipped with an EZRaman Analyzer software that allows background subtraction through Auto Baseline 2 and smoothing with the help of Boxcar which was set at 1. The system was equipped with a 785nm laser and the optimized parameters were laser power set at 150mW, exposure time, and spectral accumulations of 5. The measurements were done over the 100cm^{-1}-4000cm^{-1} spectral range and analyzed in the "fingerprint" spectral region of 500-1800 cm. The spectral resolution of the Raman system used was 7cm^{-1}.

4.2.2 FTIR Spectroscopy

FTIR spectra were recorded using Spectrum Two (PerkinElmer, USA) within the spectral range 4000cm^{-1} to 400cm^{-1} with a resolution of 4cm^{-1}. The analysis was carried out by placing the analyte sample in a unit cell before the spectra were acquired in transmission mode. All the spectra were plotted using OriginPro 2021, version 9.8.0.200.

4.3 Computational Details

This sub-section presents details for the theoretical calculations employed in the study with an emphasis on how pristine silver nanoparticles /Ag (1 1 1) slab and trenbolone acetate adsorbate were optimized and binding energies obtained.

4.3.1 DFT Analysis of Trenbolone Acetate

Theoretical computations of Trenbolone acetate were performed using Gaussan09W while the molecular visualization was done through Gauss View 6. The molecule was optimized using B3LYP which is a functional hybrid approach in combination with the 6-31G (d, p) basis set which is a functional correlation exchange of the Becke-Lee-Yang-Part and the most used DFT method. The same level of theory was used for vibrational frequency analysis. The basis set is the most commonly used due to its speed accuracy and ability to provide reproducible vibrational frequency results [1].

Harmonic vibrational numbers for infrared spectroscopy and Raman spectroscopy intensities were analytically calculated after fully optimizing the molecular geometries without any symmetry restrictions. Vibrational frequencies/wavenumbers (real harmonic) for the molecule were obtained proving the localization of the global minima on the potential energy surfaces. The calculated vibrational modes were displayed using Gauss View-05 software. The obtained vibrational frequencies were properly assigned through potential energy distribution (PED) analysis of the basic modes with the help of the VEDA 4 program. DFT helped to provide a solid foundation of the theoretically calculated Raman spectra while the PED analysis was performed to achieve vibrational assignment and understand the structural-vibrational properties of the trenbolone acetate.

4.3.2 Geometry Optimization

To find the most optimized geometry, energy calculations were done using the 6-311++ G (d, p) basis set. The molecule together with the numbering of the atoms is shown in Figure 4-1.

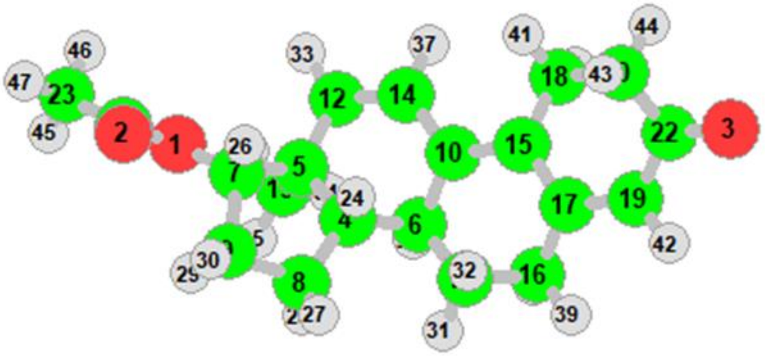

Figure 4-1:Molecular model of Trenbolone acetate molecule with the atom numbering system as appears in VEDA 4 program.

The global minimum electronic energy obtained in the optimization process was -996.9 Hartrees without the solvent while with the solvent (water) was -1000.34 Hartrees for the same basis set. The structural parameters obtained from the optimization process formed the hallmark for computing the vibrational frequencies of the molecule at the defined basis set and level of theory. Each characteristic in a molecule has a specific vibrational behavior and when coupled in systems, can change frequencies and intensities.

4.3.3 Dmol$_3$ in Materials Studio

Adsorption studies of trenbolone acetate on silver nanoparticles were carried out using DMoL3 implemented in Biovia Materials Studio. The user interface complied with Windows standards making it possible for quantum mechanical calculations. To ensure the optimization of the most feasible adsorption site on the substrate surface, the adsorption locator module in the materials studio was used. The adsorption locator uses Monte Carlo in a lattice dynamics style to come up with the most feasible lattice configuration. The optimized configuration parameters were then used as inputs for the subsequent DFT calculations. The work leveraged the face-centered cubic of Ag (1 1 1) when constructing the slab and the unit cell optimization was set at 4.02 Å.

The first step was to import trenbolone acetate (3-D atomistic model) from PubChem. The next step was to build the structure and the supercell of silver where the lattice parameters were length a=b = 4 Å. While building a supercell, the spectral range was set at 5 Å giving the length of the slab as ≈ 20 Å. The length was found to be feasible since the longest side of trenbolone acetate was 13.8 Å. The extra length was to allow the molecule to freely adsorb on the substrate without overlapping.

The next step was to independently do geometry optimization of the adsorbate and the adsorbent. During optimization, the quality was set to fine, and the function used was General Gradient Approximation (GGA) with Perdew Burke Ernzerhof (PBE) which provides better total energies during optimization.

After the molecules and substrates were optimized, the next step was to adsorb the molecule on the substrate with the help of an adsorption locator. In the adsorption locator setup, the quality used was medium and three cycles were used with 15,000 steps to reduce the time for calculation and to achieve better accuracy. The optimized structure of trenbolone acetate was introduced as the adsorbate on the optimized silver slab. Some of the properties that were explored in the adsorption calculations include adsorption energies, the total density of states projected density of states, and the energy distribution.

References

[1] J. A. Plumley and J. J. Dannenberg, “A Comparison of the Behavior of Functional/Basis Set Combinations for Hydrogen-Bonding in the Water Dimer with Emphasis on Basis Set Superposition Error,” *J. Comput. Chem.*, vol. 32, no. 8, pp. 1519–1527, Jun. 2011, doi: 10.1002/jcc.21729.

5 Results and Discussion

This section is divided into four sub-sections, as per the objectives of the study. The first section explores results obtained for the synthesized pristine silver nanoparticles and their characterization using different techniques. The second part explains localized surface plasmon resonance studies of trenbolone acetate. The third sub-chapter looks at how silver nanoparticles can be used as substrates in surface-enhanced Raman spectroscopy. This is followed by sub-chapter 4 and sub-chapter 5 which present results on the DFT study of trenbolone acetate and the adsorption of trenbolone acetate on silver nanoparticles respectively.

5.1 Laser Ablation in Liquid and Characterization of Synthesized Silver Nanoparticles

This sub-section describes the optimization process used in generating silver nanoparticles using the laser ablation in liquid (LAL) technique. Thereafter, generated nanoparticles were characterized using both microscope-based, spectroscopy-based, and X-ray-based analytical methods. Some of the parameters that will be explored in optimizing the LAL approach include ablation time, pulse repetition rate, and laser energy.

5.1.1 Colloidal Silver Nanoparticles

To generate silver nanoparticles, analytical grade silver nanoparticles (99.99% pure) were used as the target. The silver granules were put in a beaker containing 10ml of distilled water and then an Nd: YAG 104nm Q-switch delayed laser was focused on the target to generate silver nanoparticle colloids. During ablation, the beaker containing water was manually moved to ensure the surface was evenly ablated and to generate evenly distributed nanoparticles. The generated nanoparticles were inspected physically for color change. Figure 5-1 shows the yellowish and brownish color of the nanofluid after ablation which shows evidence of silver nanoparticles.

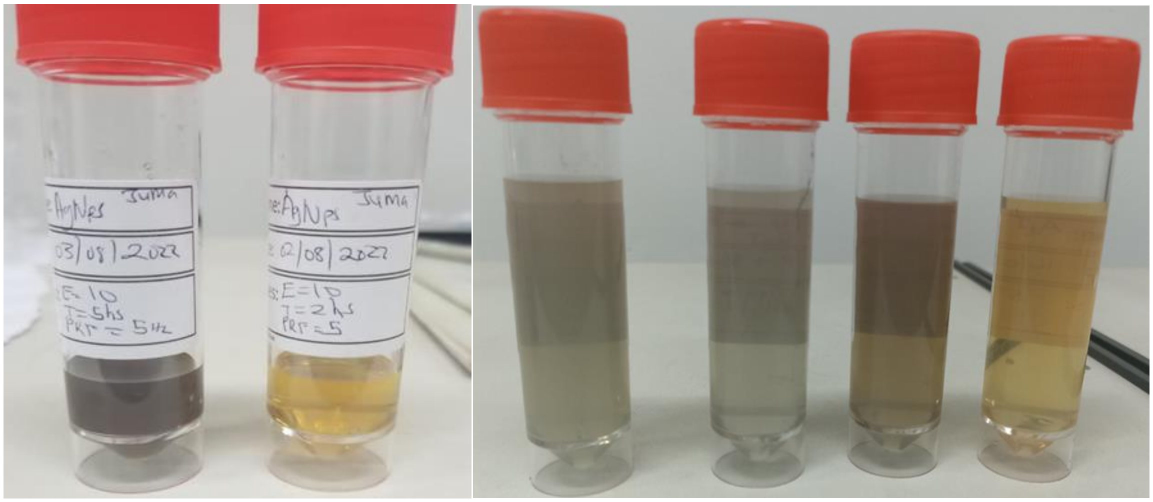

Figure 5-1: Observed color change on the silver nanofluids prepared at different ablation times.

Significant research has linked the yellow-brownish color to the presence of silver nanoparticles. Alhamid *et al*., [1], Mulfinger *et al*., [2], and Hussain *et al*., [3], have all confirmed that colloidal silver nanoparticles are yellowish. The yellow color confirms the plasmonic effect due to the vibrating lattice atoms within the silver nanoparticles. The color change from yellow to brown has also been shown to depict the presence of silver nanoparticles. Therefore, the physical inspection and observation of the change of color in the nanofluid provided a preliminary way of confirming that the generated nanoparticles are indeed silver. Lyane *et al.*,[4] explain that the change in the color of the nanofluid provides the basis for understanding the optical properties of silver nanoparticles as explored using UV-VIS and Raman spectroscopy among other techniques in the subsequent section.

5.1.2 Characterization of Silver Nanoparticles

Characterizing nanoparticles by exploring their physicochemical properties (size, shape, structural crystallography, etc.) is an important step in assessing their subsequent applications. Accurate and valid information about nanoparticles using different characterization techniques helps to ascertain their therapeutic and diagnostic efficacies and other applications that are dependent on the particle’s physicochemical properties. This section discusses how silver nanoparticles were characterized using different methodologies.

5.1.2.1 X-ray Diffraction

The crystallinity of the synthesized silver nanoparticles was examined using X-ray diffractometry (XRD) in the Bragg–Brentano geometry. There were three visible peaks centered at $2\theta = 19.06^{\circ}$, $27.59^{\circ,}$ and 40° corresponding to (1 1 1) which was the sharpest peak; (2 0 0) and (2 2 0) planes which belong to the face-centered cubic (FCC) crystalline AgNPs structure. The peak positions of the planes are shown in Figure 5-2.

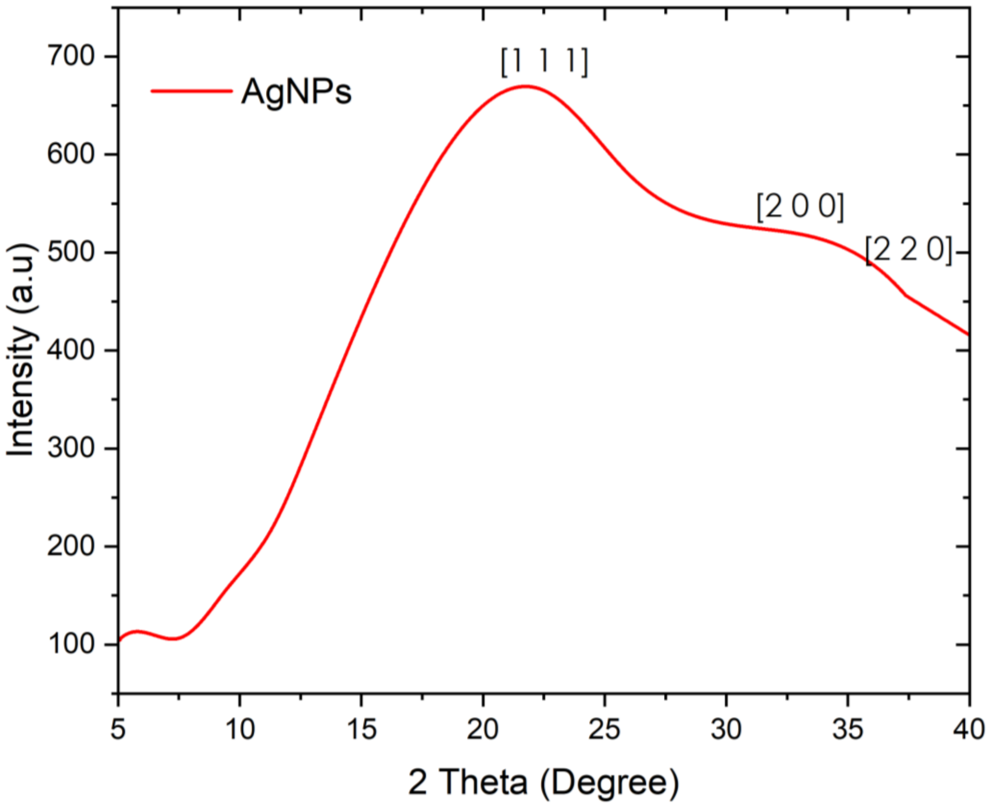

Figure 5-2: XRD Spectra of laser ablated silver nanoparticles.

As shown in Figure 5-2, there were no other peak planes corresponding to unexpected phases within the spectra which shows that the synthesized silver nanoparticles were pure. The miller indices and the angle are shown in table 5-1.

Table 5-1: Miller indices from XRD Spectra.

Miller Indices	2θ degrees	θ radians
1 1 1	19.06°	9.53
2 0 0	27.59°	13.79
2 2 0	40.46°	20.23

The appearance of a large intense peak at 19.06° and a small peak at both 27.59° and 40.46° both confirm the presence of silver nanoparticles. The broad peak corresponds to the face-centered cubic (F C C) crystalline planes.

Using the most intense band at 19.06°, the crystalline size was obtained based on the Scherrer equation below.

$$D = \frac{K\lambda}{\beta cos\theta} \qquad 5.1$$

In equation 5.1, D is the average crystalline size, K is the Scherrer constant provided as 0.94 since the silver nanoparticles are spherical, β is FWHM given in radians, θ is the Bragg's angle in degrees. λ is the X-ray wavelength where for CuK_{α}, the value is 1.54 Angstroms or 0.154nm.

The value of FWHM based on the band at [1 1 1] was obtained from the origin as 0.98 and in terms of radians, the value of FWHM is 0.017 radians.

Therefore, substituting the values in equation 5.1, the crystalline size can be given as;

$$D = \frac{0.94 * 0.154}{0.017 * \cos 13.6} = \frac{0.14476}{0.017 * 0.972} = 0.014476/0.0165 \approx 9\text{nm}$$

The results obtained using TEM for the same samples (nanoparticles synthesized using 8 hours of ablation time) showed the particle size to be 10nm. Therefore, the results obtained using TEM and XRD are almost similar with a minimal slight deviation.

5.1.2.2 UV-VIS Spectroscopy

UV-VIS spectrophotometry was carried out to further confirm the presence of the nanoparticles. The results indicated a surface plasmon band at 408nm which is an indication of the presence of the nanoparticles. Several authors have reported the silver nanoparticle absorbance between 400 and 450nm with the variation being a result of the technique used to synthesize the nanoparticles or the base liquid in the case of the laser ablation method. For biological methods that leverage the use of leaf extracts, Agustina *et al*., [5] reported a localized surface plasmon resonance peak of 400nm. Fernández-Arias *et al*., (2015) [6] also reported an LSPR peak at 402nm when using water as the base liquid. Therefore, the results obtained for this work were consistent with what has been reported by other authors. This section focuses on the optimization parameters that were used to characterize silver nanoparticles.

5.1.2.3 Ablation Time

Ablation time can be defined as the time required for a significant mass to be ejected from a metal target after exposure to laser radiation. Varying ablation time has been shown to have diverse physiochemical effects on the generated nanoparticles. In terms of particle size, Mafuné *et al*., (2000) have reported that more time is used to ablate the sample results in nanoparticles with smaller sizes. An increased ablation time also led to higher ablation mass as evidenced by an absorption band that has an increased intensity. Bhuiyan *et al*., (2015) [7] reported that an increase in ablation time leads to nanoparticles that are finer and with narrow size distributions. The effect of ablation time on UV-Vis peak intensity has also been investigated by Baladi *et al*., [8]) using a 1064 nm laser with an energy of 250mJ and ethanol as the base liquid. The conclusion drawn was that an increase in time leads to a higher concentration of the nanoparticles which is similar to the results obtained in this research.

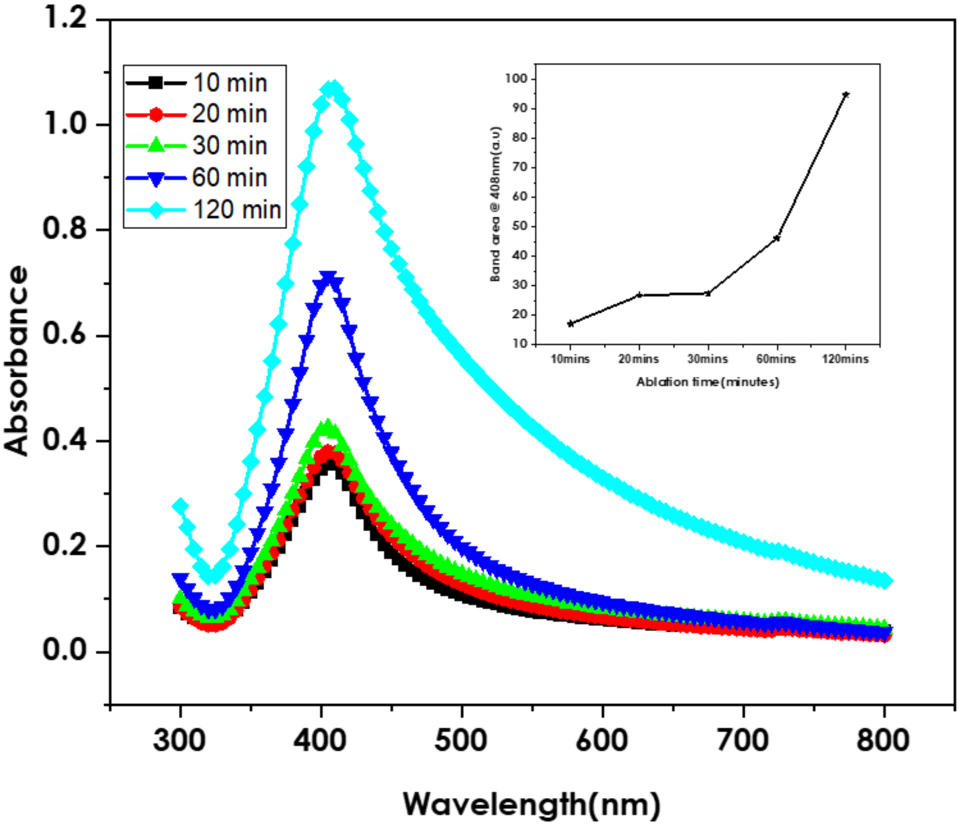

Figure 5-3:Absorbance spectrum of silver colloids for different ablation times by the same energy (200mJ) and pulse repetition frequency (5Hz).

The results in Figure 5-3 show that there is a direct correlation between absorbance and the time of ablation. According to Desarkar *et al.*, [9], a longer ablation time generates more nanoparticles as reflected in increased absorbance. The increase in absorption has also been associated with more particles agglomerating and as such, more energy getting absorbed. The figure shows that the absorbance band is at 400nm after which there is a tail part that is a result of the particle plasmon excitation and the also the interband transitions [10]. Amendola *et al.*, [11] also, explain that the band around 400nm shows that the generated nanoparticles are spherical.

5.1.2.4 Ablation Energy

Energy is an important parameter when exploring the synthesis of silver nanoparticles. Bola [12] reported that when the laser pulse energy increases, the generated nanoparticles also increase in size. A change in energy from 9 to 13mJ resulted in a change in size in the range of 9 to 22nm. From this research, it was observed that the peak absorbance of every sample had a linear relation with the concentration of the generated nanoparticles while the intensity of the yellow color characteristic of the silver nanoparticles changed based on the laser energy. Figure 5-4 shows the impact of laser energy on the absorbance of silver nanoparticles.

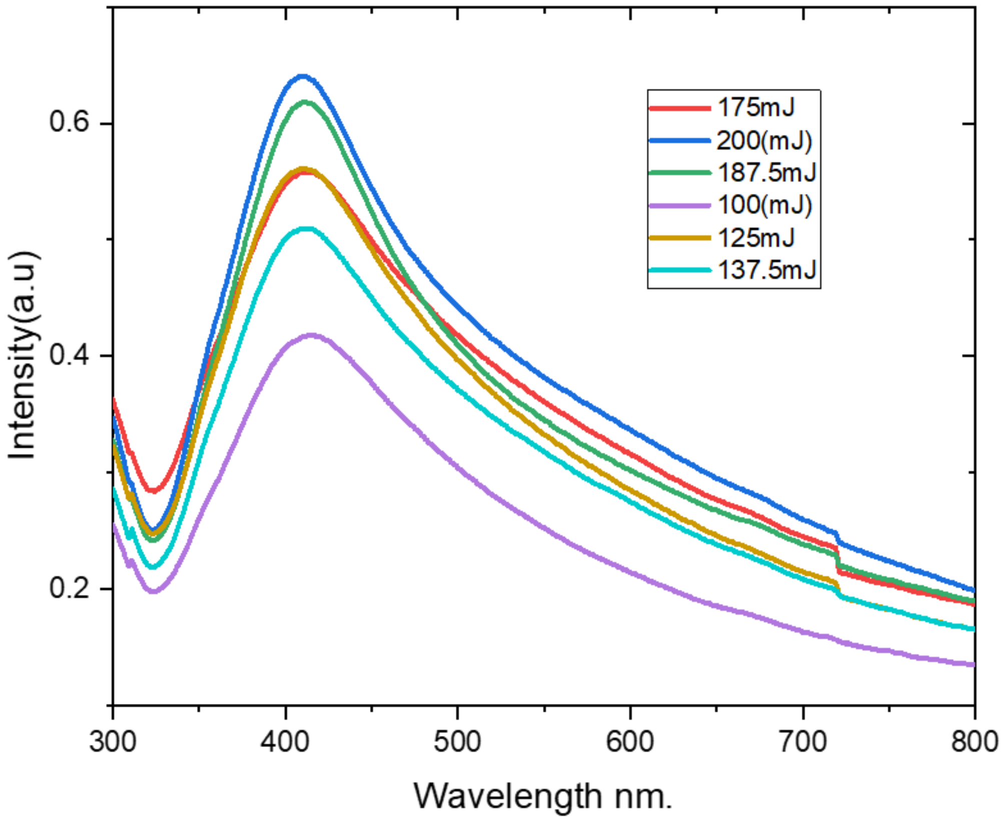

Figure 5-4:UV-Vis spectra of AgNPs at different ablation energies and 20-minute ablation time and 5Hz frequency.

As shown in Figure 5-4, the peak absorbance generally increases with an increase in the ablation energy but with all spectra consisting of strong absorption due to plasmon resonance around 400nm. As stated by Bola (2014) [12], the higher the peak absorbance the more the concentration of silver nanoparticles in the solution. Therefore, we can conclude from this observation that the higher the laser power, the more concentrated the nanoparticles tend to be in the solution. Although not noted in this research, Hernández-May *et al.*, [13] emphasized that the range between 100 – 180mJ can be regarded as an optimal range used for laser ablation and that it is not possible to generate nanoparticles with less than 100mJ energy or more than 180mJ. The research also noted that there is the possibility of saturation when synthesizing nanoparticles if the energy is above 180mJ.

5.1.2.5 Pulse Repetition Frequency

The laser pulse repetition rate had a notable impact on the development of the silver nanoparticles. Repetition rate is defined in this case as the number of laser pulses per second that hit the metal target. This study showed that there was a linear relationship between the concentration of silver nanoparticles and the pulse repetition rate in the lower ranges of 1,2 and 5 Hz as shown in Figure 5-5. Amendola & Meneghetti, [11] state the linear relationship is reported since the repetition rate is longer than the lifetime bubble cavitation time.

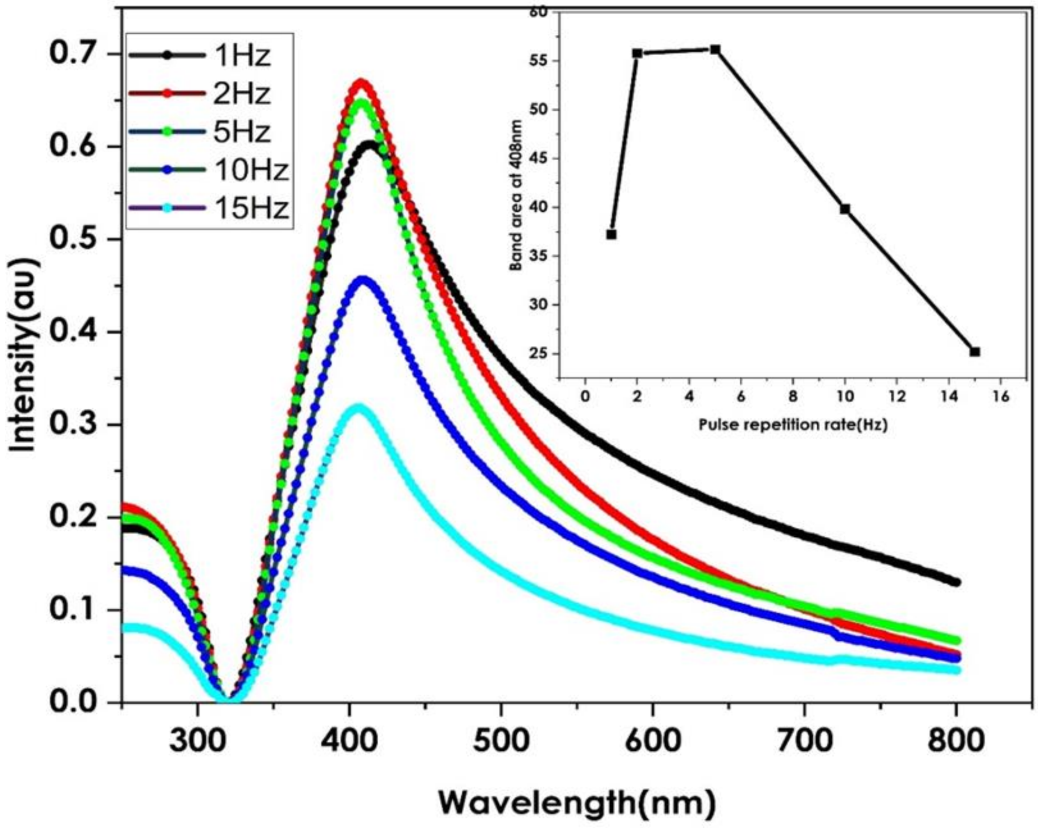

Figure 5-5:UV-Vis spectra of AgNPs at different repetition rates with time maintained at 1 hour and energy at 200mJ.

In this study, 5Hz was the threshold in the production of synthesized nanoparticles. Beyond this threshold, the concentration of silver nanoparticles reduced linearly as shown in the inset of Figure 5-5. Amendola & Meneghetti [11] note that beyond the threshold, the metal target temperature increases higher than the room temperature reaching an energy threshold for the detachment of the metal surface. A high pulse repetition also maintains the heat produced during ablation and also helps to reduce energy waste. Unfortunately, this only acts to speed up aggregation and the coalescing of the nanoparticles [14].

5.1.3 Raman Spectroscopy

Raman spectroscopy can characterize silver nanoparticles providing detailed information on their structural, chemical, and physical properties. Analyzing the Raman spectra of silver nanoparticles provides notable insights into their vibrational modes, surface chemistry, and interactions with surrounding molecules. This section provides a characteristic analysis of silver nanoparticles using Raman spectroscopy.

5.1.3.1 Laser Optimization

The synthesized nanoparticles were characterized using Raman spectroscopy; with 532nm and 785nm laser strengths to acquire the background SERS spectrum before interacting with the target analyte. An aliquot of the nanofluid was loaded on the surface of an aluminum foil which was covered with a slide and then let to dry in the ambient air. Figure 5-6 shows the Raman spectra of silver nanoparticles using the two laser powers.

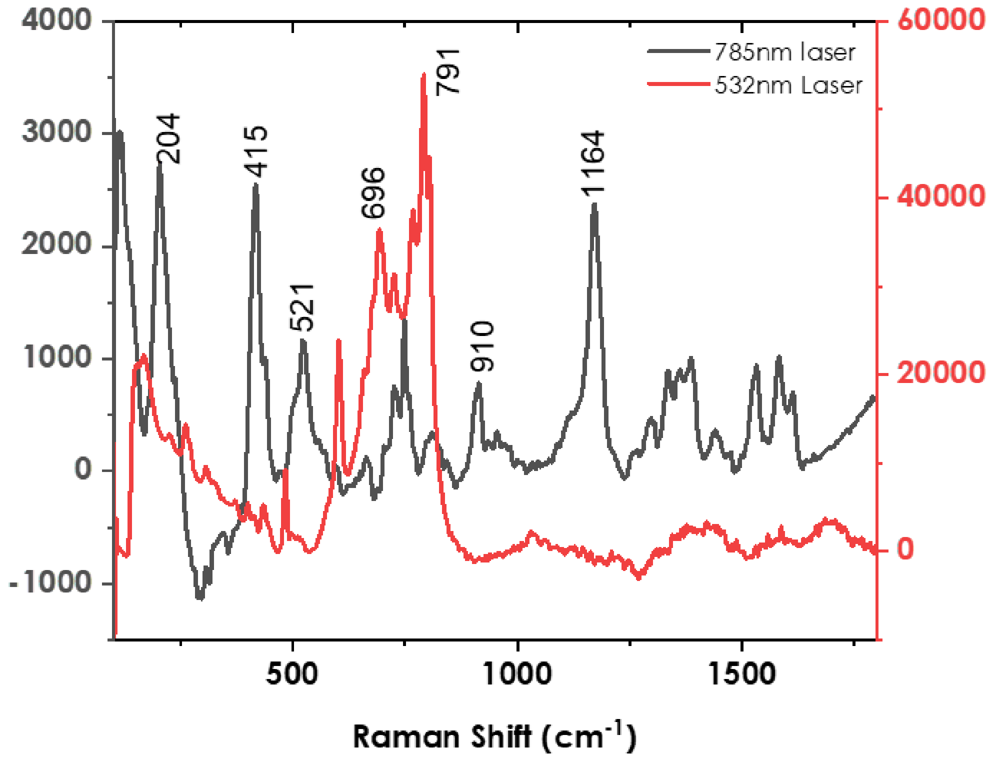

Figure 5-6: Raman spectra of silver nanoparticles using 532nm and 785nm laser strengths.

Some of the peaks that were observed were 204cm^{-1} for the 785nm laser which appeared at 199cm^{-1} when using the 532nm laser. An intense band at 415cm^{-1} was visible for the 785nm laser and almost invisible for the 532nm laser. The small band at 521cm^{-1} could be visible when using 785nm and shifted to 505cm^{-1} when using a 532nm laser. The peak at 791cm^{-1} was the most intense band when using a 532nm laser. This band was way low when using a 785nm laser. 910cm^{-1} and 1164cm^{-1} were only evident when using the 785nm laser while the bands at 1391cm^{-1} and 1578cm^{-1} were only sharper and more enhanced using the 785nm laser as compared to the 532nm laser.

The significant spectral variations of 785nm and 532nm laser when characterizing silver nanoparticles paint a better picture of subsequent SERS characterization. 785nm laser is more feasible for such characterization since it provides more spectral features and improved signal intensity. The prepared silver nanoparticles had a plasmon resonance band around 411nm (the green region). Since the 532nm laser is closer to this region, it benefits from the strong plasmonic effects that eventually result in significant enhancement of the signals in the UV region which is between 530cm^{-1} and 795cm^{-1}. Therefore, to properly characterize silver nanoparticles, a 785nm laser can be used since it reveals the peaks that are masked by the high fluorescence 532nm laser.

The lack of more spectral information within the medium frequency region of 1000cm^{-1} and 1800cm^{-1} when using 532nm laser suggests that subsequent characterization when the probe is adsorbed to the nanoparticles would be probably explained better using 532nm laser since any Raman scatter bands within this region would easily be attributed to the probe. This is unlike when using a 785nm laser where more silver nanoparticle bands would easily overlap with the signals from a probe that has Raman active modes within the same region.

5.1.3.2 Substrate Optimization

The interaction between the nanoparticles and the adsorbing surface is key in defining the Raman signal and in providing valuable information about the nanoparticles. For this work, three substrates were used as adsorbent surfaces in characterizing silver nanoparticles. As shown in Figure 5-7, the three substrates showed different signal enhancement behavior for a 532nm laser.

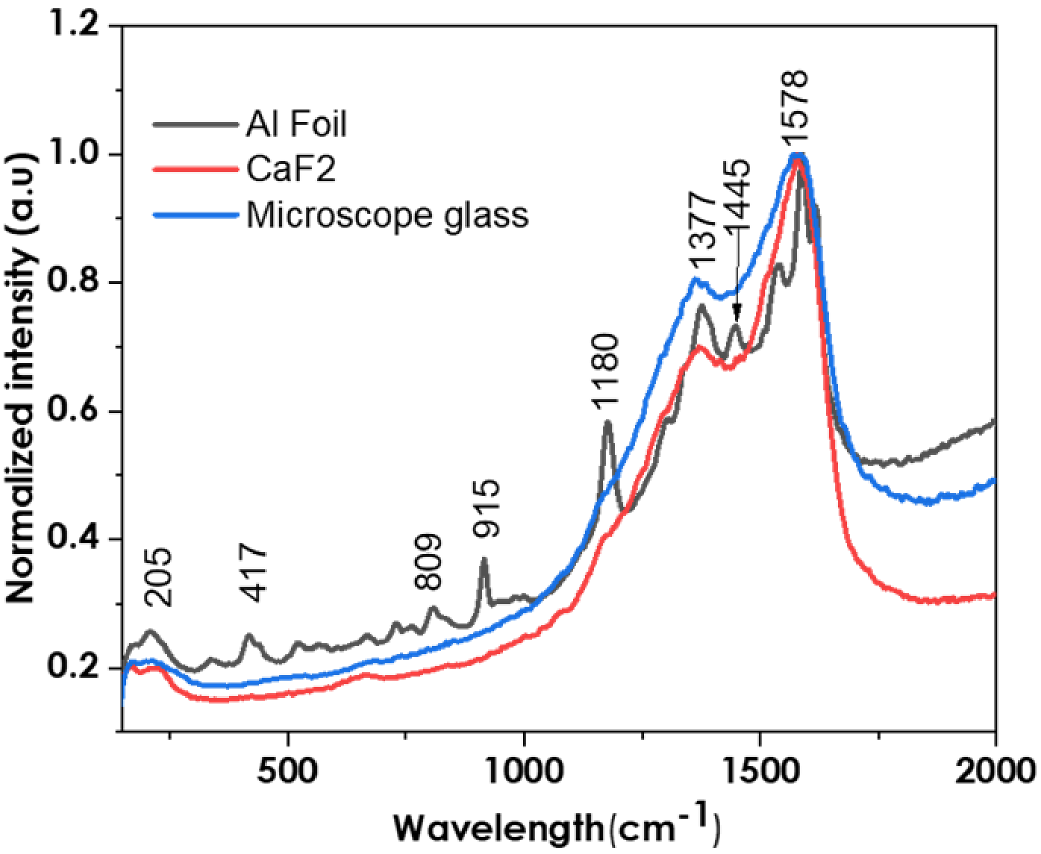

Figure 5-7: Characteristic Raman spectra of silver nanoparticles on Aluminium foil, calcium fluoride glass, and microscope glass, using a 532nm laser, 10 seconds exposure time, and 5 accumulations. The spectra have not been background subtracted to show the similarity.

Aluminum foil was the best substrate for characterizing silver nanoparticle signals. The spectra were obtained on the edge of the coffee ring after drying. The spectra that can be directly attributed to silver nanoparticles include 205cm^{-1}, 417cm^{-1}, 809cm^{-1}, 915cm^{-1}, 1180cm^{-1}, 1377cm^{-1}, 1445cm$^{-1,}$ and 1578cm^{-1}. All the bands can be assigned to silver colloids as noted by [15]. The spectra obtained were similar to what was reported by Joshi *et al.*, [16] who used a chemical synthesis method for preparing silver nanoparticles and assigned the bands as 233cm^{-1} (Ag-O stretching), 470cm^{-1}& 627cm^{-1} (stretching vibration of C-N-C), 1364cm^{-1} and 1544cm^{-1} for the carboxylic symmetric and the antisymmetric C=O stretching vibration. Calcium fluoride and microscope glass only provided peaks at 1377cm^{-1} and 1578cm^{-1} with no peaks in the lower frequencies. Lewis *et al*., [17] noted that calcium fluoride provides no means for increasing the rather weak Raman signals. The improved signals when using aluminum foil allow for improved Raman signal and obtaining more Raman features.

All the low-frequency vibrations could only be obtained using an aluminium foil substrate. Aluminium substrate's high reflectivity especially in the visible and near-infrared spectral range improves its utility when coupled to surface-enhanced Raman spectroscopy [18]. When a laser beam is directed onto the aluminum substrate, a significant portion of the incident light is reflected, ensuring efficient excitation of the sample [19]. The substrate also has low autofluorescence in the spectral range used for Raman spectroscopy, minimizing background noise and improving the signal-to-noise ratio of the Raman measurements. Gudun *et al*., [18] utilized the sensitivity and versatility of aluminium foil in making a SERS substrate for characterizing gold nanoparticles. Al foil is also known to yield a very low and featureless spectral background which is unlike glass that exhibits interference from the strong broadband that easily masks the important fingerprint bands at important spectral regions [19].

The conclusion that can be drawn from this finding is that aluminum foil can be used as an important substrate which can be complemented with the SERS tendency of silver nanoparticles to achieve an even higher signal enhancement behavior. When used as a substrate for Raman spectroscopy, aluminium facilitates the creation of SERS-active substrates providing plasmonic enhancements for the Raman signals.

5.1.4 Fourier Transform Infrared Spectroscopy

FTIR was used in conjunction with Raman spectroscopy to ascertain the nanoparticle's chemical structural characteristics as indicated in the spectra of silver nanoparticles in Figure 5-8.

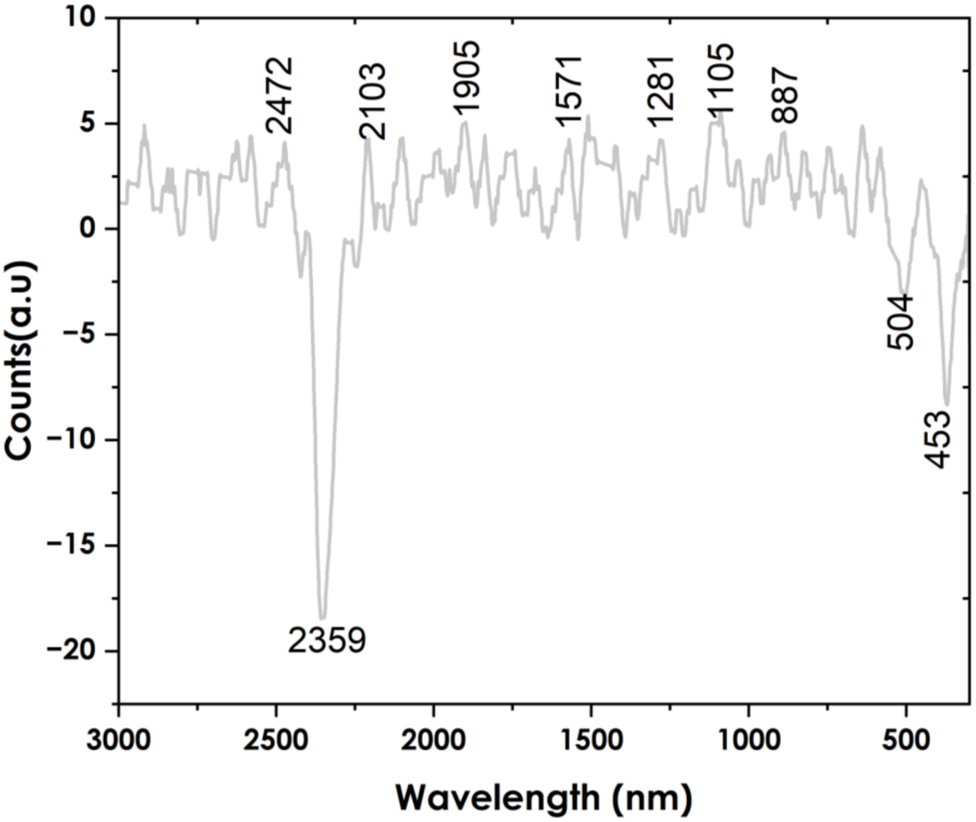

Figure 5-8: FTIR Spectra of Silver Nanoparticles.

The results show that FTIR exhibits prominent peaks at 2359cm^{-1}, 1571cm^{-1}, 1905cm^{-1}, and 2103cm^{-1}. Other minor peaks were noted to be at 1631cm^{-1} and 1383cm^{-1}. The bands have previously been reported by Marimuthu *et al.*, [20] who assigned the bands to the stretching vibration of the C=O group and C-C methoxy compounds stretching vibration.

5.1.5 Energy Dispersive X-Ray Spectroscopy

Energy dispersive X-ray spectroscopy was used as an effective analytical technique to provide chemical elemental information. In this research, the EDX was coupled to SEM and helped to provide the elemental composition of the silver nanoparticles. The EDS analysis was employed on the nanoparticles with Figure 5-9 showing an example of the EDS spectra on the synthesized nanoparticles.

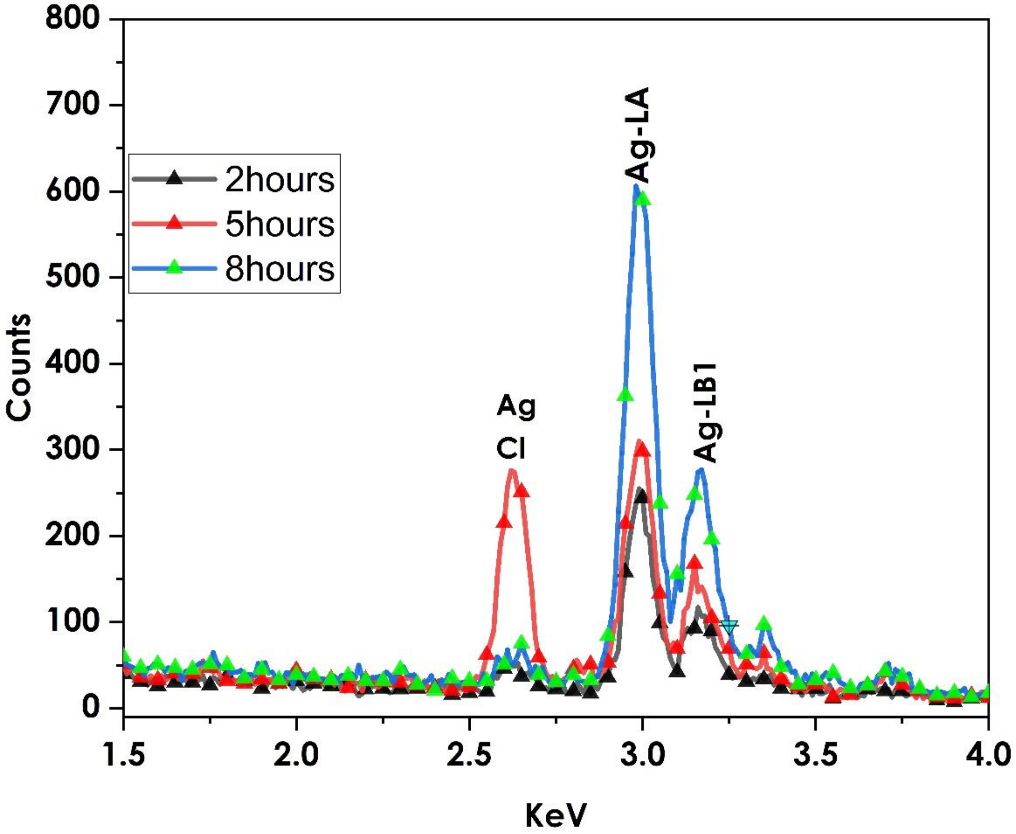

Figure 5-9:EDS spectra of silver NPs optimized at different ablation times.

In the EDS spectra, strong signals could be observed from the silver atoms in the nanoparticles at around 3keV which is characteristic of metallic silver nanoparticles. These results were in line with those reported previously by [21]. As shown in Figure 5-9, there is a linear relation between the intensity of the characteristic silver peak and the time of ablation used to synthesize silver nanoparticles. This linear relationship shows that the concentration of silver nanoparticles increases with the increase in ablation time and demonstrates the sensitivity of EDS in characterizing different concentrations of silver nanoparticles.

5.1.6 Energy Dispersive X-ray Fluorescence

EDXRF spectroscopy was employed in this work as an analytical method used to prove the existence of silver nanoparticles and then quantify them by measuring the spectral energy and intensity. X-ray fluorescence is based on the principle of interaction of radiations with matter causing either photoelectric absorption or scattering of the photons. Maaza *et al.*, (2018)[22] contend that the XRF technique is of great value in evaluating nanoparticles due to its versatility and ability to provide multiple analyses almost simultaneously. Besides, it ensures that the elements can be quantified without any damage to the sample. This work used an energy-dispersive X-ray fluorescence spectrometer Shimadzu series EDX800HS, model CE (212-23701-36), for spectral data measurements. The EDXRF spectrum of the synthesized nanoparticles is shown in Figure 5-10.

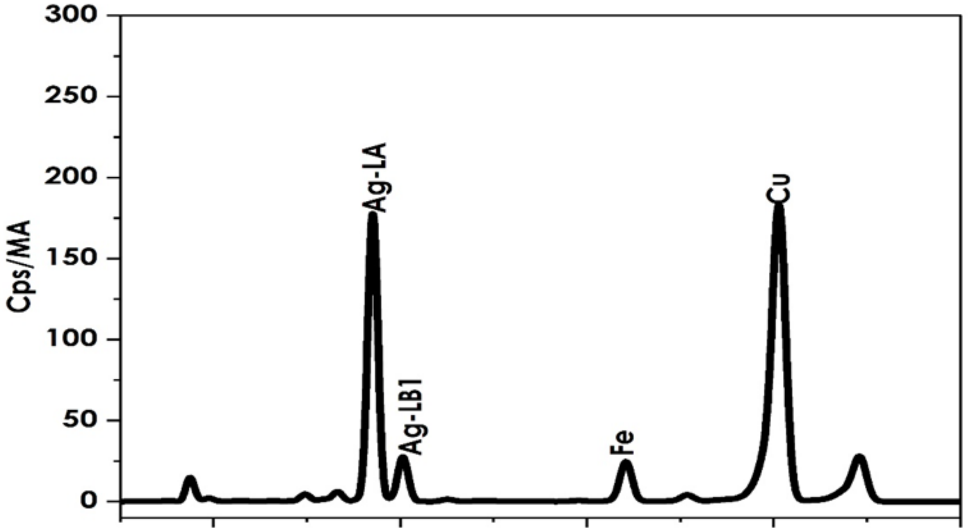

Figure 5-10: EDXRF Spectra of synthesized silver nanoparticles indicating the peak position of silver.

Using the X-ray fluorescence analysis, it was observed that the two forms of silver; Ag-Lα and Ag-Lβ are both evident. The two scatter bands have previously been reported by Fierascu *et al.*, [23] who reported a small shift in the bands due to the difference in the method used to synthesize the nanoparticles. This line is produced when an electron from the M shell transitions to fill a vacancy in the L shell while the Ag-Lβ line results from an electron transitioning from the N shell to fill a vacancy in the L shell. Therefore, based on the XRF spectra, we can confirm the presence of silver nanoparticles in the prepared nanofluid.

5.1.7 Laser-Induced Breakdown Spectroscopy

Silver nanoparticles were further characterized using laser-induced breakdown spectroscopy to help explore whether the generated silver ions were Ag^{2+} or Ag^{+}. The charge type/state is important in determining how the nanoparticle will interact with the target analyte as well as the stabilization mechanism of silver nanoparticles. Similarly, the HOMO-LUMO gaps of silver and analyte composites are significantly influenced by the charge state. Modeling the type of charge of the silver nanoparticles influences the interaction of silver nanoparticles and the target analyte. Emission lines showed the presence of both Ag^{+} and Ag^{2+}. Figure 5-11 shows the emission spectra of silver nanoparticles with an emphasis on the charge of silver ions.

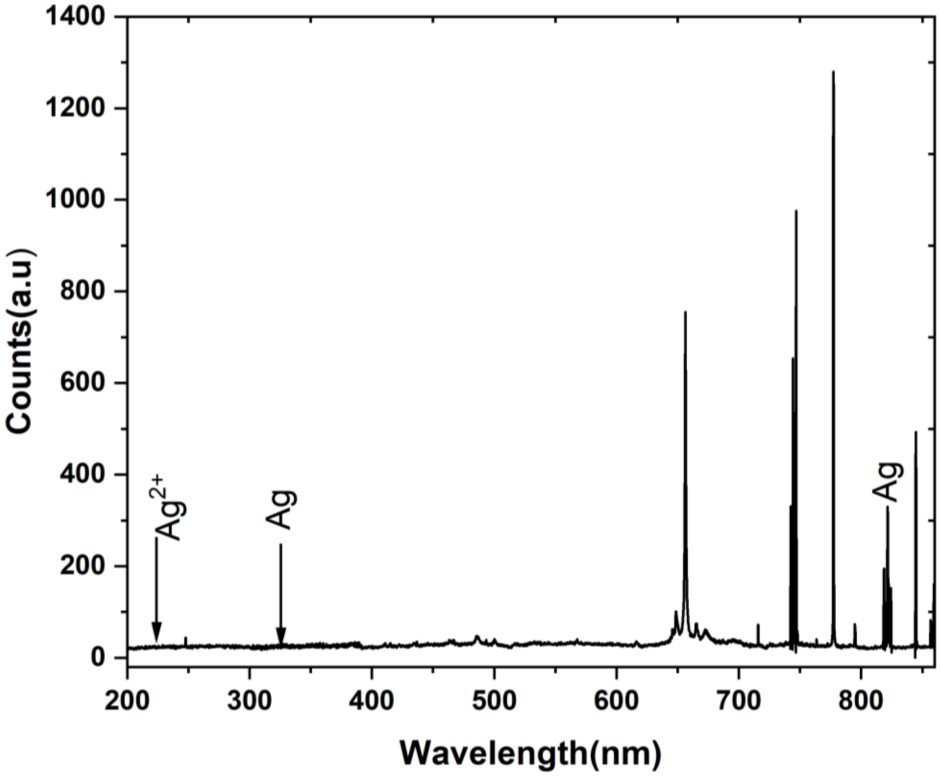

Figure 5-11: LIBS spectra for silver nanoparticles showing Ag emission lines.

Figure 5-11 implies that the analyte will adsorb with silver nanoparticles either through its Ag^+ or the Ag^{2+} to form a complex that changes the refractive index of the emerging environment. The charge also dictates how trenbolone acetate will adsorb on the silver slab which affects the efficiency of surface-enhanced Raman spectroscopy. In SERS, the enhancement of Raman signals is significantly influenced by the charge transfer interactions between the analyte and the silver substrate. Therefore, understanding the charge helps in predicting how effectively an analyte will bind to silver nanoparticles or other silver surfaces [24].

5.1.8 Scanning Electron Microscopy (SEM)

Scanning electron microscopy (SEM); MIRA3 TESCAN with 5 kV and a high-pressure vacuum was used to study the morphology of the synthesized nanoparticles. The SEM was coupled to EDX 300 ISI from the Oxford instruments with a Si detector. The samples were prepared by dropping 6 µl of the aliquot on a carbon grid and letting it dry under a fluorescent lamp. After drying the sample, it is only the nanoparticles that remain on top of the carbon thin film. The nanoparticles were observed at different ablation times and their morphology is shown in Figure 5-12.

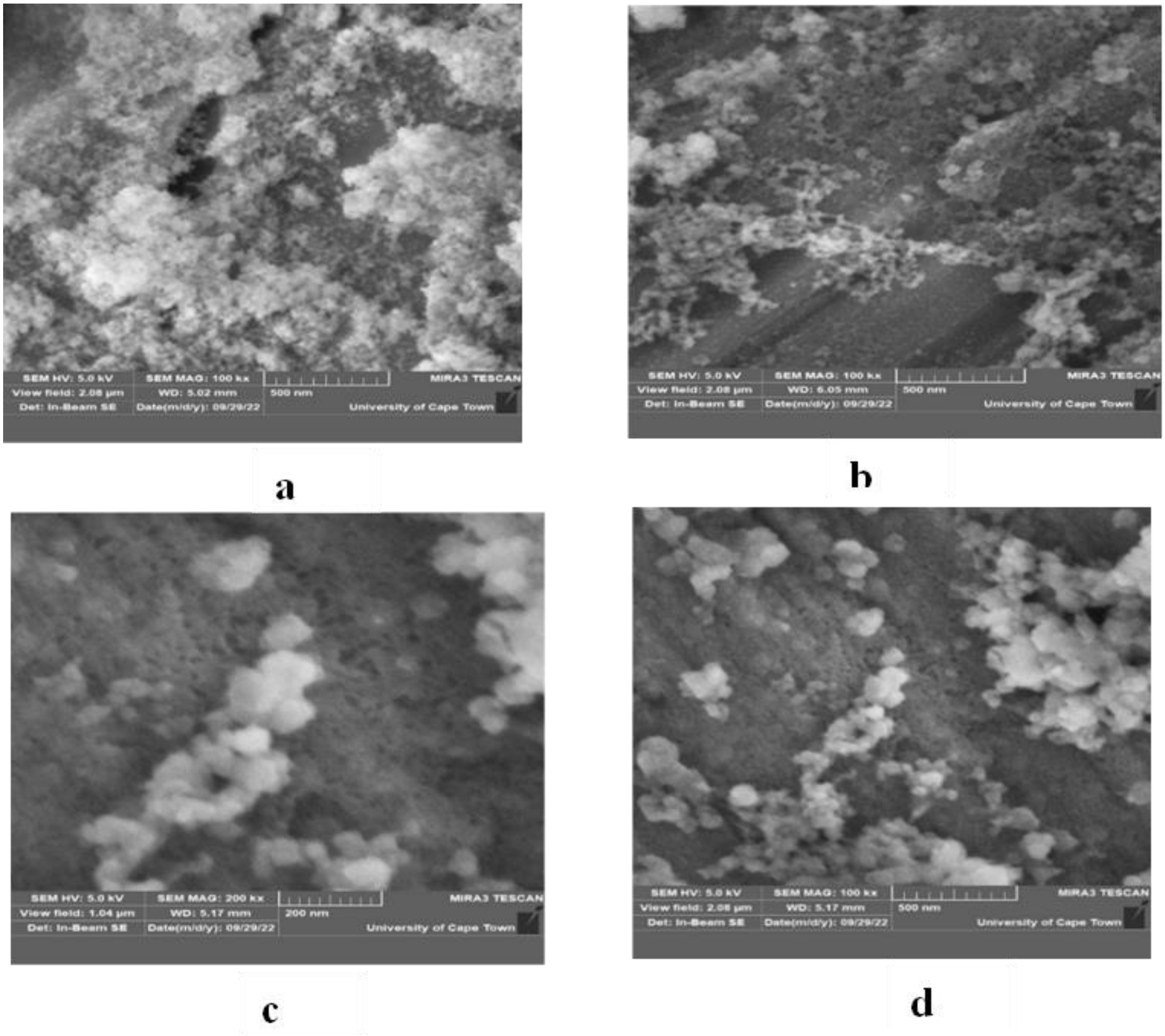

Figure 5-12: SEM image of synthesized Nanoparticles; 10a, at 2 hours laser ablation, 10b at 5 hours laser ablation and 10 c and 10 d are for 8 hours laser ablation; X200 and X100 magnification respectively.

As can be seen in Figure 5-12, several particles were agglomerated as is expected for colloidal particles in solution. The agglomeration increases with particle concentration. The size of silver nanoparticles recorded using SEM was estimated using ImageJ software. Another observation made is that the nanoparticles are spherical.

5.1.9 Transmission Electron Microscopy (TEM)

The TEM analysis was done using the Tecnai Osiris instrument from FEI Company which is optimized for its high speed and high-speed EDX measurements in the STEM mode. The instrument is equipped with four detectors that are integrated into the pole piece hence allowing detection of up to 200,000 X-ray counters over a 0.9 srad solid angle. The instrument is also equipped with an 11 Mpx Gatan Orius CCD microscope camera allowing both conventional bright field and dark field as well as high-resolution TEM imaging. TEM was employed for silver nanoparticles synthesized under different ablation times to explore the influence it has on particle sizes.

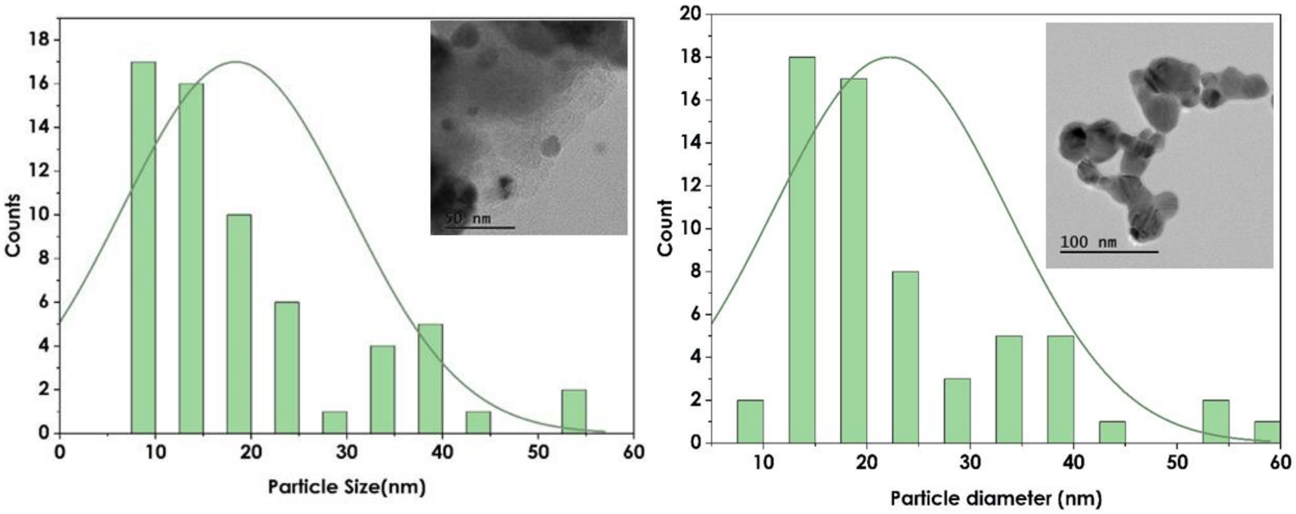

Figure 5-13: Histograms showing particle sizes from TEM analysis (inset: TEM images) for silver nanoparticles ablated at 8 hours (left) and 4 hours (right) with particle sizes 11nm and 16nm respectively.

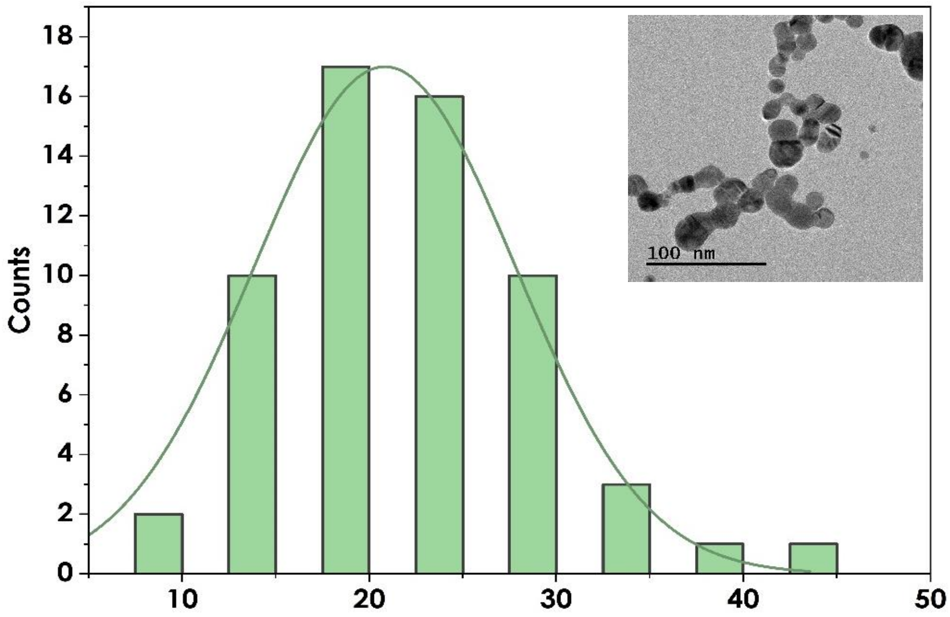

Figure 5-14: Histogram showing the size of silver nanoparticles ablated at 2 hours; average particle size is 21nm

Figure 5-13 and Figure 5-14 show that the particle sizes reduce with an increase in ablation time with the ablation at 8 hours showing the smallest particle size. Similar results were reported by Baruah *et al*., [25] who noted that the extended ablation duration increases the number of laser pulses hitting the target resulting in the generation of a higher quantity of nanoparticles. An even higher ablation time causes the nanoparticles to reach a point where they impede the laser beam penetration to the target. Therefore, the laser energy is absorbed by the nanoparticles that are already formed causing them to heat. The increase in temperature causes the particles to melt and fragment leading to the formation of smaller particles. The results demonstrate that for applications that require nanoparticles less than 10nm, longer ablation times will be used during the synthesis process. A summary of the impact of laser ablation time on the absorbance of localized surface plasmon band and the particle size is given in Figure 5-15.

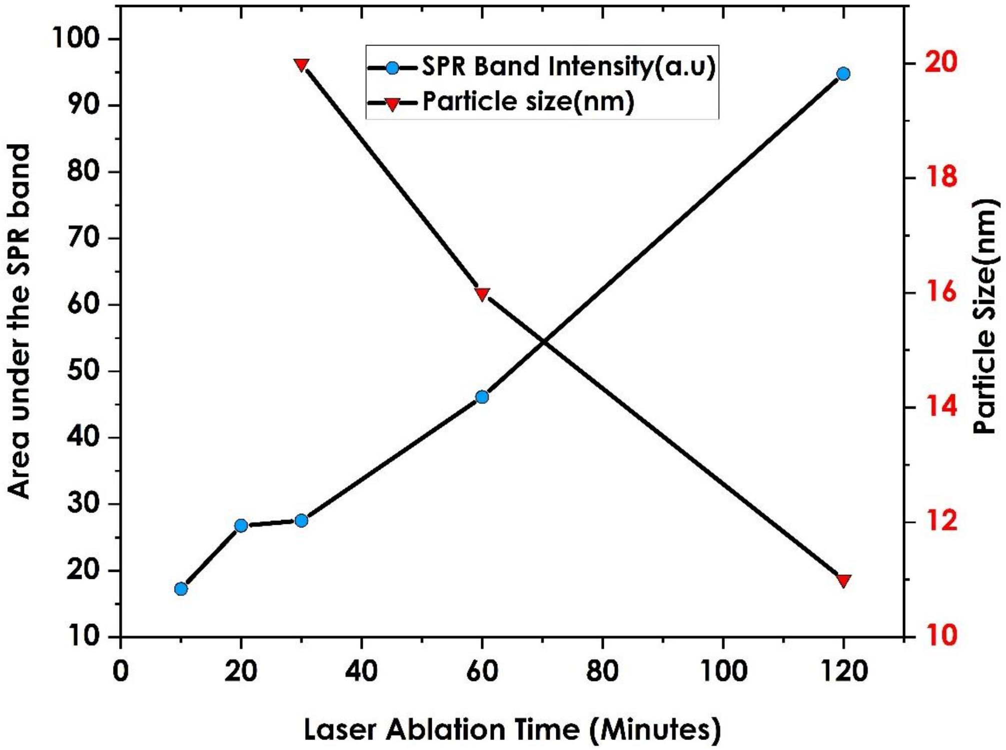

Figure 5-15: Impact of ablation time on particle size and the absorbance of the plasmon band of silver nanofluid.

As shown in Figure 5-15, the size of generated silver nanoparticles inversely relates to the ablation time. Conversely, an increase in ablation time during laser ablation of silver in liquid leads to an increase in the absorbance of the surface plasmon resonance (SPR) band of the resulting silver nanoparticles probably due to more nanoparticles being generated.

5.1.10 Conclusion

This section has provided an in-depth characterization of silver nanoparticles. The work has shown that laser ablation in the liquid approach is a reliable method for synthesizing nanoparticles of different sizes. The results show that it is possible to make particles of different sizes by varying ablation parameters like the ablation time and repetition frequency. The average particle size obtained using laser ablation was 24nm. Particle size affects the interaction between particles and analytes in biosensing applications. The size of particles can determine how effectively they bind to target molecules, impacting the accuracy and reliability of detection. The smaller particles obtained in this work exhibit a higher surface area to volume ratio which improves the particle's sensitivity in detecting trenbolone acetate. The sensitivity of the smaller nanoparticles was particularly important in detecting trenbolone acetate at lower concentration levels. Another important observation noted in the characterization is the lower aggregation of nanoparticles as shown using both SEM and TEM. The non-aggregation is important since it explains the improved binding nature of the nanoparticles with the target analyte. Therefore, objectives one and two were achieved with spherical silver nanoparticles being synthesized using laser ablation and optical characterization was effectively carried out to explore the nature of the generated nanoparticles.

5.2 Localized Surface Plasmon Resonance in Detecting Trenbolone Acetate

Localized surface plasmon resonance is a renowned approach that can be used in bio-detection even at low concentrations. The techniques offer a sensitive and label-free way of detecting minor changes in a molecule. Traditional LSPR-based biosensing uses the sensitivity of plasmon frequency to changes in the local refraction index at the nanoparticle surface [26]. This section explores results that were obtained by assessing the changes in the plasmon band due to the interaction of silver nanoparticles with trenbolone acetate.

5.2.1 Investigating the Beer-Lambert Law

According to Beer-Lambert law, it is recognized that in situations where concentrations are low, the level of absorption correlates directly with the amount of solute present [27]. Consequently, in these low-concentration scenarios, an increase in the number of particles in a solution leads to a corresponding rise in absorbance values, as each particle absorbs a considerable amount of light. In this work, the Beer-Lambert law was investigated, with a focus on the concentration under which it no longer holds. With UV-VIS, the spectral range upon which the radiations are absorbed was explored and kept to be between 200nm and 800nm. Maximum absorption of radiations occurred at around 408nm for silver nanoparticles and 349nm for trenbolone acetate dopant. To ensure that the absorbance does occur, the spectral range was maintained between 310nm and 440nm for both nanoparticles and the target analyte. Figure 5-16 Shows the investigation of the law with a focus on the specific concentration under which the law is obeyed.

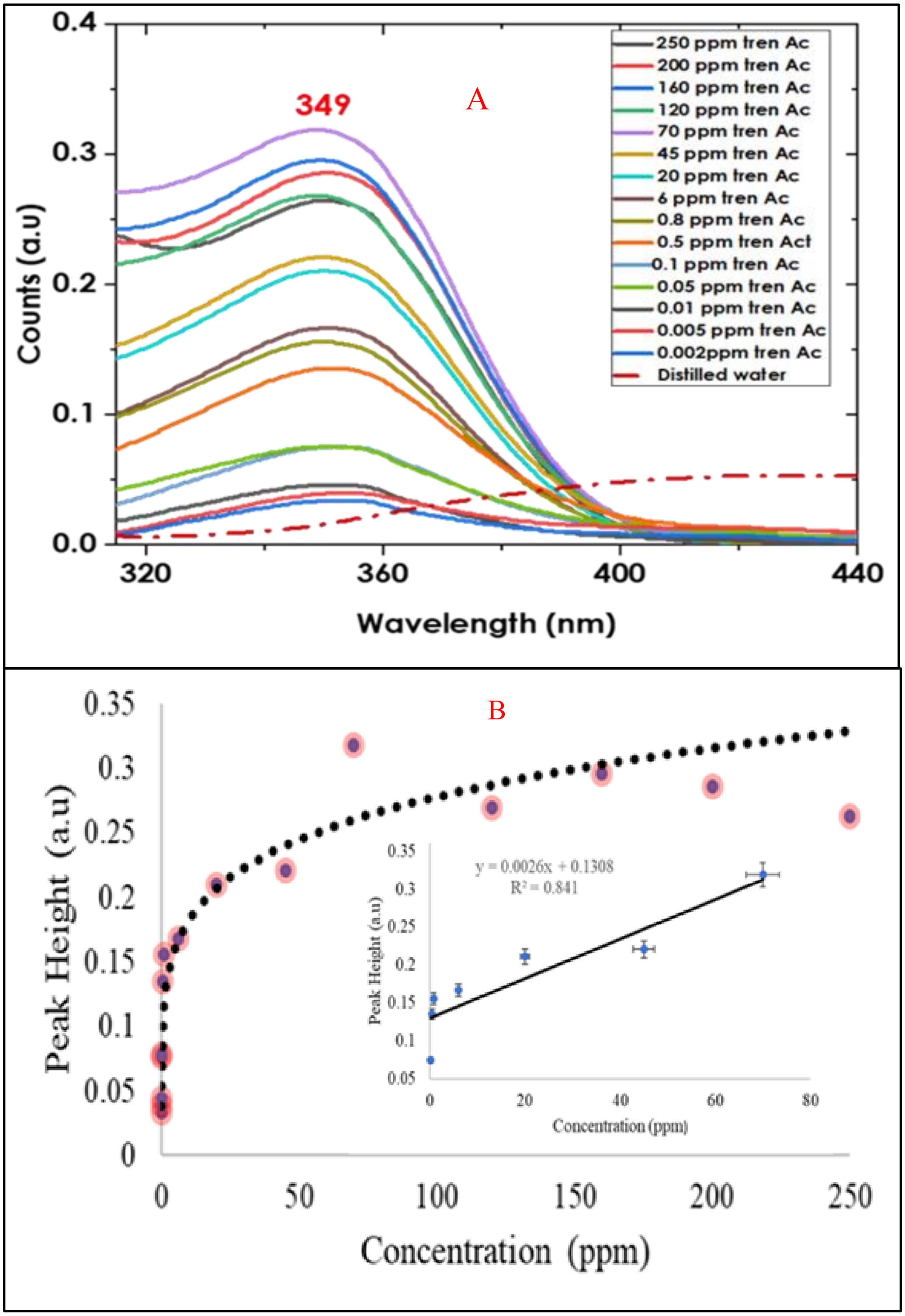

Figure 5-16:UV-VIS spectra of Trenbolone showing the absorbance band at 349nm (A) and the effect of concentration to signal intensity (B; the inset shows the calibration for concentrations between 0.1ppm to 70ppm) depicting the limit of Lambert-Beer Law.

A significant finding is the consistent increase in absorbance with the rise in trenbolone concentration up to 70 ppm. This outcome aligns with expectations, as spectroscopy attributes absorbance primarily to two factors: the concentration of absorbing substances and the distance light travels through the sample, as described by the Beer-Lambert law in Equation 5.2

$$A = \mathcal{E} * b * C \qquad 5.2$$

In equation 6-1, A is the amount of energy absorbed Ɛ is the molar extinction coefficient, b describes the thickness of the cuvette while C describes the concentration of the analyte. Equation 6-1 suggests that absorbance is likely to be higher at a higher concentration of the analyte since more particles will be absorbing the incident photons [28].

As indicated in Figure 5-16, the law seems not to hold after 70ppm which indicates that this has to be treated as the threshold concentration level. A primary factor contributing to the deviation from the linear trend, particularly beyond this threshold, is the increased coulombic interactions among molecules, leading to modifications in the electronic structure of the target analyte. At elevated concentrations, the likelihood of molecular interactions rises, consequently affecting the molar absorptivity coefficient crucial for absorbance determination.[29]. Furthermore, at higher concentrations, the increased presence of substances leads to greater light scattering and absorption within the material, causing additional distances for light to traverse. In mixtures containing multiple phases, such as the AgNPs and trenbolone acetate in this study, the refractive index changes due to changes in the dielectric environment. This heightened scattering at elevated concentrations explains the deviation from the Beer-Lambert law.

At the optimal concentration (70ppm), the incident photons may undergo self-quenching, resulting in decreased intensity in the absorption as well as a reduction in the activities of nanoparticles. The self-quenching tendency may lead to the formation of a core shell around silver nanoparticles which influences the sensing behavior. Moreover, the luminescent properties of trenbolone acetate result in the failure of the law, as fluorescent emissions get to the detector, causing the absorbance signal to die off, especially at higher concentrations [30]. In addition, reabsorption of the emitted radiation is assumed which suggests the failure of the law in such circumstances.

5.2.2 Detection Limit of Trenbolone Acetate Using Absorbance Measurements

To explore the experimental detection limits, UV-VIS was employed within a concentration range below 70ppm since that is the region where the Beer-Lambert law holds. The ranges are also considered since they are the detection limits for steroids and other performance-enhancement drugs as approved by the World Anti-doping Agency (WADA) as shown in Figure 5-17.

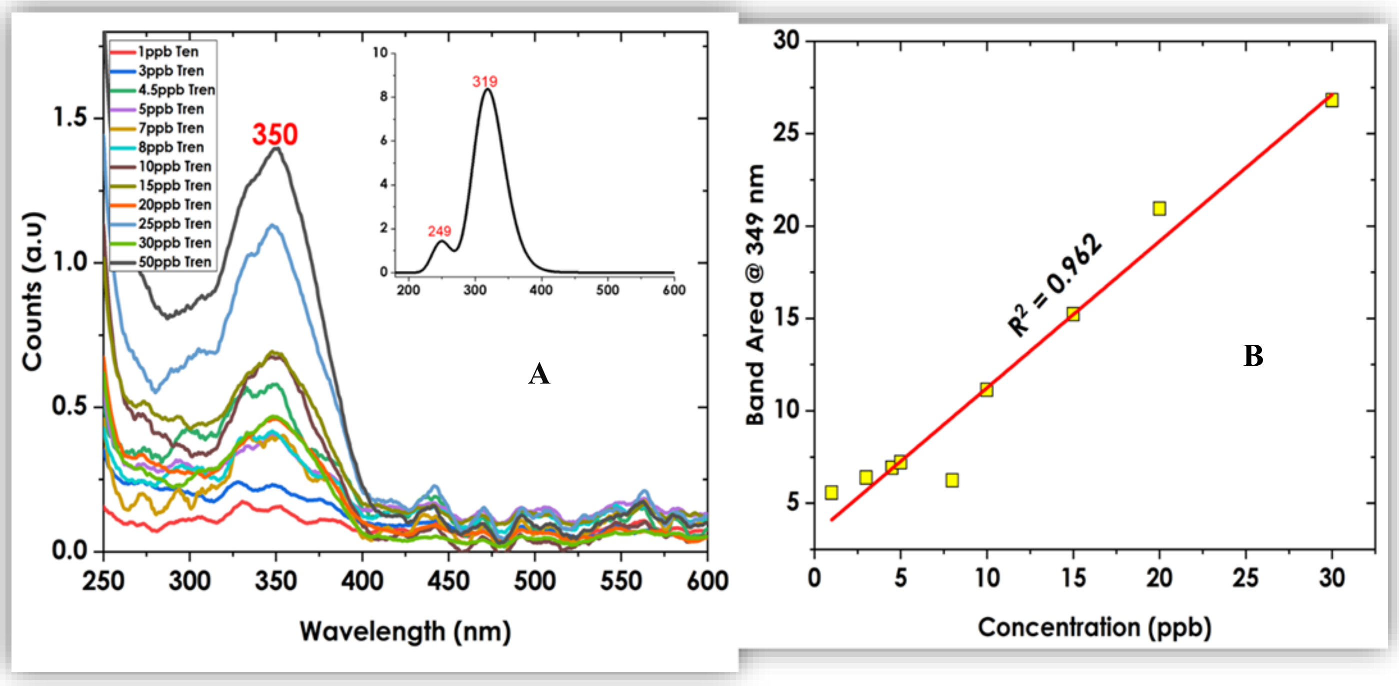

Figure 5-17:UV-VIS spectra of trenbolone for the biosensing region of interest (A) and on the calibration curve (B).

The analytical technique used to detect trenbolone and other anabolic steroids dictates the detection limit likely to be achieved. WADA has set the detection limit to be between 2 to 40ng/Ml. Therefore, the sensitivity of any analytical technique is measured by the ability to achieve this detection limit. A more sensitive analytical technique is likely to achieve a lower detection limit. For the absorbance measurements using UV-VIS, concentrations were measured using concentration ranges between 1 to 50 ppb which falls within the recommended WADA limits. As shown in Figure 5.17 (B), there is a linear correlation between intensity (given as the area under the band) and concentration of trenbolone acetate dopant. Using regression analysis, it is possible to explore the detection limit of UV-VIS based on the response of the plasmon band. Using the sensitivity curve, the limit of detection can be given as;

$$LOD = \frac{3\sigma}{S} \qquad 5.3$$

In equation 6.2, σ can be expressed as √n * standard error given on the y-intercept after plotting a regression line, n describes the number of variables while S is the slope. Based on equation 6.2, the LOD was **9.12ppb** which is within the limits set forth by the World Anti-doping Agency.

5.2.3 Optimizing AgNPs: Trenbolone Acetate Ratio

The mixing ratio of silver nanoparticles to trenbolone acetate has a notable influence on the plasmon behavior and in using localized surface plasmon resonance in bio-detection. Therefore, the optimal ratio at which the nanoparticles are mixed with the target analyte was explored since it was determined that varying the mixing volume had a significant impact on both the band position and the position of the LSPR band and the absorbance of the nanoparticles as shown in Figure 5-18.

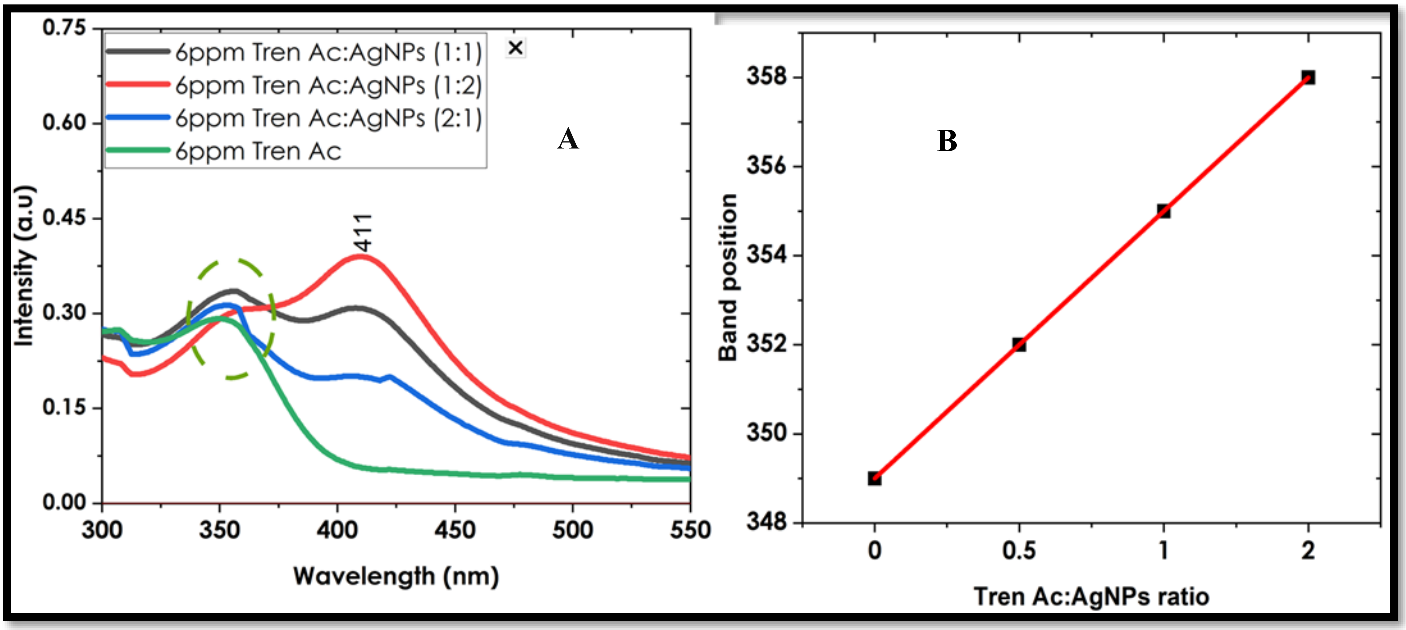

Figure 5-18:Ratio of Tren Ac to Silver nanoparticles (A) and the influence of AgNPs concentration on the Tren Ac band position (B).

Several observations can be made as indicated in Figure 5-18. One of the observations was that there was a notable red shift in the silver nanoparticle plasmon band with a slight change (red-shifting) in the absorbance. On the other hand, the results also show that there were more evident shifts when the volume of nanoparticles used increased (as shown in the spectra marked red in Figure 5-18A). The figure shows that doubling the volume of nanoparticles reduces the intensity of the absorbance band to nearly zero. On the contrary, the plasmon band of silver nanoparticles at 411nm increases significantly. Therefore, the intensity pattern specific to the trenbolone absorbance band contrasts with that of the LSPR of the nanoparticles. This outcome is anticipated because increasing the concentration of silver nanoparticles (by increasing the volume of nanoparticles) implies that more of them absorb light, thereby diminishing the presence of light absorbed by Trenbolone. Hajizadeh *et al*., [31] noted similar results when exploring the impact of cyanide on the localized surface plasmon resonance band using silver nanoparticles. The author observed that increasing the amount of cyanide while maintaining the volume of silver nanoparticles led to a reduced intensity in the surface plasmon resonance. Hajizadeh *et al* [31] asserted that mixing the ratio of silver nanoparticles to cyanide as 1:0.5 provided the desired signal enhancement. For this work, the ratio of silver nanoparticles to trenbolone was maintained at 1:1 to optimize their interaction and to obtain the best signal enhancement. This ratio was also the most optimal one in maintaining the desired signal specific to silver nanoparticles.

5.2.4 Impact of Trenbolone Acetate on the LSPR Band

The influence that a molecule has on the LSPR band after binding often forms the basis for biosensing applications. Binding nanoparticles with the analyte changes the dielectric environment and such changes can be monitored using optical techniques. This section explores some of the changes to the local environment after mixing trenbolone acetate and silver nanoparticles.

5.2.5 Change in the Intensity of the Plasmon Band

In this section, the concentration of trenbolone acetate was varied to explore the subsequent impact on the localized surface plasmon band. The change in the plasmon band in terms of intensity and shifts in the band position is assessed and presented in Figure 5-19.

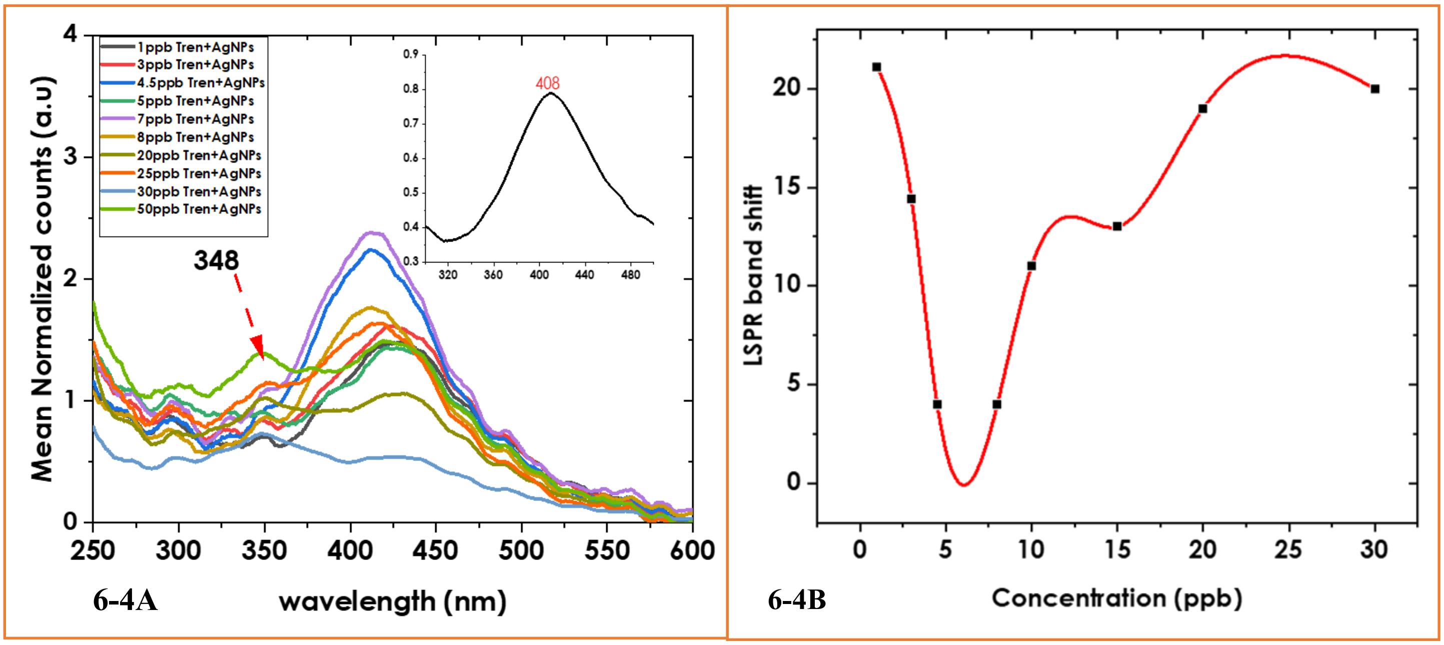

Figure 5-19: 5-19A; Influence of Varying Tren Ac Concentrations on the LSPR Position of AgNPs (inset: absorbance band of AgNPs) and the 5-19B is the LSPR shift

Notable insights were explored using UV-VIS spectroscopy after mixing trenbolone acetate with silver nanoparticles. For instance, mixing the nanoparticle with analytes led to a reduction in the intensity of the localized surface plasmon resonance band. The reduction can be attributed to the competition between absorption and scattering since within the wavelength range that is similar to that of the plasmon resonance of silver nanoparticles, the molecules of interest can either absorb or scatter the oncoming radiations. Therefore, the intensity reduces since not all radiations will be absorbed by the molecules. The other reason for the reduction in intensity is the fact that analytes get adsorbed on the silver nanoparticles creating a core shell-like structure that changes the optical characteristics, including altering the absorbance. Silver nanoparticles are known for their LSPR behaviors that explain their potent absorption and scattering capabilities, which account for their potent absorption and light scattering abilities, trenbolone acetate gets adsorbed on the nanoparticle surface, influencing the nearby electromagnetic field and consequently changing the LSPR characteristics. In label-free analysis, the intensity of the plasmon band can be monitored at different analyte concentrations to build a calibration strategy for quantitative purposes.

5.2.6 Red-shift in the LSPR Band

Besides the change in intensity, mixing silver nanoparticles with trenbolone acetate resulted in a shift in the localized surface plasmon band, an aspect that can be used in the sensing of trenbolone acetate. The shift in LSPR diminishes initially and then escalates exponentially as the concentration of the analyte increases as shown in Figure 5-19B. When the concentration of trenbolone acetate is low, the individual molecules easily interact/adsorb on the nanoparticle surface resulting in the possible coupling of the EM field. It is from the coupling that a wider LSPR band is reported occasioned by the fluctuations in the refractive index of the surrounding environment. The LSPR band not only looks wider but also less distinct. Upon binding, any slight changes in the electromagnetic field result in a wider change in the LSPR band position and intensity. Such sensitive changes form the hallmark of biosensing applications and confirm the Drude model that ascertains that the LSPR band linearly correlates with the refractive index of the surrounding environment [32]. According to the model, a shift in the plasmon band exponentially changes with the nanoparticle size.

5.2.7 Effect of Trenbolone Acetate on FWHM Band Broadening Behavior

Different ways can be used to assess how sensitive a biosensor is. Some of the ways include ascertaining the limit of detection (LOD), using the figure of merit (FOM), and the quality factor among other ways. The figure of merit holds particular significance since it can be explained based on sensitivity and the FWHM of the absorbance or the transmission. Similarly, the figure of merit given in Equation 5.4 can help to ascertain the signal-to-noise ratio of the obtained signal.

$$FOM = \frac{S}{FWHM} \qquad 5.4$$

In equation 6.3, S is sensitivity, FOM is figures of merit and FWHM is the full width at half maximum. To ensure that this work focuses on how silver nanoparticles can be used towards optical biosensing, the influence of changes in concentration of trenbolone acetate on the full width at half maximum of the absorbance band was explored. Figure 5-20 shows how the width of the LSPR band changes with the concentration of trenbolone acetate.

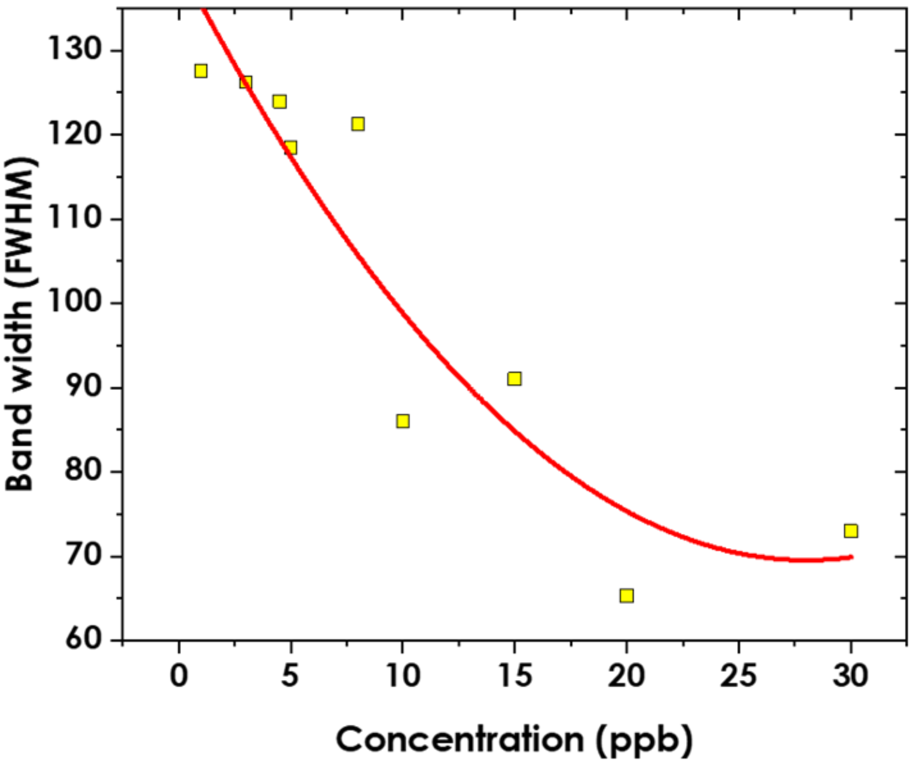

Figure 5-20: How LSPR bands contract with the increasing concentrations of the trenbolone acetate

From Figure 5-20, the band broadening tendency is evident, suggesting a possible interaction of Tren Ac and silver nanoparticles. The interaction resulted in a change in optical properties. For instance, the widening of LSPR can be explained by the reduced plasmonic interaction of tren Ac and silver nanoparticles. At low concentrations of trenbolone acetate, there is minimal electrical field interference due to the higher abundance of silver nanoparticles compared to trenbolone acetate. Consequently, at higher analyte concentrations, the interaction with the silver nanoparticles is greater resulting in the narrowing of the plasmon band.

Combining the nanoparticles with trenbolone acetate also leads to changes in electronic transitions used for the absorption of light. This interaction may result in changes in the full width at half maximum (FWHM) compared to bare nanoparticles. Another potential cause for band narrowing is heightened particle agglomeration with increasing trenbolone concentration, a phenomenon termed an ensemble effect.

5.2.8 Core-Shell Structure of Silver Nanoparticles

The agglomeration behavior of the Tren ac/silver nanoparticle complex was evaluated to help assess the core-shell structure of silver nanoparticles. Energy dispersive X-ray spectroscopy (EDS) was carried out to explore the concentration of elements for silver nanoparticles and for silver nanoparticle/trenbolone acetate complex.

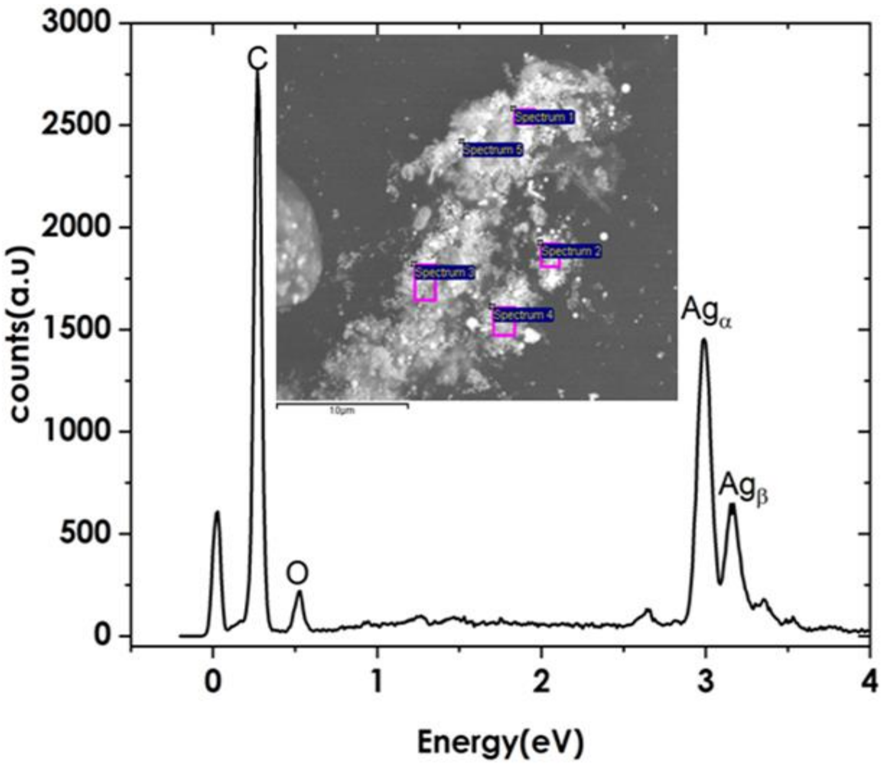

Element	Atomic Weight
Carbon	37.81
Oxygen	12.11
Silver	50.08
Total	100

Figure 5-21: The EDS Spectra of AgNPs with atomic weight percentage concentration of Atoms

Using EDS, it was possible to identify peaks attributed to silver at 3 eV and 3.2eV and those attributable to Oxygen as shown in Figure 5-21. However, the reported carbon is due to the carbon tape that was used as the substrate on which the sample was placed for analysis. The results show that silver was the most abundant element with a 50.08% concentration level. However, on mixing silver nanoparticles with trenbolone acetate, the percentage concentration of silver and oxygen changes as shown in Figure 5-22.

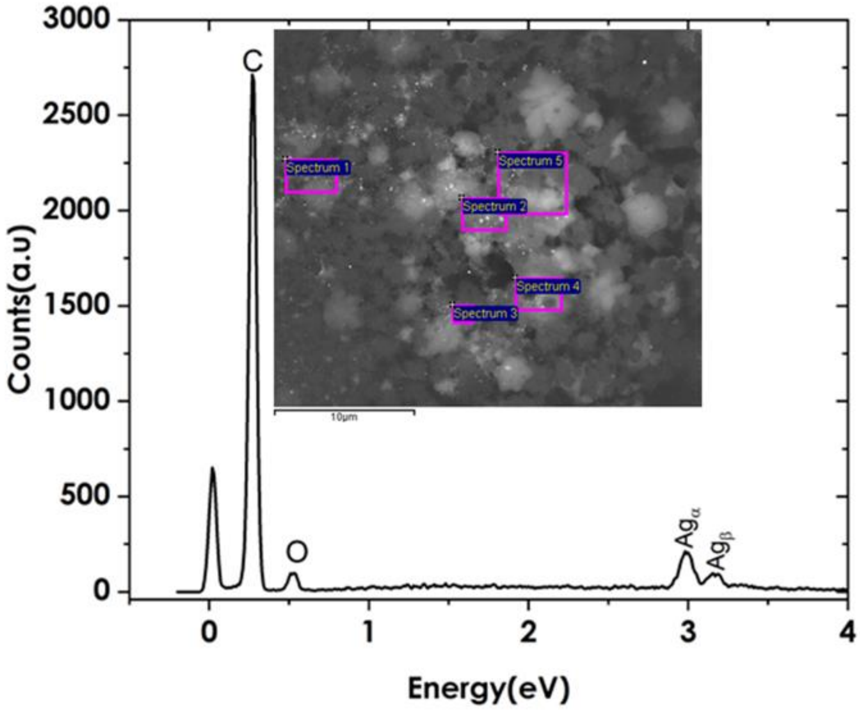

Element	Atomic Weight
Carbon	37.66
Oxygen	43.19
Silver	19.15
Total	100

Figure 5-22; The EDS Spectra of Tren Ac Adsorbed on AgNPs with the atomic weight percentage concentrations

As shown in Figure 5-22, there was a significant reduction in the concentration of silver after mixing the nanoparticles with trenbolone acetate. The EDS results show a reduction in the concentration of silver nanoparticles from 50.01% to 19.4%, while the percentage concentration of Oxygen increased from 12.11% to 43.19%. These percentages represent averages derived from five spectra collected at distinct points, as illustrated in the accompanying inset graphs. A reduced concentration of silver implies that post-mixing shows that a substantial portion of the nanoparticles became impeded by incoming radiation. This alteration indicates the formation of a core-shell structure wherein trenbolone acetate atoms encapsulate the silver nanoparticles. Consequently, incoming radiation predominantly interacts with the surface of the analyte, with fewer radiations penetrating through to the silver atoms. The presence of oxygen, which increased in concentration, further supports the core-shell hypothesis. Trenbolone acetate comprises carbon, oxygen, and hydrogen, with hydrogen being undetectable via EDS due to its low atomic number. Given the rise in oxygen concentration from 12.11% to 43.19%, it can be inferred that the majority of excited oxygen atoms originated from the analyte since those from the nanoparticles were enveloped by the analyte atoms after adsorption. Thus, the discernible conclusion is that trenbolone acetate molecules aggregate on the surface of Ag NPs, assuming a core-shell-like configuration [33].

5.2.9 Conclusion

Localized surface plasmon resonance (LSPR) was a key aspect in understanding the plasmon behavior of silver nanoparticles and how it can be used in label-free detection of trenbolone acetate. The main aim of this section was to explore the optical properties of trenbolone acetate and Tren Ac/silver nanoparticles complex. In assessing LSPR in bio detection of trenbolone acetate, some of the optical properties that were explored include changes in the localized surface plasmon band of silver nanoparticles, changes in the band width and band intensity as well as the core-shell behavior of silver nanoparticles and how it influences detection of trenbolone acetate. The results in this section showed that the dielectric environment changes after mixing the nanoparticles with the analyte. The changes were sensitive to any slight concentration changes demonstrating the ability of LSPR to achieve sensitive analyte detection capabilities. UV-VIS also demonstrated to be an effective optical technique in ascertaining the optical properties of silver nanoparticles through its plasmon band. Our paper published in Nature scientific https://www.nature.com/articles/s41598-024-56456-w already demonstrated the feasibility of using localized surface plasmon resonance in detecting trenbolone acetate and the results could be extended to other androgenic anabolic steroids and other biosensing applications. Therefore, based on the results and subsequent publication, it can be concluded that objective three of the work has been achieved.

5.3 Silver Nanoparticles as Substrates Used in Surface-Enhanced Raman Spectroscopy

For this part of the study, different concentrations of trenbolone acetate were mixed with silver nanoparticles which acted as substrates. The volume of the nanoparticles to that of the analyte was 1:1. Thereafter, an aliquot of the mixture was micro-pipetted and dropped on aluminum foil which is a hydrophobic surface that concentrates the target sample. The sample was characterized both in liquid form and when dried on the surface as is the case for drop coating deposition Raman.

5.3.1 Raman Spectra of Trenbolone Acetate and Tren Ac/AgNPs Complex

The Raman spectra of unaided trenbolone acetate were different from those of trenbolone acetate when mixed with silver nanoparticles. This section explores the ability of Raman spectroscopy to characterize and monitor the spectral changes of trenbolone acetate when mixed with silver nanoparticles.

5.3.1.1 Raman Spectra of Trenbolone Acetate

Trenbolone acetate (Tren Ac) has a benzene ring which is made of six carbons with alternating double bonds. The characteristic Raman scatter bands of the molecule are shown in Figure 5-23. The Raman spectra of trenbolone acetate were collected in the liquid phase without any further pre-treatment.

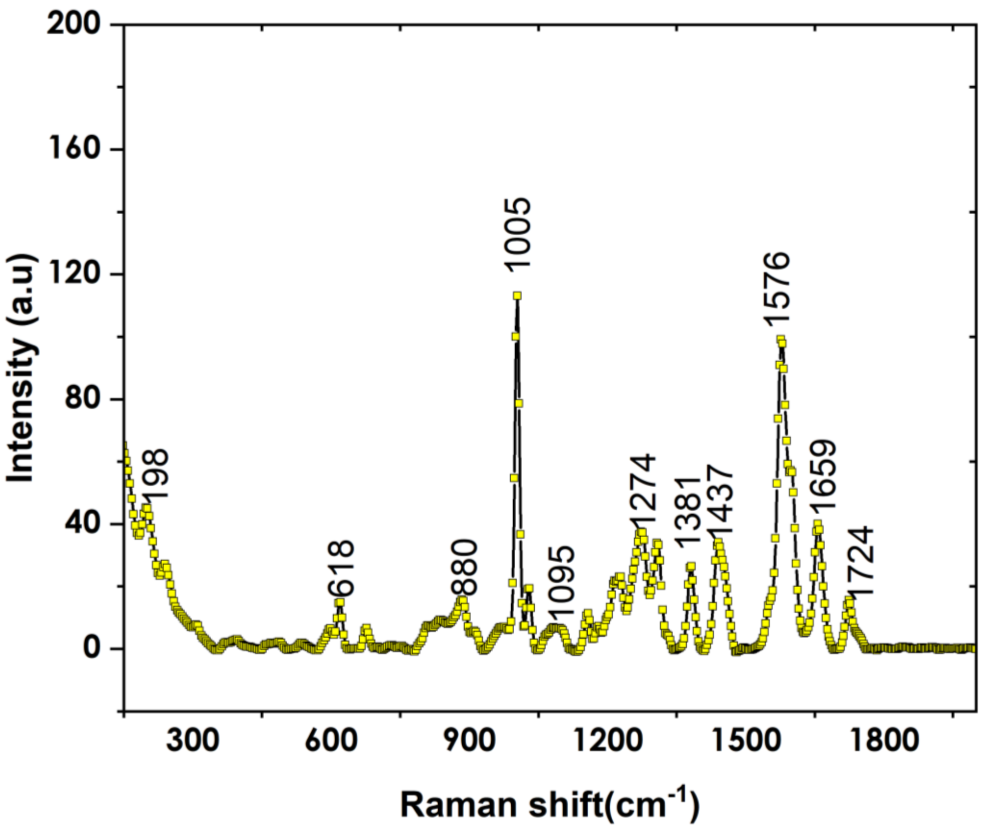

Figure 5-23: Raman spectrum of trenbolone acetate.

The most active Raman vibrational bands were observed between 900cm^{-1} and 1750cm^{-1}. The spectral assignments of the bands can be summarized as follows;

C=O Stretching

The carbonyl (C=O) group of the acetate ion provides symmetric vibrations at 1576, 1659, and 1724 cm^{-1}. The 1659 and 1724cm^{-1} vibrational modes have the highest percentage contribution at 80% and 86% respectively as will be shown while discussing potential energy distribution (PED).

Deformation vibrations

Bending normal modes are found between 1095 and 1647cm^{-1}, including the δ(HCH), δ(HCC) (methine group), and δ(HCO). Trenbolone acetate is also made of three cyclohexane and one cyclopentane ring which provide the steroid nature of the molecule. Therefore, δ(CCC) and δ(COC) bending modes were evident. The bending mode configurations are assigned at 372 and 351cm^{-1} for OCC and CCO respectively. The δ(CCC) is assigned in low-frequency vibrations between 212 and 963cm^{-1}. The rocking motion of the methyl group which is also common in an acetate molecule is evident at the δ (CCC) with a band positioned at 793cm^{-1}.

C-C and C-O stretching Vibrations

The acetate part (CH3COO-) of the molecule is also defined by the C-O stretching vibration that is observed between 900 and 1300cm^{-1}. There are dominant bands at 924, 1013, and 1269cm^{-1} all of which can be assigned to the C-C and C-O stretching vibrations.

Torsional Vibrations

Different types of torsional vibrations are also evident in trenbolone acetate molecules. The vibrations can be assigned as low-frequency and medium-frequency vibrations. The medium frequency torsional vibrations include τ (HCCC) at 1000/1380/1293/1424 and 1320cm^{-1}. The other medium frequency torsional vibration is τ (HCOC) at 1329, 1062, and 1468cm^{-1}. Other than 1329 and 1468cm-1, the rest provide asymmetric contributions. Low-frequency torsional vibrations are assigned in frequencies less than 400cm^{-1} and assigned to CCCC and HCCO bands.

5.3.2 Surface Enhanced Raman Spectra of Trenbolone Acetate

In this section, the Raman spectra (RS) and surface-enhanced Raman spectra (SERS) of trenbolone acetate and trenbolone acetate when mixed with silver nanoparticles were explored. The aim was to explore the enhancement tendency of silver nanoparticles when used as substrates. Figure 7-2 depicts the comparison of the Raman spectral characterization for a 6ppm trenbolone acetate dopant and Tren ac when mixed with silver nanoparticles.

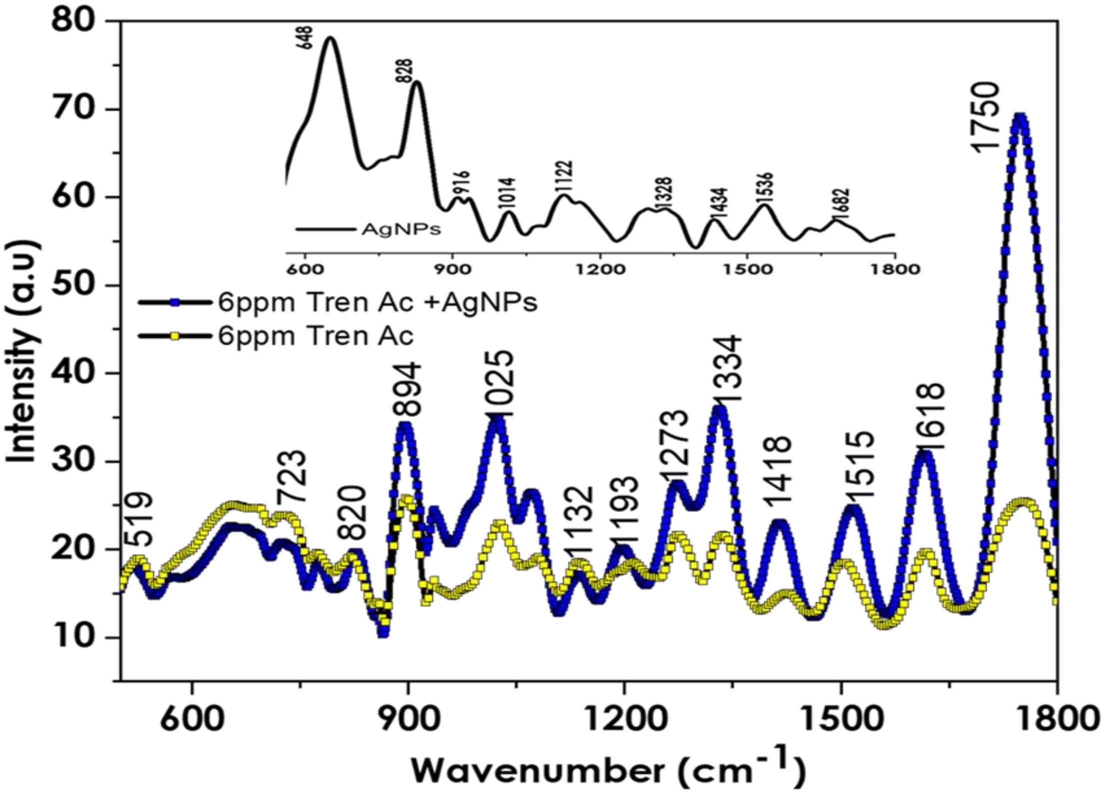

Figure 5-24: Raman and surface-enhanced Raman spectra of trenbolone acetate and Tren Ac when mixed with silver nanoparticles

In Figure 5-24, the tendency of silver nanoparticles to be used as possible substrates for signal enhancement is demonstrated. The results show that all the Raman scatter bands reported an enhanced intensity demonstrating the feasibility of silver nanoparticle substrates as possible enhancers of the Raman scatter bands. Consequently, signal enhancement can be determined as follows;

$$EF = \frac{I_{SERS} - C_{SERS}}{I_{RS} - C_{R.S}} \qquad 5.5$$

where EF is the enhancement factor, I_{SERS} is the intensity of the band (given as area under the band) for the enhanced sample; when in liquid and when dried. C_{SERS} is the concentration of the probed sample when diluted with silver nanoparticles, I_{RS} is the intensity of the sample (area under the band) before adsorbing with silver nanoparticles and the concentration equivalent is C_{RS}.

5.3.3 Orientation of Tren Ac on Silver Nanoparticles using SERS

The interpretation of SERS spectra can provide important information about the orientation of the molecule on the metallic nanoparticles especially in the monolayer regime[34]. SERS can also help to explore the molecular moieties used in the interaction and how strong the adsorption process is. The adsorption process of Tren Ac on silver nanoparticles is also an important aspect that helped to achieve signal enhancement as seen in Figure 5-24. The adsorption can be monitored using the absorbance extinction spectra since the analyte introduces aggregation of nanoparticles in the suspension.

In this section, the resulting SERS signal will be used to explain the adsorption behavior of Tren Ac on the nanoparticles. Adsorption is an important step where the aqueous substrate (AgNPs) chemically interacts with the analyte through chemical groups demonstrating some kind of affinity towards the metal NPs [35].

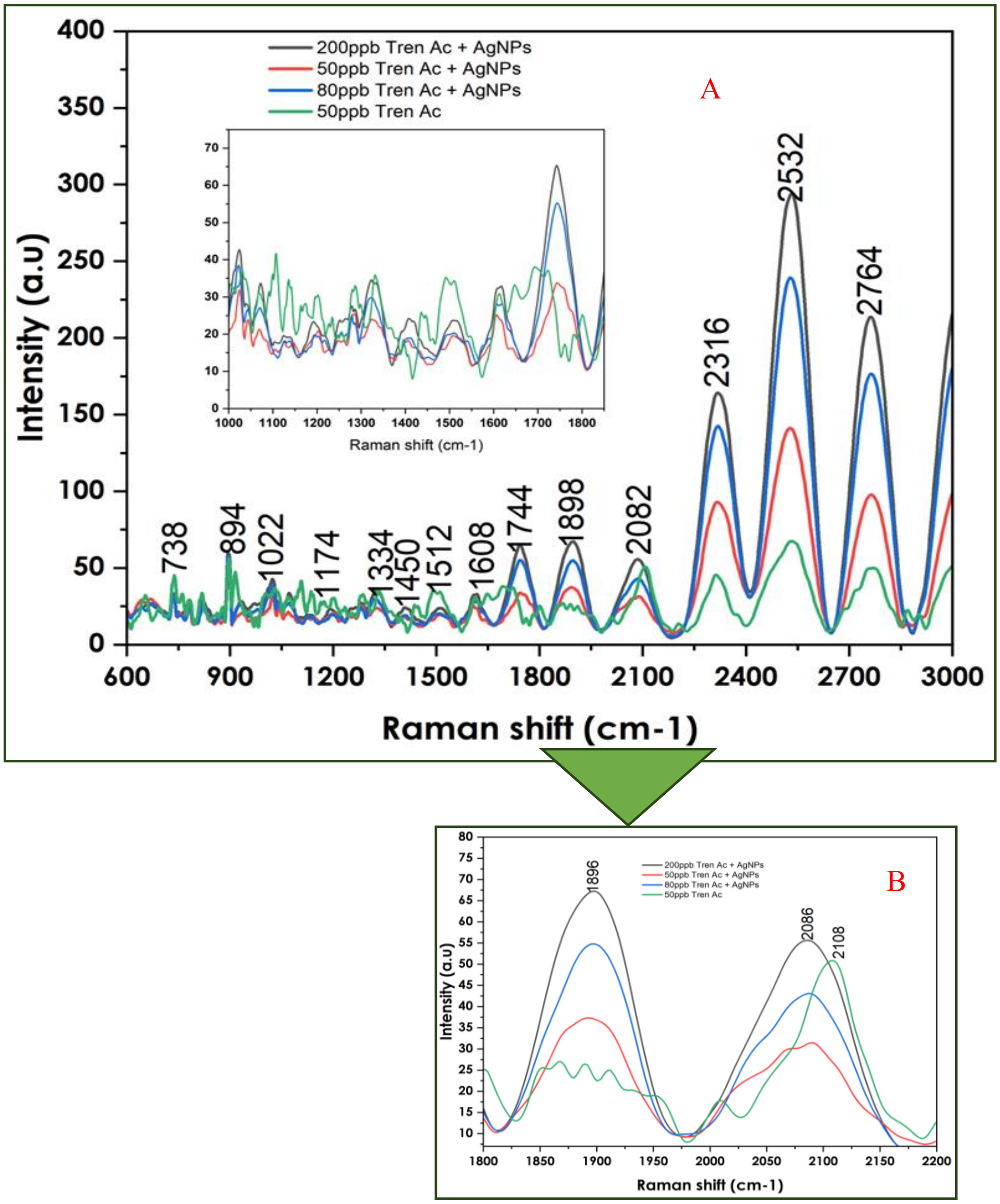

Figure 5-25: Comparison of SERS and Raman spectra of Trenbolone acetate at different concentrations. 7-3B shows band broadening and wavenumber shifts within 1800 to 2200cm^{-1}.

Some of the bands such as 1608,1744 and 1898cm^{-1} could only be detected by adsorbing the molecule with silver nanoparticles. The SERS peak intensity increased with an increase in concentration especially for Raman scatter bands at higher wavelengths. However, for low-wavelengths, there was no clear correlation between the concentration of the analyte with the peak intensity. The low-wavelength region showed more Raman activity and supposedly more interaction between the nanoparticles and the Tren Ac analyte.

The other important observations were peak broadening and wavenumber shift of the spectral bands are the notable features that can be used to distinguish SERS from conventional Raman. It is observed that some peaks are shifted to the lower wavenumber when SERS is introduced. For instance, the peak at 2108cm^{-1} shifts to 2085cm^{-1} in normal Raman while the peak at 617cm^{-1} shifts to 614cm^{-1}. Joydeep *et al*., [36] argues that the magnitude of the wavenumber shift is a measure of the degree of chemical enhancement which is based on the charge transfer of the lone pair of electrons from trenbolone acetate adsorbent as it is transferred to the lowest vacant orbital of the silver nanoparticles.

The shift in some of the wavenumbers is also due to the impact of the surrounding environment on the vibrational modes of the molecule. The adsorption of the molecule on the nanoparticles changes the chemical bonds, hence causing a shift in the wavenumbers. The theoretically obtained results in SERS can be better interpreted using density functional theory which helps to explore the most likely adsorptive site/sites in trenbolone acetate, which provides a clear picture of the charge transfer mechanism in SERS.

Density functional theory analysis on trenbolone acetate showed that the most active/adsorptive site on the molecule is oxygen since it is the most electropositive. Therefore, the interaction between the silver nanoparticles and trenbolone acetate involves the formation of strong ionic compounds between the positively charged silver ions and the negatively charged oxygen atoms in the molecule. This interaction leads to the creation of a shell of Ag_2O around the particle, resulting in a redshift in the plasmon peak. The oxygen atoms in trenbolone acetate provide the electron-rich/dense region that facilitates the adsorption and interaction with the silver nanoparticles, influencing the spectral characteristics observed in the adsorption process. In SERS, the interaction is observed in terms of shift in some of the wavenumbers.

In SERS (experimental), the most prominent wavenumber shifts were reported at 2086cm^{-1} (+ 12 cm^{-1} redshift) which is assigned to the C≡C triple bond functional group, 1608 and 1744cm^{-1} both of which report + 18 cm^{-1} redshift) and are assigned to the carbonyl (C=O) functional group often present in steroids. C=O can be regarded as the most important active site that will cause chemical transformations when adsorbed on silver nanoparticles. The carbonyl group is also polar since carbon is partially positive and oxygen is negative which makes them susceptible to nucleophilic attack. The electrophilicity of the molecule supports this assertion and as such, trenbolone acetate's oxygen molecule at the 1600 – 1750cm^{-1}, functional group provides the most active site for adsorption. Therefore, the shifts in wavenumber within this region provide SERS with its capability to be used as a sensitive and label-free analytical technique when adsorbed on silver nanoparticles.

5.3.4 Theoretical Analysis of SERS using DFT

Surface-enhanced Raman was also explored theoretically with the help of DFT. The Ag 10 nanocluster was imported from the quantum cluster database and then optimized in Gaussian with the BL3YP/LANL2DZ calculation as shown in Figure 5-26. The silver nanocluster, associated with experimental silver nanoparticles are relevant nanoscale representation and presents unique electronic and optical properties that are significantly influenced by quantum effects [24].

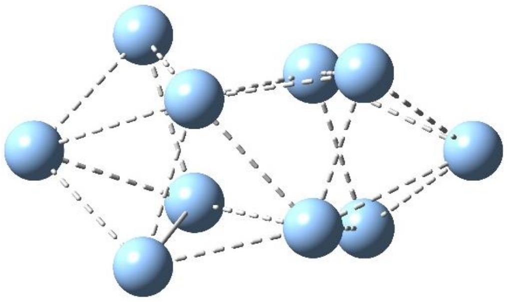

Figure 5-26: Structure of Ag-10 cluster optimized with BL3YP/LANL2DZ.

The next step was to import the optimized molecule of Trenbolone acetate and then adsorb it to the modeled silver nanocluster surface. The two were then optimized again using the same basis set to achieve the lowest conformation of the molecule. Frequency calculations were carried out using the Gaussian 09W program for both trenbolone acetate and Trenbolone acetate adsorbed on the silver nanocluster surface and are presented in Figure 5-27.

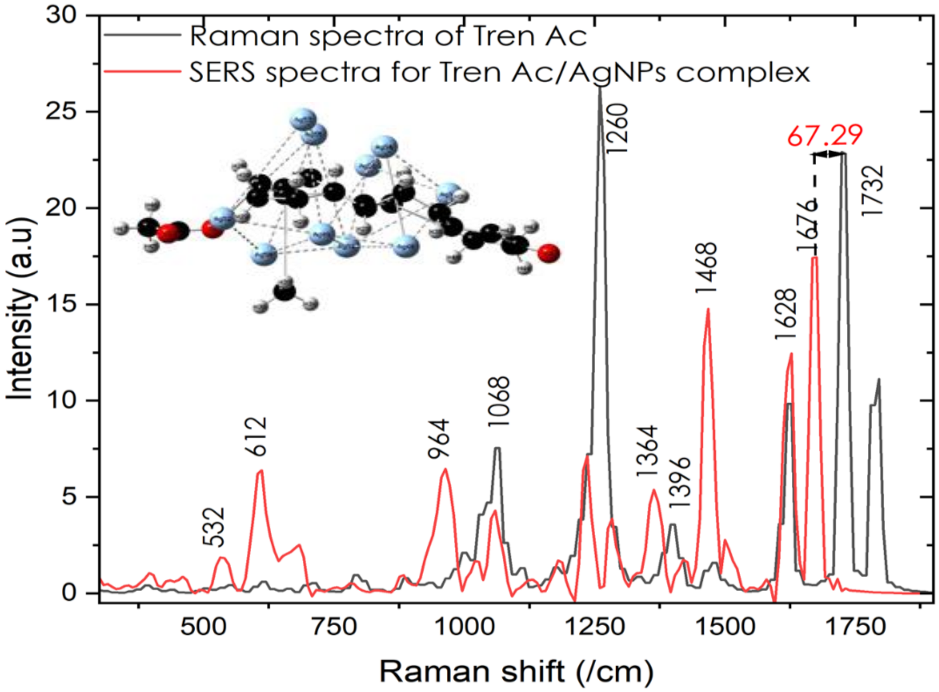

Figure 5-27 SERS simulated spectra for the Ag 10 Tren complex calculated at the B3LYP/LANL2DZ level.

The results show that some of the Raman scatter bands had an enhanced intensity when the analyte was adsorbed on silver nanoparticles. All the low-frequency Raman scatter bands (< 1000) and some of the medium-frequency bands reported a higher enhancement. Bands referred to in this range include 532, 612, 964, 1364, and 1468cm^{-1}. The presence of nanoparticles creates localized surface plasmon resonances that amplify the electric field near the surface, consequently amplifying the Raman signals. Similar results were noted experimentally as previously discussed in 3.1.2. Therefore, the electromagnetic field enhancement from localized surface plasmon is more effective in increasing the vibrational frequency of low-frequency modes.

There were also notable redshifts in some of the Raman scatter bands. For instance, the Raman band at 1724cm^{-1} is assigned to C=O (carbonyl) stretching vibration. The C=O is the strongest vibrational mode due to its significant dipole moment. Upon adsorption, the band redshifts to 1668 cm^{-1}. Other redshifts were noted for 1260, 1364, and 1476cm^{-1}. The bands can be assigned to symmetric bending vibration of methyl groups (δ(CH33), and the C=C stretching. Some of the bands also report a reduction of intensity in the SERS spectrum. Badillo *et al*., [37] noted that functional groups closer to the surface and vertically oriented show a significantly higher enhancement than other functional groups. In this case, the adsorption was more likely through the carbonyl and methyl groups. The theoretical results are consistent with what was presented experimentally in the previous section.

The ability to detect and quantify analytes, Tren Ac in this case based on redshifts without requiring chemical labels highlights the robustness and simplicity of label-free SERS methods. In this work, it is possible to monitor the shifts in Raman scatter bands for different analyte concentrations for building a calibration strategy that can be applied in quantitative analysis.

5.3.5 Conclusion

In this sub-section, the role of silver nanoparticles as possible substrates used in surface-enhanced Raman spectroscopy has been demonstrated. Before this step, the characteristic Raman spectra of trenbolone acetate were obtained and properly assigned with the help of density functional theory. The unique chemical fingerprint of trenbolone acetate was explored for the first time, since to the best of our knowledge, no literature has provided Raman vibrational spectroscopic analysis of the steroid. Besides characterizing trenbolone acetate, the role of silver nanoparticles as possible substrates has been explored. Using nanoparticles in SERS allowed single molecule detection of the molecule. Silver nanoparticles provided its plasmonic property by supporting localized surface plasmon resonances that strongly couple to light at specific wavelengths, leading to a substantial increase in the Raman signal. Using SERS, it was possible to achieve signal enhancement to X 11 orders of magnitude when compared to conventional Raman. The enhancement tendency of silver nanoparticles in SERS allows possible detection of the molecule in matrices such as urine and blood which would be expected in routine doping analysis. Some of the bands that can be used as biomarkers in detecting trenbolone acetate in such complex matrices include 1273, 1334, 1418, 1618, and 1750cm^{-1}. The subtle characteristic peaks are strongly enhanced when using silver nanoparticles. The results formed the basis of a submitted publication and demonstrate that objective four was achieved.

In this section, the adsorption tendency of trenbolone acetate on silver nanoparticles has also been demonstrated. The shift in wavenumbers, especially within the 1600 – 1750 cm^{-1} spectral range provides the most active adsorbent site for silver nanoparticles. Oxygen molecule in the C=O functional group is highly electronegative and as such, would lead to changes in the chemical bonds and the corresponding Raman peaks. The changes in intensity and shifts in specific wavenumbers provide surface-enhanced Raman spectroscopy with its ability in label-free detection of trenbolone acetate and other anabolic steroids used in doping.

5.3.6 Drop-Coating Deposition Raman Spectroscopy

Drop coating deposition Raman was employed as a complementary technique to surface-enhanced Raman spectroscopy. In DCDR, the mixture of trenbolone acetate and silver nanoparticles was dried on a hydrophobic aluminum surface to help pre-concentrate the sample and achieve better signal intensity.

5.3.6.1 Impact of Aliquot Volume

The volume of the aliquot micropipette on the foil was optimized as shown in Figure 5-28.

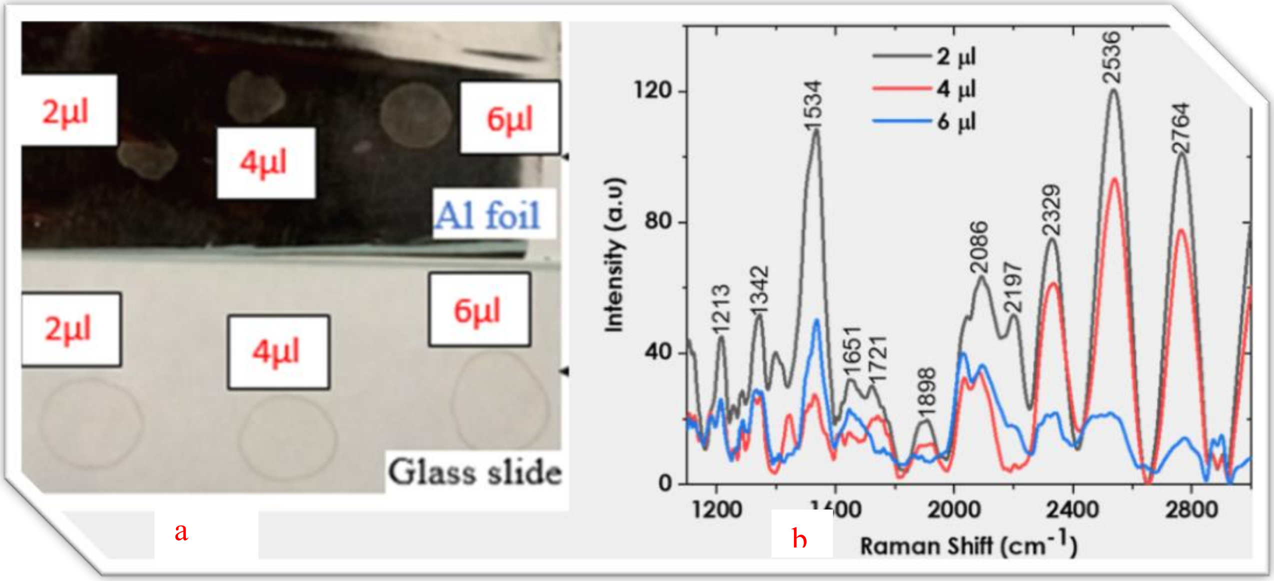

Figure 5-28: Impact of aliquot volume on the size of the coffee ring on both a dried drop on Aluminium foil and glass slide (5-28a) and the impact on the spectral intensity for spectra taken on the edge of the ring after drying on Aluminium foil.

The volume of aliquots that are often deposited ranges from nano to milliliters. Manual aliquot microdroplets are often performed with a volume range of 1 to 10 µl. The other option is to use an ink-jet printer that allows the creation of aliquot volumes to nanoliter dimensions [38]. This work sought to explore the volume that would help to enhance the Raman signal for a particular concentration of trenbolone acetate adsorbed to silver nanoparticles. The results show that a smaller aliquot volume results in better signal intensity. Ortiz *et al*., [39] note that after drying, droplets often have an inhomogeneous distribution of the molecules with many moving toward the edge. The inhomogeneity can be more pronounced for bigger aliquot volumes due to thicker and less uniform coatings. The higher spread of the bigger aliquot also increases the risks of the probe interacting with the substrate, increasing background interference. The signal-to-noise ratio for the deposition spectrum in the low volumes was higher than at larger volumes [39]. The unequal evaporation rate was also found to be a contributing factor in defining the differences in signal intensity.

Halvorson *et al*., [40] observed that 2µl was ideal in using DCDR in aqueous sample volumes and larger sample volumes were not required to improve spectral resolution. The optimized volume displayed a distinct "coffee ring" deposit that allowed for achieving a high signal-to-noise ratio. The small aliquot volume demonstrates the benefits of SERS and DCDR complimentary techniques that leverage very small sample volumes in analytical processes, desirable in doping analysis.

5.3.6.2 Signal Distribution in Coffee Ring Effect

When the drops of a prepared mixture of colloid and trenbolone acetate probe were deposited on the target substrates (aluminum foil and glass slide), the drying effect was such that the mixture moved on the edge of the ring during the evaporation process. Šimáková *et al*., [41] noted that SERS spectra are always influenced by fluctuations in signal intensity and distribution.

Therefore, a suitable volume and appropriate mixtures have to be used for an optimal signal intensity to be found. The optical microscope bright field image of the dried drop of the mixture is shown in Figure 5-29.

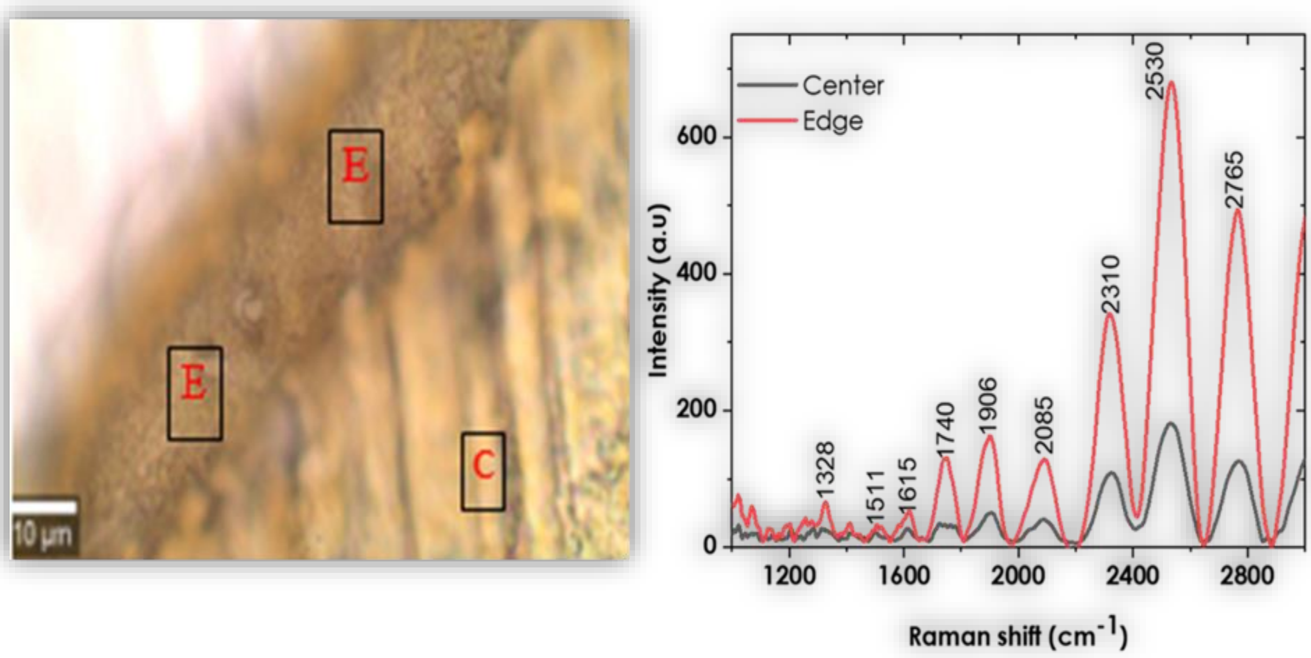

Figure 5-29:The optical image of a dried coffee ring of a probe mixed with silver nanoparticles with E depicting the edge of the ring and C depicts the center. 5-29b signal distribution at the center and edge of the ring using a 785nm laser.

The signal of the SERS analyte was measured at the edge and center of the dried drop. The results showed a lack of homogeneity in terms of how the probe concentrations are distributed. The signal obtained at the edge reported an enhancement factor that is three times more than the spectra obtained at the center of the ring. During spectral acquisition, it was noted that even on the edge of the ring, intensity variation could be observed. The spectra reported in Figure 5-29 are an average of thirty spectra taken at the edge as well as at the center of the ring. The results reported in this work were similar to Li *et al.*, [42] who argued that the ring region gave a higher signal intensity and more Raman features than the central region.

5.3.7 Principal Component Analysis to Confirm Signal Distribution

To explore the (in)homogeneity of the data acquired at the edge and center of the dried drop in the two spectra regions, a principal component analysis was done to assess the (di)similarity in the data acquired in the two regions. Figure 5-30 shows the score plot and the loadings plot for data acquired both at the center and the edge of the dried coffee ring.

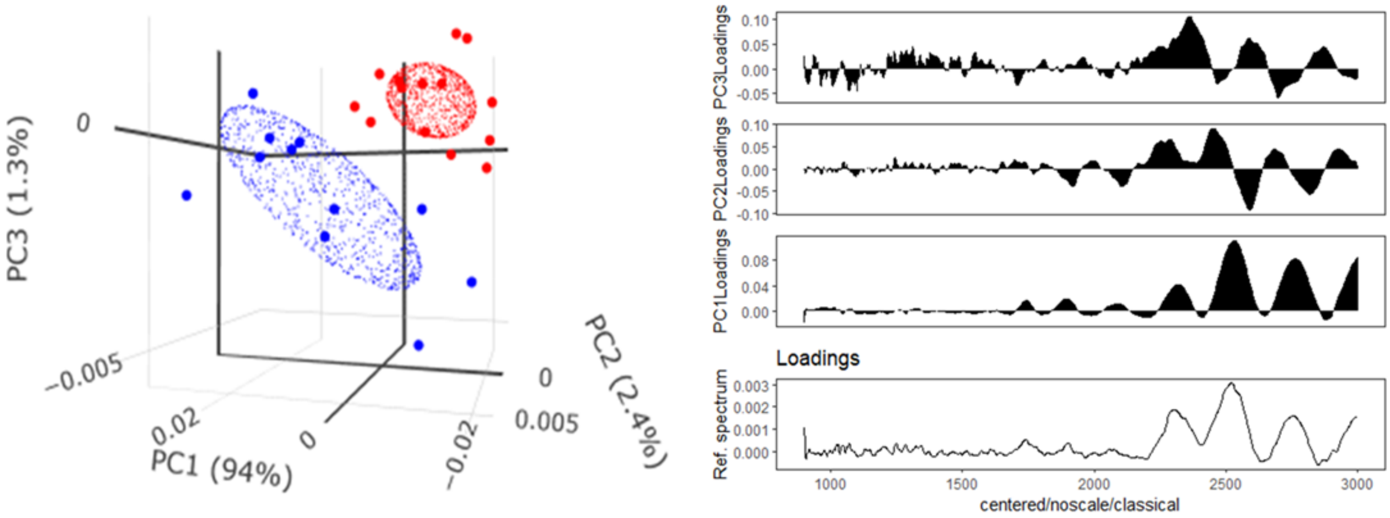

Figure 5-30:Principal component analysis and loadings plot for data acquired at the edge (red) and center (blue) of the coffee ring after the drying of trenbolone acetate and silver nanoparticle SERS mixture.

The score plot showed that data acquired at the edge and center of the ring were inhomogeneous. The spectral classification could be explained using 94% of PC-1, 2.4% of PC-2, and 1.3% of PC-3. Most of the data acquired at the edge of the dried drop are due to positive eigenvalues of the first principal component. The specific bands of this classification are 1650 - 1800cm$^{-1,}$ and all the other bands above 2000cm^{-1}. The classification is thus explained by analyte concentration with those at the edge corresponding to higher intensity bands. Therefore, better characteristic assessment for such probes using drop-coating deposition should be carried out on the edge using a confocal Raman spectrometer system since the edges help to provide an enhanced signal intensity as compared to the spectra obtained at the center.

5.3.8 DCDR and SERS as Complementary Techniques

While silver nanoparticles have been used as reliable substrates that enhance the detection of trenbolone acetate, the desired signal could not be found when the spectra were acquired for a sample in liquid form. Therefore, to achieve an enhanced signal, the sample was dried on the aluminum foil. The signal intensities for conventional Raman, SERS, and DCDRS are shown in Figure 5-31.

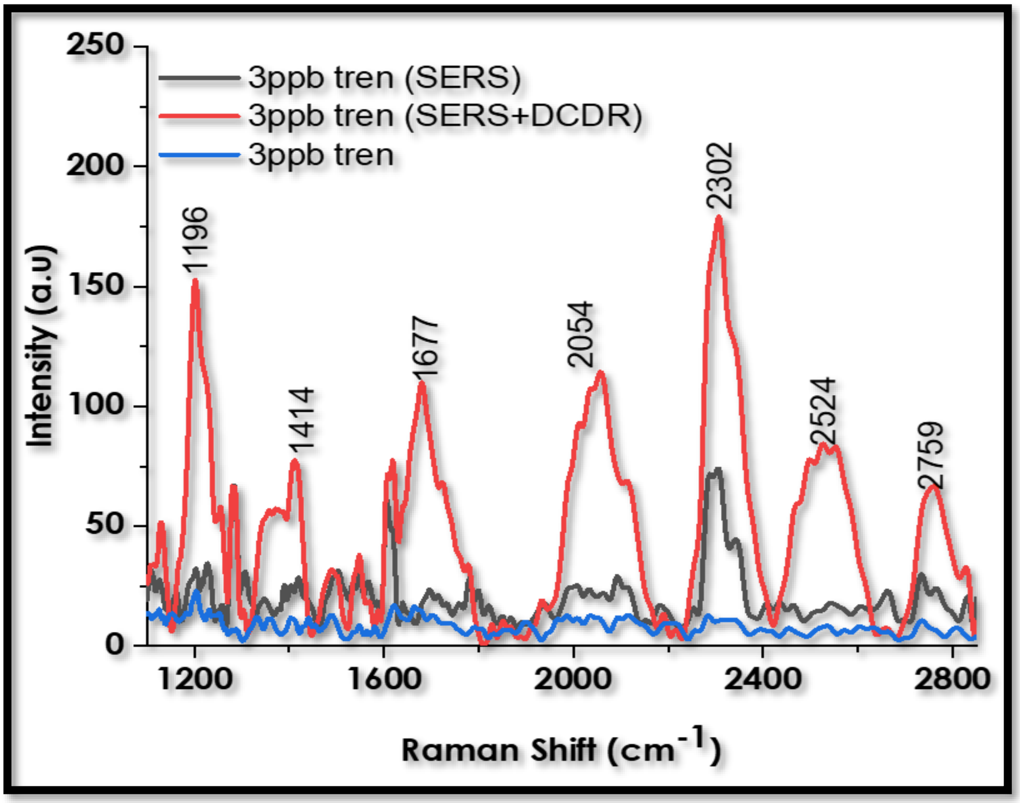

Figure 5-31:Comparing the signal intensity of 3ppm trenbolone acetate using 785nm conventional Raman, SERS in liquid, and SERS after drying a 2µl aliquot mixture of silver nanoparticles and probe on Al foil.

Using equation 5.5, the enhancement factor for SERS+DCDR was obtained to be X 60 while for SERS in liquid, the enhancement factor was noted to be X 11. Therefore, combining SERS and drop coating deposition helps to significantly improve the signal that can be leveraged in analytical detection for sub-ppm analyte concentrations.

The 1196cm^{-1} band can be assigned to the C-O stretching vibration that may as well be associated with the ether linkage that is often associated with any steroid. The band at 1414cm^{-1} can be assigned to the CH_3 rocking and bending vibrations. 1677cm^{-1} is assigned to the C=O stretching vibration which is often due to ketone functional groups associated with steroids [43]. The other bands above 2000cm^{-1} can as well be assigned to C-H stretching vibrations from the aliphatic hydrocarbon chains.

5.3.9 Conclusion

This work has shown that both SERS and drop coating deposition Raman (DCDR) can be used as complementary techniques to improve the signal intensity when probing associated dopant analytes at sub-ppm concentration level. The enhanced signal can help to achieve better sensitivity when detecting dopants like trenbolone acetate in complex matrices as is often the case in anti-doping tests. While DCDR provides a way to preconcentrate the probe and consequently improve signal detection, the optimization process is shown to be critical in achieving desired results. Optimizing the substrate was noted to be key with Aluminum foil providing its hydrophobic and reflective surface that achieves less background interference. The type of laser strength also showed to be important in improving the characterization of silver nanoparticles before they are subsequently applied in SERS. While highly reproducible spectra are obtained when combining SERS and drop-coating deposition, smaller aliquot volumes demonstrated great potential in achieving a better Raman signal, a move that would provide a remarkable breakthrough in demonstrating the feasibility of Raman spectroscopy as a technique that requires very minimal sample volume for analytical purposes. The results provide great insight into the analytical capability of different Raman methodologies in detecting performance-enhancement drugs in anti-doping.

5.4 Density Functional Theory Study of Trenbolone Acetate

This section presents results overview of the theoretical vibrational assignment (Raman, FTIR, and SERS) of trenbolone acetate and how the results compare with what was obtained experimentally. Theoretical computations of trenbolone acetate were performed by using the DFT approach based on the B3LYP/6-31G (d, p) basis set. The molecule was optimized using the same basis set by finding the minimum energy. The molecular electrostatic potential (MEP) surface was studied to ascertain the most active attack zones with the energy gap for trenbolone acetate also obtained. Vibrational analysis was carried out within the most prominent regions based on the potential energy distribution assignments obtained using vibrational energy distribution analysis (VEDA). Combining experimental and theoretical analysis provided better insights into ascertaining the molecule's vibrational bands.

5.4.1 Simulated and Experimental FTIR Spectra of Trenbolone Acetate

The strong infrared absorption observed in the C=O stretching vibration is attributed to the molecular dipole moment generated by this mode of vibration. The simulated infrared data indicates that the bands at 1626 and 1727cm^{-1} exhibit the highest intensity, corresponding to the stretching vibrations of C=C and O=C, respectively, as validated by the theoretical density functional theory (DFT) calculations.

The FTIR spectra simulated in both water and air exhibited bands that closely resembled those observed in Raman spectra, whether simulated or experimental. Consistent with findings in Raman spectroscopy, the range spanning 1500 to 1700cm^{-1} showed the highest infrared activity. This spectral region is attributed to the carbonyl group (C=O), known for its significant polarity and strong absorption of infrared radiation. The polar nature of the carbonyl group accounts for its activity in both infrared and Raman spectroscopies. Moreover, this region hosts the most prominent stretching vibrational peak of the carbonyl group, making it an ideal biomarker functional group for detection using both Raman and infrared techniques. Figure 5-32 shows the simulated and experimental spectra of the trenbolone acetate dopant.

Notably, the FTIR simulation conducted in the air revealed additional infrared active bands compared to those observed in water. Specifically, the DFT simulation in air unveiled a distinct band at 1727cm^{-1}, which was absent in the theoretical calculations performed in water. This difference could be attributed to the dielectric properties of water, which can induce chemical reactions and electron transfers, thereby influencing molecular behavior.

5.4.2 Simulated and Experimental Raman Spectra of Trenbolone Acetate

Experimental and simulated Raman spectra (both in air and in water) are presented in this section. The Raman spectrum obtained experimentally for Tren exhibited a notably closer resemblance to the simulated spectrum in the air compared to that in water. This similarity was assessed by generating a regression curve between the two spectra (experimental versus simulated in both air and water), illustrated in Figure 5-32.

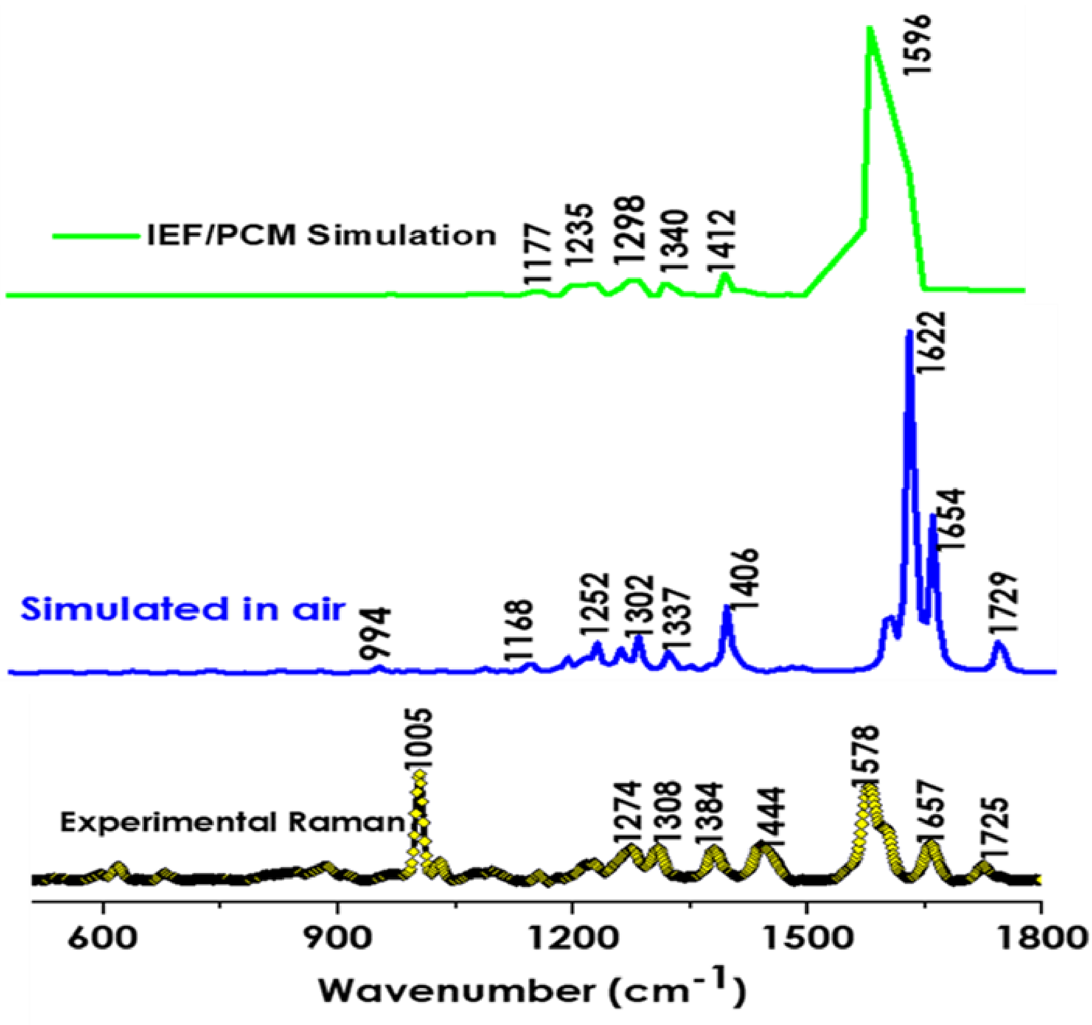

Figure 5-32: Experimental and Simulated Raman spectra of trenbolone Acetate.

It was noted that both the experimental and simulated Raman spectra displayed prominent bands within the spectral range of 1500 to 1760 cm^{-1}. These bands were attributed to vibrations associated with H-C-H bending (1500 -1580 cm^{-1}), C=C stretching (1620 - 1670 cm^{-1}), and O=C stretching (1725 - 1760 cm^{-1}). Typically, this spectral region is characterized by vibrations originating from the ketone (C=O) and alkene (C=C) functional groups.

5.4.3 Vibrational Assignment and PED using VEDA 4 Program

VEDA 4 was used to achieve the potential energy distribution of theoretical vibrational spectra obtained using density functional theory. Before VEDA, the quantum chemical calculations were obtained using a 6-311++G (d, p) basis set. The detailed interpretation of the vibrational spectra was done to obtain a detailed interpretation of the fundamental modes [44]. No scaling was employed and the band assignments are shown in Table 5-2.

Table 5-2: Band assignment for simulated Raman and FTIR spectra of trenbolone acetate.

Simulation wavenumbers (cm^{-1}) DFT Raman (in air)	**Experimental wavenumbers (cm^{-1}) Raman**	**Simulation wavenumbers (cm^{-1}) DFT FTIR (in air)**	**Experimental wavenumbers (cm^{-1}) FTIR**	**Proposed band assignment (PED%)**	**Associated Atom numbers**			
523	519	501	-	O=C-C bend, (14)	2	21	23	-
523	-	-	528	C-C-C-C, out, (12)	13	4	12	5
558	558			C-C-C, bend, (10)	4	5	7	-
611/613	-		649	O-C-O-C, out, (35)	2	23	1	21
624/656	624	624	671	O=CC, bend, (15)	2	21	23	-
748	716	707	750	CC, str, (18)	13	5	-	-
784	-	-	-	C-C=C, bend, (18)	5	12	14	-
791	-	800	-	C-C, str, (11)	6	11	-	-
879	871	894	892	C-C, str (10)	20	22	-	-
922	-	-	-	C-C, str (10)	23	21	-	-
968	973			HCCC, tor, (12)	34	13	5	4
994	1005	-	964	CCC, bend, (11)	20	22	19	-
1012	1046	1038	1031	CC, str (10)	9	7	-	-
1067	1094	1066	1067	O=C, str (10)	1	7	-	-
1121	1160	-	1110	C-C, str (13)	18	15	-	-
1168	-	-	1174	C-C, str (10)	7	5	-	-
1252	1274	1262	1275	H-C-C, bend, (27)	27	8	9	-
1302	1308	-	1329	H-C-C, bend, (11)	25	6	11	-
1337	1384	1337	1374	H-C-C, bend, (23)	25	6	11	-

1406	1418	1402	1402	H-C-O, bend, (12)	26	7	1	-
1471	1444	-	1444	H-C-H, bend, (16)	47	23	46	-
1478	-	-	-	H-C-C-O, tors, (15)	47	23	21	1
1502	1578	-	1539	H-C-H, bend, (32)	35	13	34	-
1622	1657	1621	1666	C=C, str, (57)	19	17	-	-
1729	1725	1727	1759	O=C, str, (88)	3	22	-	-

The chemical equation of Trenbolone acetate is $C_{20}H_{24}O_3$ which implies that it has 135 normal modes as per the formula 3^{n-6} where n is the number of atoms in the molecule. The vibrational modes can be categorized into 45 stretching modes, 46 bending modes, and 44 torsion modes, aligning with the anticipated count of vibrational modes. Similar to other steroids, trenbolone acetate comprises various functional groups such as the ketone group (C=O), the alkene group (C=C), the alkane (C-C and C-H), and the aromatic ring. The acetate group (O=C-O) represents a distinctive functional group that sets this molecule apart from other steroids. The vibrational modes, as outlined in Table 5-2, are active in both infrared (IR) and Raman spectroscopies.

Trenbolone acetate possesses a structural framework comprising three distinct rings. The primary ring is a cyclohexane ring composed of six carbon atoms, serving as the central structural element. The second ring is a cyclopentane ring, featuring five carbon atoms, while the third is an aromatic benzene ring characterized by alternating double bonds. Analysis of Table 5-2 reveals that within the spectral range of 500 to 800cm^{-1}, the bending modes δ (CCC) and δ (OCC) are explained by the bonds. Additionally, this region encompasses out-of-plane wags δ (CCCC) and δ (OCOC), indicating uncoupled bonds undergoing similar angular bending internal coordinates.

Below 1000cm^{-1}, Vedad *et al*., [45] suggest the presence of typical modes such as out-of-plane bending of -CH groups and ring deformations associated with all steroid molecules.

Specifically, for trenbolone acetate, Raman bands were identified at 523, 613, 748, 784, 879, and 922cm^{-1}, corresponding to ring deformation vibrational modes.

Within the spectral range of 1590 to 1800cm^{-1}, vibrational modes associated with double bond stretches, C=C, and O=C moieties are prominent. According to simulated Raman spectra, the most intense band is observed at 1596cm^{-1} in solvation conditions and at 1622cm^{-1} in air. This band, attributed to the CC stretching vibration, contributes 57% of the information, indicating it as the most Raman active mode in the molecule. In FTIR, the band at 1622cm^{-1} is replicated through simulation in a solvent, while in air, the most intense band is at 1727cm^{-1}, assigned to the ν (O=C) vibration. This specific vibration contributes 88% of the potential energy distribution. Notably, the intensity of the FTIR band at 1727cm^{-1} surpasses that observed in Raman spectra. FTIR simulation in water demonstrates better reproducibility of experimental results in the ν (O=C) vibrational mode. A peak at 1727cm^{-1}, observed at 1722cm^{-1} by Vedad *et al.*, [45], is regarded as one of the most prominent peaks useful for distinguishing different forms of estrogen. This peak, characteristic of the carboxyl group, is assigned to ketones and typically found experimentally between 1720-1740cm^{-1}, serving as a marker for the Estrone molecule according to [45].

The spectral region spanning 1200 to 1500cm^{-1} elucidates deformation vibrations with bending normal modes at δ(HCC) (methine group), δ(HCO), and δ(HCH). These normal bending modes are coupled with various internal bending coordinates. Between 700cm^{-1} and 1000cm^{-1}, a combination of ν(CC), δ(CCC), and τ(HCCC) vibrations are observed. As detailed in this section, all vibrational modes are both Raman and infrared active. However, the simulation, as depicted in Table 1, yields more Raman and IR bands compared to experimental data, indicating that some modes possess similar energies, and their corresponding bands are not resolved in the observed spectra. The results obtained using SERS support those generated in localized surface plasmon resonance, showing the capability of the two approaches in label-free sensing of trenbolone acetate.

5.5 Adsorption of Trenbolone Acetate on Ag (1 1 1) Surface; A DFT Study

This sub-chapter explores the use of DFT in exploring the interaction behavior of silver nanoparticles with trenbolone acetate after adsorption.

5.5.1 Introduction

The interaction behavior of any analyte as it is adsorbed on the nanoparticle surface is key in defining the enhancement behavior in SERS. Ideally, how the analyte is anchored on the nanoparticle, the bond strength that exists from the interaction, and the changes in electronic or structural systems are key in spectroscopic applications [46]. Experimental SERS can be complemented with DFT modeling for a better interpretation of the SERS spectra. Besides understanding the specific molecular sites involved in interaction with the metal substrates, it is also possible to explore adsorption geometrics explaining the interaction. In this study, DFT-D has been leveraged to elucidate the molecule-surface interactions of trenbolone acetate on the silver surface. Investigations were done to understand the interaction by employing solvation possibilities using water as the solvent. The results that will be presented to explore the interaction include the adsorption energy, the solvation energy, the total density of states, and the partial density of states, all of which help to ascertain the interaction behavior of trenbolone acetate on the Ag (1 1 1) surface. The adsorption behavior of trenbolone acetate on silver nanoparticles provides a reference for the molecule's detection based on the surface-enhanced Raman spectroscopy (SERS) technique. Guo *et al.*, [47] argues that the sensitivity of SERS is often manipulated by the interaction between the analyte molecules and the metallic nanostructures. Therefore, the adsorption behavior of trenbolone acetate on a silver surface was explored through DFT simulation and experimental SERS.

With the help of DFT, the SERS spectra of the adsorbed molecule will also be interpreted. The computational approach allowed the interpretation of SERS spectra by identifying any possible shifts in the Raman spectral positions after the analyte is adsorbed on the nanoparticles. Using DFT, it was also possible to explore molecular sites that define the analyte/nanoparticle complexing. Therefore, this sub-chapter seeks to respond to the following pertinent questions; such as band positions of the Raman scatter bands, shifts in Raman frequency relative to the normal modes, and identifying sites where the adsorbate gets adsorbed on the nanoparticles. The section also seeks to explore the adsorption geometries and the nature of the active site involved in the chemical reaction. An effective response to these questions will form the basis for a spectroscopy-based analytical technique in detecting and possibly quantifying trenbolone acetate and other drugs often abused in sports.

5.5.2 Computational Details

The DFT-D method Bucko *et al*., [48] which is executed in DMol3 in the Materials Studio BIOVIA environment Issahaku *et al*., [49] was used to do calculations in this section. The method is preferred since it accounts for any possible van der Waals interactions between trenbolone acetate and silver nanoparticles. The generalized gradient approximation (GGA) method was leveraged to approximate the exchange-correlation function since it gave a better description of the electronic system. The double-numerical quality basis set with polarization functions (DNP) was also employed.

5.5.3 The Unit Cell and Surface Construction

The unit cell of bulk silver was optimized based on the 12 x 12 x 12 Monk Horst-Pack mesh of k points. The conjugate gradient method was then used to relax the unit cell. Figure 5-33 shows the schematic representation of the optimized bulk Ag.

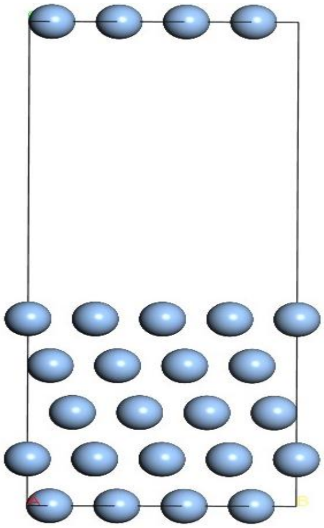

Figure 5-33: Schematic representation of the optimized Bulk Silver unit cell.

After the unit cell, the surface was constructed by using a 3 x 3 supercell based on five layers. The top layer was allowed to relax both with and without the adsorbent. The top layer of the substrate was frozen to ease the time for calculations. A vacuum distance of 20 Å was maintained as that was the most feasible distance that allowed the molecule to be fully placed on the slab without overlapping. Spherical silver nanoparticles were constructed with the bonding crystallographic surface being kept at Ag (1 1 1).

To introduce the adsorbate on the optimized silver slab, the adsorption locator feature on Dmol3 was used. Using the adsorption locator allowed the trenbolone molecule to be introduced on the silver slab generating the adsorbate-sorbate configuration, generated using the Monte Carlo approach which is embedded in the adsorption locator module. The two relaxed for all the degrees of freedom, including having the molecule rotate on the silver surface without further constraints. Minimum energies of the adsorption-adsorbate systems were also obtained in the adsorption locator. Figure 5-34 shows the top view and the surface slab for trenbolone acetate adsorbed on a silver surface.

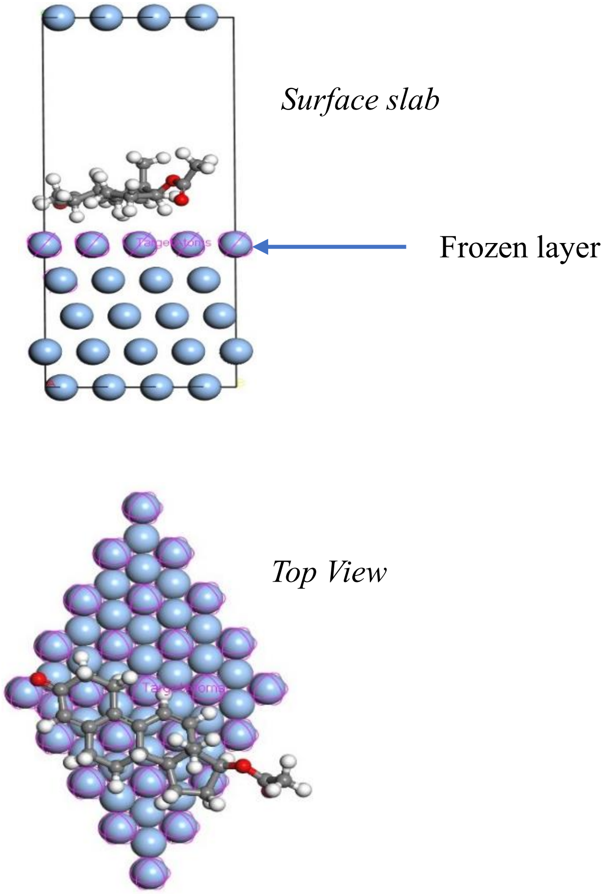

Figure 5-34: Trenbolone acetate adsorbed on Ag (1 1 1) slab with the side and the top view. Color code; oxygen: red, grey: carbon, and white: hydrogen

5.5.4 Adsorption Energy

For a favorable adsorption for the substrate and the adsorbate, the energy of the adsorbed system is lower than when the adsorbate is combined with the substrate, and the adsorption energy will be negative [50].

Understanding the nature of the interaction between trenbolone acetate dopant and silver nanoparticles is critical in explaining the application of SERS in the spectroscopic-based detection of doping materials. The process of adsorption can occur physically or through chemical adsorption derived from dominant forces [51]. Physical interaction arises from weak interactions (≤ 0.4eV) while chemical interactions are a result of stronger forces often ≥ 0.4eV [51]. The chemical bonding process involves the transfer of electrons between the adsorbent and adsorbate. The adsorption energy was carried out using DFT in Dmol3. A summary of the binding energies is presented in Table 5-3.

Table 5-3: Adsorption energies of the surface, adsorbate, and surface + Adsorbate.

System	The energy of the system (eV)
Total surface	-412897.623
Adsorbate	-29068.18521
Surface + Adsorbate	-441908.54
adsorption energy	**-57.28**

The energy released when the molecule is adsorbed on the substrate explains how well the analyte is bound on the substrate. The formula for adsorption energy is given by the formula defined by [52].

$$E_{ads} = (E_{\text{surface}} + E_{\text{adsorbate}}) - E_{(surf+adsorbate)}$$

In the equation, $E_{(surf+adsorbate)}$ describes the total energy of the total energy of the adsorbate combined with the relaxed surface. E_{surf} is the energy of the relaxed surface while $E_{adsorbate}$ is the energy of the relaxed adsorbate. The negative adsorption energy of the system shows that the adsorption of the molecule on the silver slab will be favorable. While doing the simulations for the slab, trenbolone acetate, and the adsorbed system for the adsorption energy calculations, the same exchange-correlation function was used to achieve the desired accuracy. Similarly, geometric relaxation was carried out to lower the forces on the atoms.

The adsorption energy being negative also implies there is a coupling between the nanoparticle plasmon resonance and the adsorbate molecular resonance which are key in both LSPR wave-shift sensing and SERS sensing. Bailey *et al*., [53]explains that the molecular structure and surface affinity influence SERS sensitivity such that having a strong surface affinity provides the highest signal-to-noise ratio in any SERS experiment. Since the adsorption energy is negative, it can be concluded that there is adsorption of trenbolone acetate on silver nanoparticles as the trenbolone molecule will be near the silver surface. The higher density of the molecules near the metal surface results in an enhanced Raman signal [54].

The next step is to prove that trenbolone acetate adsorbs on silver nanoparticles through chemisorption rather than physisorption. While clarifying the adsorption of Triphenylamine on Au(111), Zheng *et al*., [55] leveraged HOMO-LUMO studies to assess the behavior of electron states. Zhang *et al.*, [56] noted that upon adsorption, some of the new unoccupied electron states filled the energy region between the HOMO and LUMO of the free Triphenylamine molecule. The conclusion drawn from the study was that the interaction was chemisorption due to the exchange of electrons. Physisorption involves weak van der Waals forces between the adsorbate and adsorbent while Chemisorption involves the formation of strong chemical bonds between the adsorbate and adsorbent [57]. Chemisorption can also be explained using the core-shell nature of silver nanoparticles as noted in the EDS spectra in the previous sections. We explore the nature of adsorption through frontier molecular orbital analysis and quantum chemical analysis as discussed in section 5.5.5.

5.5.5 Quantum Chemical Calculations

In this section, quantum chemical analysis was done with the help of density functional theory using the Gaussian 09 software package. Table 5-4 shows the atom number distribution, HOMO, and LUMO of trenbolone acetate. Frontier molecular orbital analysis helps to obtain frontier electron density for predicting positions that are most reactive within the π electron system and the subsequent reactions in the conjugated systems. During molecular interactions, the lowest molecular orbital is an electron acceptor and possesses energy corresponding to electron affinity. On the other hand, the highest occupied molecular orbital is the level that donates electrons, and it is linked to the molecule's ionizing potential.

Table 5-4: Optimized structure of Trenbolone Acetate and the frontier molecular orbital density distributions

Optimized Trenbolone Acetate	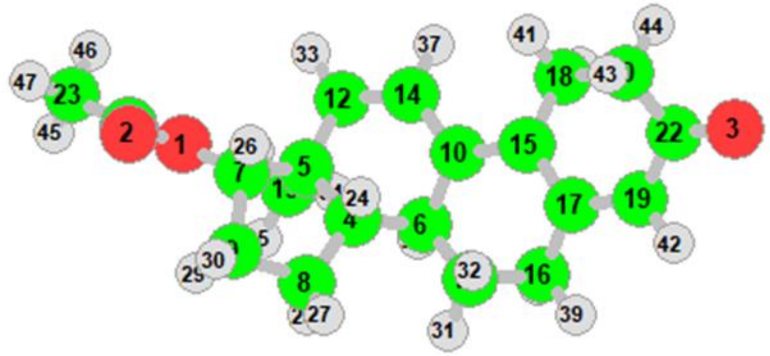

a) MEP	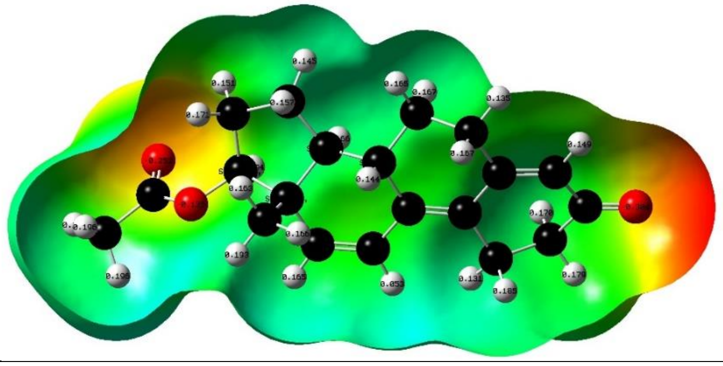
b) HUMO	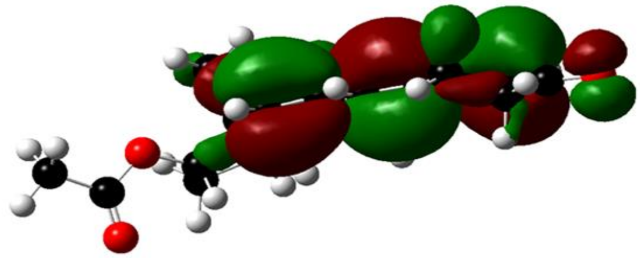
c) LUMO	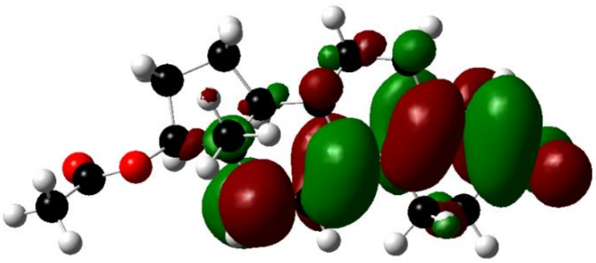

HOMO and LUMO helped to understand the adsorption process of trenbolone acetate on the silver nanoparticle surface. The HOMO and LUMO showed that density was unevenly distributed on the atoms. In the color scheme utilized in the molecular electron potential map (MEP), blue represents regions with electron deficiency, light blue indicates regions that are deficient in electrons, and yellow represent regions that are rich in electrons. Consequently, carbons offer the lowest probability for the analyte to interact with silver. In the model that is structurally optimized, the Highest Occupied Molecular Orbital (HOMO) is situated predominantly along the most negatively charged oxygen along the benzene ring which creates an opportunity for either chemical bonding or electronic transitions. The calculated energy values of the HOMO and LUMO along with other pertinent chemical parameters describing the interaction between Trenbolone acetate and silver nanoparticles are outlined in Table 5-5.

Table 5-5: HOMO and LUMO chemical parameters describing the interaction between Tren Ac and AgNPs.

E_{HOMO}	The energy of the Highest Occupied Molecular Orbital	-0.22365 H	6.086eV
E_{LUMO}	The energy of the Lowest Unoccupied Molecular Orbital	-0.08409 H	-2.288eV
$E_{gap} = E_{LUMO}-E_{HOMO}$	**Energy gap**	**+0.13965 H**	**3.798eV**
$\mu = (E_{LUMO}+E_{HOMO})/2$	Chemical potential	-0.15387 H	2.094 eV
$\eta = (E_{LUMO}-E_{HOMO})/2$	Chemical hardness	+0.069825 H	1.899eV
$\chi = -(E_{LUMO}+E_{HOMO})/2$	Electronegativity	+0.15387 H	-2.094 eV
$\omega = \frac{\chi^2}{2\eta}$	Electrophilicity index	+0.1696 H	1.154 eV

The band gap energy is consistent with the absorbance band obtained using UV-VIS spectroscopy for trenbolone acetate. The absorbance band was found to be 348nm wide. Therefore, the band gap energy can be obtained mathematically as;

$$E = \frac{hc}{\lambda} \qquad 5.6$$

$=\frac{6.63*10^{-34}*3*10^{8}}{348*10^{-9}} = 5.7*10^{-19}J$ which can be converted to eV:

1eV = $1.6*10^{-19}$;

Therefore, E = 3.56eV, which only slightly deviates from the computational calculation results.

Therefore, the minimum energy that will be required to excite an electron from HOMO to LUMO where it can participate in the reaction. The experimentally obtained band gap for silver nanoparticles based on its absorbance band is given as;

$$\frac{6.63*10^{-34}*3*10^{8}}{408*10^{-9}} = 4.875 * 10^{-19} \text{ J;}$$

From equation 9.1, the energy in eV is 3.05eV.

It can be observed that the reacting species have band gap values that are close indicating that their energy levels are well-aligned and that there is efficient charge transfer or chemical reactions between them. This alignment of band gaps allows for effective interaction between the species, facilitating processes like electron transfer or the formation of chemical bonds. Essentially, when the band gaps of reacting species are close, it signifies a favorable match in their electronic structures, promoting strong interactions. The transfer of electrons also shows that the adsorption process is chemisorption rather than physisorption.

Other than the band gap, the other molecular orbital parameter that was explored is the chemical potential that serves as a measure to evaluate a molecule's tendency to explain the reactivity and stability of the molecule. The chemical potential of trenbolone acetate is way less than the band gap which explains the ease with which trenbolone acetate can participate in a chemical reaction. While the band gap is 3.798eV, the chemical potential (energy required to add the molecule to a response) is 2.094eV. Therefore, trenbolone acetate will easily react.

The chemical potential is also higher than the chemical hardness which often explains the molecule’s resistance to engaging in reaction. Therefore, the fact that chemical hardness is lower than chemical potential shows that Tren Ac readily participates in a reaction. On the other hand, electronegativity and the electrophilicity index indicate a molecule's capability to attract electrons and its electrophilic potency, respectively. The higher electronegativity also supports the molecule's tendency to attract positively charged ions towards it. Hence, although Density Functional Theory (DFT) has offered insights into the opto-molecular behavior of trenbolone acetate. The adsorption studies and the spectroscopic studies show changes in the electronic structure of the molecule upon binding on silver nanoparticles which is a significant interaction that gives remarkable insights into using SERS as an approach for the detection of the molecule. The nanoparticle-molecule interaction results in the mutual excitation of the Raman polarizability from the local electromagnetic field hence generating an enhanced Raman signal of the molecule [58]. Therefore, the experimental results obtained in sub-chapter 5.4 are hereby supported theoretically with emphasis on the nature of the interaction between trenbolone acetate molecule and silver nanoparticles.

5.5.6 Density of States

To have a better understanding of the interactions between the Ag (1 1 1) surface and the Tren Ac adsorbate, the electronic properties were studied using total density of states (TDOS) and partial density of states (PDOS). TDOS and PDOS were obtained for isolated pristine silver nanoparticles Ag (1 1 1) and trenbolone acetate models as well as trenbolone acetate adsorbed on silver nanoparticles. Water was used as a solvent to mimic what was done in the lab. From the TDOS plots in Figure 5.35, the pristine Ag (1 1 1) surface has peaks at and below the Fermi level which is often the case for metals.

The TDOS shows peaks at the Fermi level and below as well as above the Fermi level for silver. More peaks are reported below the Fermi level between -20eV and -7.5eV. There is only one notable peak above the Fermi level. After the adsorption of trenbolone acetate on silver, the calculated total density of state was noted to be similar to what was noted in silver nanoparticles. However, after adsorption, a more intense peak was obtained at around -10eV.

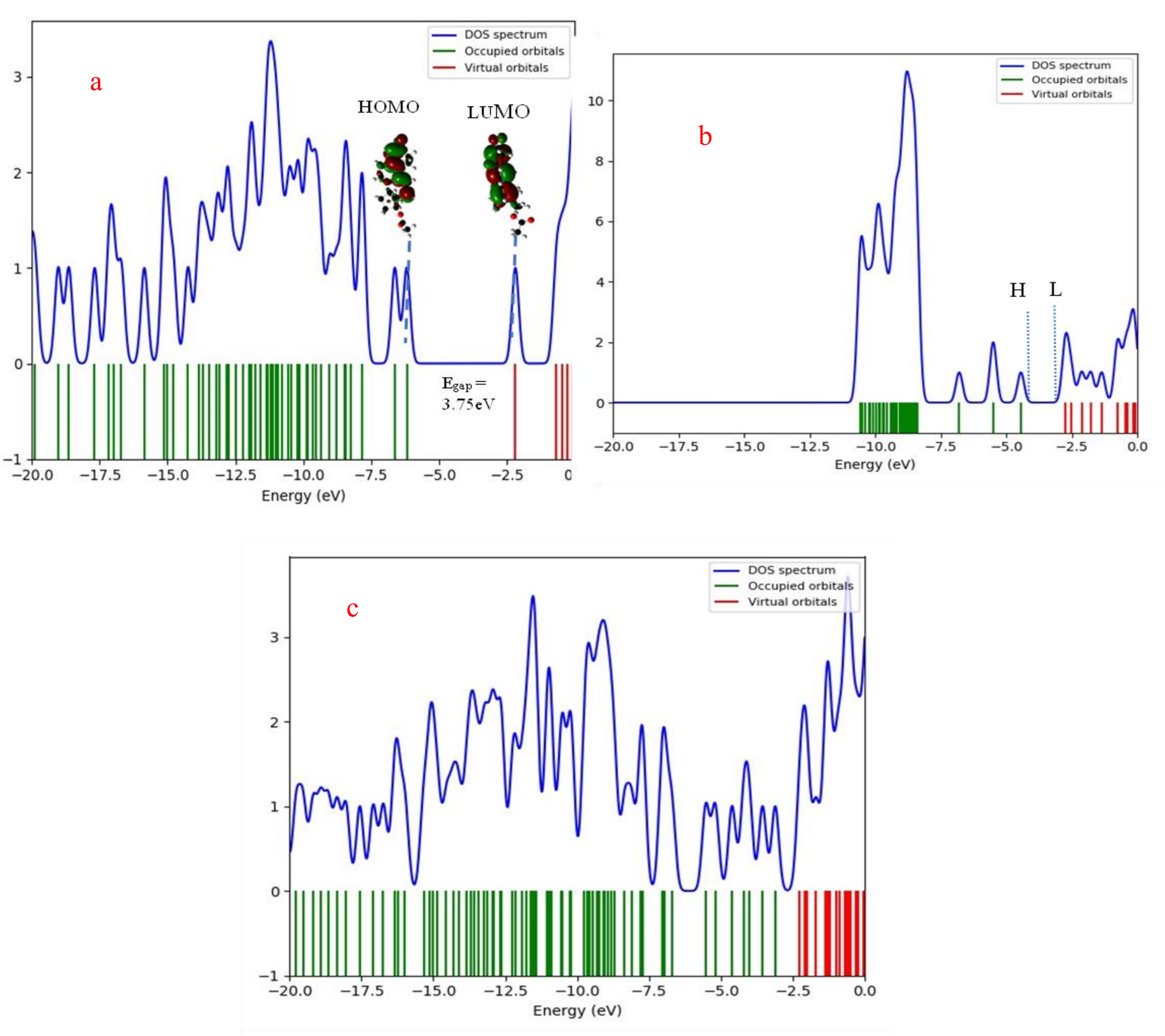

Figure 5-35: The TDOS was calculated using DFT-D/GGA formalism for Ag (a), Trenbolone acetate (b), and Ag/Tren Ac complex (c).

The Fermi level often represents zero energy value (0.0eV) at which the valence band is at its maximum and the electrons are likely to be found. Therefore, having a new and more intense peak between -7.5eV to -10eV implies that trenbolone acetate is introducing new states that are occupied by electrons and which are then transferred to the AgNPs surface. Therefore, the adsorbent is likely to have a significant influence on the electronic structure and physical properties of pristine silver nanoparticles. The fading of the silver nanoparticle peak above the fermi level indicates that trenbolone acetate is accepting electrons from silver, hence depleting the number of electrons in this region [59]. The electron transfer from silver nanoparticles to trenbolone acetate results in changes in the chemical bonding and reactivity among other properties. The adsorption energy results show that the interaction of the trenbolone acetate molecule with silver is strongest with most negative energy values between -12.5eV and -7.5eV.

The other observation made was the reduction in the band gap after trenbolone acetate was adsorbed on the silver nanoparticles. The band gaps for the obtained density of states can be summarized below;

E_{gap} for Tren Ac 3.75eV

E_{gap} for silver nanoparticle 2.2eV

Egap of Tren Ac/AgNPs complex 1.3eV

Therefore, the interaction energy can be calculated based on the equation given by Shukla *et al.*, [60].

Interaction energy = $E_{\text{Tren Ac/AgNPs}} - [E_{\text{AgNps}} + 2E_{\text{Tren}}]$

$= 1.3 - [2.2 + 2*3.75]$

= -8.4eV

The high value of interaction energy shows that there is strong adsorption between Tren Ac and silver nanoclusters and that the interacted system is thermodynamically favorable.

DOS is important in explaining surface-enhanced Raman spectroscopy, especially using chemical enhancement mechanisms rather than electromagnetic enhancement. Cong *et al*., [61] explain that chemical transfer between the substrate/ nanoparticle and analyte changes the distribution of electron density of the molecules. Consequently, there is more polarizability and enhanced Signals reported in enhanced Raman spectroscopy. Unlike the EM enhancement strategy which enhances the Raman signal by 10^{15}, chemical transfer enhances the signals to a tune of 10^{3} for a metal-molecular system. In such a system, the direction where the metal is aligned with the analyte will dictate the charge transfer process. Positioning is influenced by how the Fermi level is located within the metal as well as the HOMO/LUMO positions within the molecule. The highest level of photoinduced charge transfer often happens when the charges are transferred to or from the levels that are close to the Fermi level. Therefore, an increased density of the state near the Fermi level contributes to SERS as noted by Muehlethalel *et al*., [62] who enhanced the density of the states by introducing oxygen in molecules, facilitating exciton resonance. According to Fermi principles, the probability for electrons to shift is linearly related to the density of states around the Fermi level in the chemical transfer process [61].

5.5.7 Mulliken Charge Distribution and Bond Length

The Mulliken charge distribution is a crucial concept in understanding the electronic structure and properties of molecules. In this study, Mulliken charge distribution on trenbolone acetate molecule was carried out to understand the distribution of electronic charge on the molecule, information that also contributes to explaining how the molecule interacts and adsorbs on the substrate. The Mulliken charges are also associated with other molecular properties like dipole moment and polarizability that contribute to SERS behavior for both chemical and electromagnetic enhancement. Figure 5-36 shows the Mulliken charge distribution in trenbolone acetate.

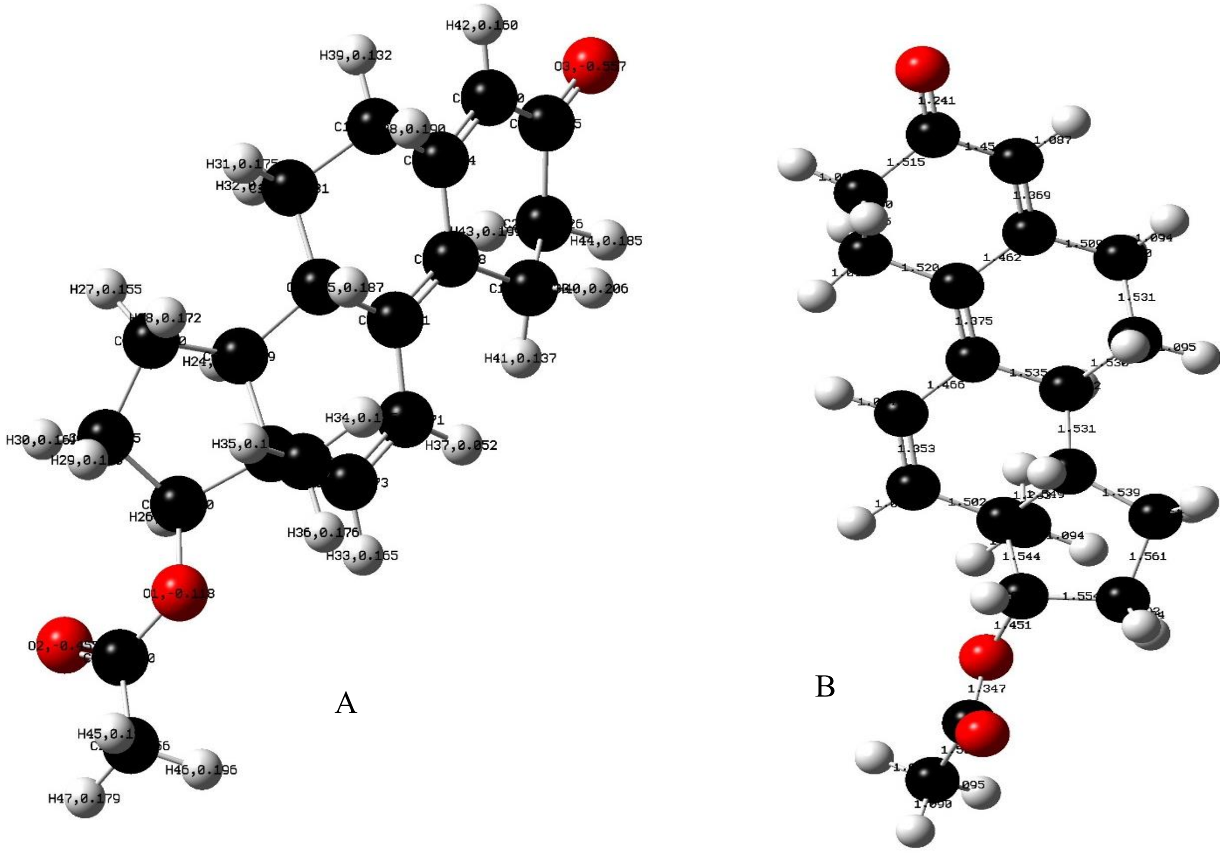

Figure 5-36: Mulliken Charge distribution (A) and bond length (B) for Trenbolone acetate molecule.

From the Mulliken charge distribution, O_3 is the most negatively charged atom (-0.587eV) and as such, most available for electrostatic interaction when adsorbed on the surface. The most electronegative atom has the highest tendency to attract electrons, resulting in a higher degree of polarization enhancing the Raman signal[63]. In terms of bond length, O_3 exhibits one of the lowest bond lengths ($1.241\mathring{A}$) which implies that it is loosely held and can easily engage in reaction. Therefore, by leveraging Mulliken charges, it is possible to refine detection methods to make them more sensitive and specific. For example, understanding how charge distributions change upon binding can improve the design of sensors that detect biomolecular interactions.

5.5.8 Conclusion

This work has demonstrated that density functional theory can be used as a computational and interpretative tool that can help to elucidate the chemical reactivity of trenbolone acetate with silver nanoparticles. In the work, theoretical studies about the affinity of silver ions Tren Ac at a molecular level have been demonstrated. DFT has helped to underscore the chemical transfer capability of trenbolone acetate and the ease with which the molecule can interact with silver nanoparticles. Through the frontier orbitals, HOMO and LUMO, it was possible to explore the chemical reactivity and molecular interactions of trenbolone acetate and silver nanoparticles. The DFT simulation showed that O^{2-} was the most negative atom in trenbolone acetate and would be easily attracted to silver nanoparticles forming a complex. The process is defined by the transfer of electrons between the substrate and analyte from HOMO to LUMO.

DFT has been used as an effective quantum mechanical modeling tool to study the adsorption tendency of trenbolone acetate on silver nanoparticles. In this section, DFT has been employed to analyze the molecular structures, energies, and vibrational frequencies using theoretical computations. With the help of DFT, it was possible to explore the vibrational frequencies of trenbolone acetate, comparable to what was achieved experimentally.

This section has also shown that surface-enhanced Raman is credited to be one of the most feasible spectroscopic techniques that can elucidate the orientation and the adsorption behavior of a molecule onto the metal surface based on scattering enhancement. Dastafkan *et al*., [35] already demonstrated that the relative enhancement of some of the SERS bands could be used to ascertain the orientation of a molecule on nanoparticles based on surface selection rules. Unlike in the previous section where the chemical reactivity of trenbolone acetate was carried out, this section theoretically explores the adsorption mechanism of Trenbolone acetate on silver nanoparticles. The most active adsorption sites were explored with the feasibility of SERS as a vibrational-based analytical tool applicable to sensing being demonstrated.

References

[1] M. Z. Alhamid, B. S. Hadi, and A. Khumaeni, "Synthesis of silver nanoparticles using laser ablation method utilizing Nd:YAG laser," *AIP Conf. Proc.*, vol. 2202, no. 1, p. 020013, Dec. 2019, doi: 10.1063/1.5141626.

[2] L. Mulfinger, S. D. Solomon, M. Bahadory, A. V. Jeyarajasingam, S. A. Rutkowsky, and C. Boritz, "Synthesis and Study of Silver Nanoparticles," *J. Chem. Educ.*, vol. 84, no. 2, p. 322, Feb. 2007, doi: 10.1021/ed084p322.

[3] J. Ijaz Hussain, S. Kumar, A. Adil Hashmi, and Z. Khan, "Silver nanoparticles: preparation, characterization, and kinetics," *Adv. Mater. Lett.*, vol. 2, no. 3, pp. 188–194, Sep. 2011, doi: 10.5185/amlett.2011.1206.

[4] L. M. Moreira *et al.*, "Thermo-optical properties of silver and gold nanofluids," *J. Therm. Anal. Calorim.*, vol. 114, no. 2, pp. 557–564, Nov. 2013, doi: 10.1007/s10973-013-3021-7.

[5] T. E. Agustina, W. Handayani, and C. Imawan, "The UV-VIS Spectrum Analysis From Silver Nanoparticles Synthesized Using Diospyros maritima Blume. Leaves Extract," presented at the 3rd KOBI Congress, International and National Conferences (KOBICINC 2020), Atlantis Press, Jun. 2021, pp. 411–419. doi: 10.2991/absr.k.210621.070.

[6] M. Alhajj, Md. Safwan Abd Aziz, A. A. Salim, S. Sharma, W. H. A. Kamaruddin, and S. K. Ghoshal, "Customization of structure, morphology and optical characteristics of silver and copper nanoparticles: Role of laser fluence tuning," *Appl. Surf. Sci.*, vol. 614, p. 156176, Mar. 2023, doi: 10.1016/j.apsusc.2022.156176.

[7] M. H. U. Bhuiyan, R. Saidur, M. A. Amalina, R. M. Mostafizur, and A. Islam, "Effect of Nanoparticles Concentration and Their Sizes on Surface Tension of Nanofluids," *Procedia Eng.*, vol. 105, pp. 431–437, Jan. 2015, doi: 10.1016/j.proeng.2015.05.030.

[8] A. Baladi and R. Sarraf Mamoory, “Investigation of different liquid media and ablation times on pulsed laser ablation synthesis of aluminum nanoparticles,” *Appl. Surf. Sci.*, vol. 256, no. 24, pp. 7559–7564, Oct. 2010, doi: 10.1016/j.apsusc.2010.05.103.

[9] H. S. Desarkar, P. Kumbhakar, and A. K. Mitra, “Effect of ablation time and laser fluence on the optical properties of copper nano colloids prepared by laser ablation technique,” *Appl. Nanosci.*, vol. 2, no. 3, pp. 285–291, Sep. 2012, doi: 10.1007/s13204-012-0106-8.

[10] F. Hajiesmaeilbaigi, A. Mohammadalipour, J. Sabbaghzadeh, S. Hoseinkhani, and H. R. Fallah, “Preparation of silver nanoparticles by laser ablation and fragmentation in pure water,” *Laser Phys. Lett.*, vol. 3, no. 5, p. 252, Dec. 2005, doi: 10.1002/lapl.200510082.

[11] V. Amendola, S. Polizzi, and M. Meneghetti, “Free Silver Nanoparticles Synthesized by Laser Ablation in Organic Solvents and Their Easy Functionalization,” *Langmuir*, vol. 23, no. 12, pp. 6766–6770, Jun. 2007, doi: 10.1021/la0637061.

[12] R. Bola Sampol, “Preparation of silver nanoparticles by laser ablation in water,” Jun. 2014, Accessed: Mar. 02, 2024. [Online]. Available: https://diposit.ub.edu/dspace/handle/2445/59760

[13] M. Hernández-Maya, P. Rivera-Quintero, R. Ospina, J. H. Quintero-Orozco, and A. C. García-Castro, “Ablation energy, water volume and ablation time: Gold nanoparticles obtained through by pulsed laser ablation in liquid,” *J. Phys. Conf. Ser.*, vol. 1386, no. 1, p. 012062, Nov. 2019, doi: 10.1088/1742-6596/1386/1/012062.

[14] H. A. Alluhaybi, S. K. Ghoshal, W. N. W. Shamsuri, B. O. Alsobhi, A. A. Salim, and G. Krishnan, “Pulsed laser ablation in liquid assisted growth of gold nanoparticles: Evaluation of structural and optical features,” *Nano-Struct. Nano-Objects*, vol. 19, p. 100355, Jul. 2019, doi: 10.1016/j.nanoso.2019.100355.

[15] Q. Guo, Y. Peng, and K. Chao, “Raman enhancement effect of different silver nanoparticles on salbutamol,” *Heliyon*, vol. 8, no. 6, p. e09576, Jun. 2022, doi: 10.1016/j.heliyon.2022.e09576.

[16] N. Joshi, N. Jain, A. Pathak, J. Singh, R. Prasad, and C. P. Upadhyaya, “Biosynthesis of silver nanoparticles using Carissa carandas berries and its potential antibacterial activities,” *J. Sol-Gel Sci. Technol.*, vol. 86, no. 3, pp. 682–689, Jun. 2018, doi: 10.1007/s10971-018-4666-2.

[17] A. T. Lewis *et al.*, “Mirrored stainless steel substrate provides improved signal for Raman spectroscopy of tissue and cells,” *J. Raman Spectrosc.*, vol. 48, no. 1, pp. 119–125, 2017, doi: 10.1002/jrs.4980.

[18] K. Gudun, Z. Elemessova, L. Khamkhash, E. Ralchenko, and R. Bukasov, “Commercial Gold Nanoparticles on Untreated Aluminum Foil: Versatile, Sensitive, and Cost-Effective SERS Substrate,” *J. Nanomater.*, vol. 2017, p. e9182025, Apr. 2017, doi: 10.1155/2017/9182025.

[19] L. Cui, H. J. Butler, P. L. Martin-Hirsch, and F. L. Martin, “Aluminium foil as a potential substrate for ATR-FTIR, transflection FTIR or Raman spectrochemical analysis of biological specimens,” *Anal. Methods*, vol. 8, no. 3, pp. 481–487, 2016, doi: 10.1039/C5AY02638E.

[20] S. Marimuthu *et al.*, “Evaluation of green synthesized silver nanoparticles against parasites,” *Parasitol. Res.*, vol. 108, no. 6, pp. 1541–1549, Jun. 2011, doi: 10.1007/s00436-010-2212-4.

[21] R. Geethalakshmi and D. Sarada, “Gold and silver nanoparticles from Trianthema decandra: synthesis, characterization, and antimicrobial properties,” *Int. J. Nanomedicine*, vol. 7, pp. 5375–5384, Oct. 2012, doi: 10.2147/IJN.S36516.

[22] K. Maaz, *Silver Nanoparticles: Fabrication, Characterization and Applications*. BoD – Books on Demand, 2018.

[23] R. C. Fierascu, I. R. Bunghez, R. Somoghi, I. Fierascu, and R. M. Ion, "CHARACTERIZATION OF SILVER NANOPARTICLES OBTAINED BY USING ROSMARINUS OFFICINALIS EXTRACT AND THEIR ANTIOXIDANT ACTIVITY," *Silver Nanoparticles*.

[24] C. Gellini, M. Macchiagodena, and M. Pagliai, "Adsorption Geometry of Alizarin on Silver Nanoparticles: A Computational and Spectroscopic Study," *Nanomaterials*, vol. 11, no. 4, p. 860, Mar. 2021, doi: 10.3390/nano11040860.

[25] P. Baruah, A. Sharma, and A. Khare, "Role of confining liquids on the properties of Cu@Cu2O nanoparticles synthesized by pulsed laser ablation and a correlative ablation study of the target surface," *RSC Adv.*, vol. 9, May 2019, doi: 10.1039/C9RA00197B.

[26] S. Unser, I. Bruzas, J. He, and L. Sagle, "Localized Surface Plasmon Resonance Biosensing: Current Challenges and Approaches," *Sensors*, vol. 15, no. 7, pp. 15684–15716, Jul. 2015, doi: 10.3390/s150715684.

[27] I. Oshina and J. Spigulis, "Beer–Lambert law for optical tissue diagnostics: current state of the art and the main limitations," *J. Biomed. Opt.*, vol. 26, no. 10, p. 100901, Oct. 2021, doi: 10.1117/1.JBO.26.10.100901.

[28] T. Mayerhöfer, A. Pipa, and J. Popp, "Beer's law – why integrated absorbance depends linearly on concentration," *ChemPhysChem*, vol. 20, pp. 2748–2753, Sep. 2019, doi: 10.1002/cphc.201900787.

[29] J. A. Myers, B. S. Curtis, and W. R. Curtis, “Improving accuracy of cell and chromophore concentration measurements using optical density,” *BMC Biophys.*, vol. 6, no. 1, p. 4, Apr. 2013, doi: 10.1186/2046-1682-6-4.

[30] R. Alvarez-Puebla, L. M. Liz-Marzán, and F. J. García de Abajo, “Light Concentration at the Nanometer Scale,” *J. Phys. Chem. Lett.*, vol. 1, no. 16, pp. 2428–2434, Aug. 2010, doi: 10.1021/jz100820m.

[31] S. Hajizadeh, K. Farhadi, M. Forough, and R. E. Sabzi, “Silver nanoparticles as a cyanide colorimetric sensor in aqueous media,” *Anal. Methods*, vol. 3, no. 11, pp. 2599–2603, Nov. 2011, doi: 10.1039/C1AY05567D.

[32] A. Kheirandish, N. Sepehri Javan, and H. Mohammadzadeh, “Modified Drude model for small gold nanoparticles surface plasmon resonance based on the role of classical confinement,” *Sci. Rep.*, vol. 10, no. 1, p. 6517, Apr. 2020, doi: 10.1038/s41598-020-63066-9.

[33] M. Kahraman, Ö. Aydın, and M. Çulha, “Oligonucleotide-Mediated Au–Ag Core–Shell Nanoparticles,” *Plasmonics*, vol. 4, no. 4, pp. 293–301, Dec. 2009, doi: 10.1007/s11468-009-9105-3.

[34] A. Isabel Pérez-Jiménez, D. Lyu, Z. Lu, G. Liu, and B. Ren, “Surface-enhanced Raman spectroscopy: benefits, trade-offs and future developments,” *Chem. Sci.*, vol. 11, no. 18, pp. 4563–4577, 2020, doi: 10.1039/D0SC00809E.

[35] K. Dastafkan, M. Khajeh, M. Bohlooli, M. Ghaffari-Moghaddam, and N. Sheibani, “Mechanism and behavior of silver nanoparticles in aqueous medium as adsorbent,” *Talanta*, vol. 144, pp. 1377–1386, Nov. 2015, doi: 10.1016/j.talanta.2015.03.065.

[36] J. Chowdhury, J. Sarkar, R. De, M. Ghosh, and G. B. Talapatra, "Adsorption of 2-amino-6-methylbenzothiazole on colloidal silver particles: Quantum chemical calculations and surface enhanced Raman scattering study," *Chem. Phys.*, vol. 330, no. 1, pp. 172–183, Nov. 2006, doi: 10.1016/j.chemphys.2006.08.016.

[37] I. Badillo-Ramírez, S. A. J. Janssen, G. Soufi, R. Slipets, K. Zór, and A. Boisen, "Label-free SERS assay combined with multivariate spectral data analysis for lamotrigine quantification in human serum," *Microchim. Acta*, vol. 190, no. 12, p. 495, Dec. 2023, doi: 10.1007/s00604-023-06085-3.

[38] D. Zhang, Y. Xie, M. F. Mrozek, C. Ortiz, V. J. Davisson, and D. Ben-Amotz, "Raman Detection of Proteomic Analytes," *Anal. Chem.*, vol. 75, no. 21, pp. 5703–5709, Nov. 2003, doi: 10.1021/ac0345087.

[39] C. Ortiz, D. Zhang, Y. Xie, A. E. Ribbe, and D. Ben-Amotz, "Validation of the drop coating deposition Raman method for protein analysis," *Anal. Biochem.*, vol. 353, no. 2, pp. 157–166, Jun. 2006, doi: 10.1016/j.ab.2006.03.025.

[40] R. A. Halvorson and P. J. Vikesland, "Drop Coating Deposition Raman (DCDR) for Microcystin-LR Identification and Quantitation," *Environ. Sci. Technol.*, vol. 45, no. 13, pp. 5644–5651, Jul. 2011, doi: 10.1021/es200255y.

[41] P. Šimáková, E. Kočišová, and M. Procházka, "'Coffee Ring' Effect of Ag Colloidal Nanoparticles Dried on Glass: Impact to Surface-Enhanced Raman Scattering (SERS)," *J. Nanomater.*, vol. 2021, p. e4009352, Aug. 2021, doi: 10.1155/2021/4009352.

[42] Y. Li, H. Lin, Q. He, C. Zuo, M. Lin, and T. Xu, "Label-Free Detection and Classification of Glaucoma Based on Drop-Coating Deposition Raman Spectroscopy," *Appl. Sci.*, vol. 13, no. 11, Art. no. 11, Jan. 2023, doi: 10.3390/app13116476.

[43] T. Lemma, F. de Barros Souza, C. A. Tellez Soto, and A. A. Martin, “An FT-Raman, FT-IR, and Quantum Chemical Investigation of Stanozolol and Oxandrolone,” *Biosensors*, vol. 8, no. 1, p. 2, Dec. 2017, doi: 10.3390/bios8010002.

[44] A. Roufieda Guerroudj *et al.*, “Exploring Pyrimidine-Based azo Dyes: Vibrational spectroscopic Assignments, TD-DFT Investigation, chemical Reactivity, HOMO-LUMO, ELF, LOL and NCI-RDG analysis,” *Spectrochim. Acta. A. Mol. Biomol. Spectrosc.*, vol. 313, p. 124093, May 2024, doi: 10.1016/j.saa.2024.124093.

[45] J. Vedad, E.-R. E. Mojica, and R. Z. B. Desamero, “Raman spectroscopic discrimination of estrogens,” *Vib. Spectrosc.*, vol. 96, pp. 93–100, May 2018, doi: 10.1016/j.vibspec.2018.02.011.

[46] M. Muniz-Miranda, F. Muniz-Miranda, M. C. Menziani, and A. Pedone, “Can DFT Calculations Provide Useful Information for SERS Applications?,” *Molecules*, vol. 28, no. 2, p. 573, Jan. 2023, doi: 10.3390/molecules28020573.

[47] M. Guo, T. Shi, R. Tian, P. Lu, and T. Pan, “Adsorption behavior of pyridaben on silver surface and detection of pyridaben residues in apple,” *Microchem. J.*, vol. 197, p. 109635, Feb. 2024, doi: 10.1016/j.microc.2023.109635.

[48] T. 8, S. Lebègue, J. Hafner, and J. Ángyán, “Tkatchenko-Scheffler van der Waals correction method with and without self-consistent screening applied to solids,” *Phys. Rev. B*, vol. 87, Feb. 2013, doi: 10.1103/PhysRevB.87.064110.

[49] A. R. Issahaku, M. A. A. Ibrahim, N. Mukelabai, and M. E. S. Soliman, “Intermolecular And Dynamic Investigation of The Mechanism of Action of Reldesemtiv on Fast Skeletal Muscle Troponin Complex Toward the Treatment of Impaired Muscle Function,” *Protein J.*, vol. 42, no. 4, pp. 263–275, 2023, doi: 10.1007/s10930-023-10091-y.

[50] A. Vaidyanathan, M. Mathew, S. Radhakrishnan, C. S. Rout, and B. Chakraborty, “Theoretical Insight on the Biosensing Applications of 2D Materials,” *J. Phys. Chem. B*, vol. 124, no. 49, pp. 11098–11122, Dec. 2020, doi: 10.1021/acs.jpcb.0c08539.

[51] B. Chantaramolee, A. A. B. Padama, H. Kasai, and Y. W. Budhi, “First principles study of N and H atoms adsorption and NH formation on Pd(111) and Pd3Ag(111) surfaces,” *J. Membr. Sci.*, vol. 474, pp. 57–63, Jan. 2015, doi: 10.1016/j.memsci.2014.09.048.

[52] D. C. Sorescu, “Adsorption and activation of CO coadsorbed with K on Fe(100) surface: A plane-wave DFT study,” *Surf. Sci.*, vol. 605, no. 3, pp. 401–414, Feb. 2011, doi: 10.1016/j.susc.2010.11.009.

[53] M. R. Bailey, R. S. Martin, and Z. D. Schultz, “Role of Surface Adsorption in the Surface-Enhanced Raman Scattering and Electrochemical Detection of Neurotransmitters,” *J. Phys. Chem. C Nanomater. Interfaces*, vol. 120, no. 37, pp. 20624–20633, Sep. 2016, doi: 10.1021/acs.jpcc.6b01196.

[54] X.-M. Wang, X. Li, W.-H. Liu, C.-Y. Han, and X.-L. Wang, “Gas Sensor Based on Surface Enhanced Raman Scattering,” *Materials*, vol. 14, no. 2, p. 388, Jan. 2021, doi: 10.3390/ma14020388.

[55] T. Zhang *et al.*, “Clarifying the Adsorption of Triphenylamine on Au(111): Filling the HOMO–LUMO Gap,” *J. Phys. Chem. C Nanomater. Interfaces*, vol. 126, no. 3, pp. 1635–1643, Jan. 2022, doi: 10.1021/acs.jpcc.1c08877.

[56] P. Zheng, H. Tang, B. Liu, S. Kasani, L. Huang, and N. Wu, “Origin of strong and narrow localized surface plasmon resonance of copper nanocubes,” *Nano Res.*, vol. 12, no. 1, pp. 63–68, Jan. 2019, doi: 10.1007/s12274-018-2178-6.

[57] K.-A. N. Duerloo, Y. Li, and E. J. Reed, “Structural phase transitions in two-dimensional Mo- and W-dichalcogenide monolayers,” *Nat. Commun.*, vol. 5, no. 1, p. 4214, Jul. 2014, doi: 10.1038/ncomms5214.

[58] L. Song *et al.*, “Amplifying the signal of localized surface plasmon resonance sensing for the sensitive detection of Escherichia coli O157:H7,” *Sci. Rep.*, vol. 7, no. 1, Art. no. 1, Jun. 2017, doi: 10.1038/s41598-017-03495-1.

[59] L. Buimaga-Iarinca and C. Morari, “Translation of metal-phthalocyanines adsorbed on Au(111): from van der Waals interaction to strong electronic correlation,” *Sci. Rep.*, vol. 8, Aug. 2018, doi: 10.1038/s41598-018-31147-5.

[60] M. Shukla, A. Verma, S. Kumar, S. Pal, and I. Sinha, “Experimental and DFT calculation study of interaction between silver nanoparticle and 1-butyl-3-methyl imidazolium tetrafluoroborate ionic liquid,” *Heliyon*, vol. 7, no. 1, p. e06065, Jan. 2021, doi: 10.1016/j.heliyon.2021.e06065.

[61] S. Cong, X. Liu, Y. Jiang, W. Zhang, and Z. Zhao, “Surface Enhanced Raman Scattering Revealed by Interfacial Charge-Transfer Transitions,” *The Innovation*, vol. 1, no. 3, p. 100051, Oct. 2020, doi: 10.1016/j.xinn.2020.100051.

[62] C. Muehlethaler, C. R. Considine, V. Menon, W.-C. Lin, Y.-H. Lee, and J. R. Lombardi, “Ultrahigh Raman Enhancement on Monolayer MoS2,” *ACS Photonics*, vol. 3, no. 7, pp. 1164–1169, Jul. 2016, doi: 10.1021/acsphotonics.6b00213.

[63] N. A. Wazzan, “DFT calculations of thiosemicarbazide, arylisothiocynates, and 1-aryl-2,5-dithiohydrazodicarbonamides as corrosion inhibitors of copper in an aqueous chloride solution,” *J. Ind. Eng. Chem.*, vol. 26, Dec. 2014, doi: 10.1016/j.jiec.2014.11.043.

6 General Conclusions and Future Studies

6.1 General Conclusions

This chapter concludes the entire thesis, explaining how each of the chapters in the results and discussions contribute to the overall goal and specific objectives of the research. Generally, the thesis aimed at exploring the feasibility of vibrational-spectroscopy-based analysis and localized surface plasmon resonance aided by density functional theory in the label-free detection of trenbolone acetate.

The first part of the results explored the role of laser ablation in liquid technique in synthesizing silver nanoparticles. The work demonstrated that it is possible to fabricate silver nanoparticles of different sizes (within the range of 10nm – 54nm) by varying different ablation parameters such as laser ablation time, energy, and pulse repetition frequency. The small nanoparticles generated in the work showed that it is possible to leverage laser ablation to synthesize nanoparticles with high surface area, providing remarkable adsorption tendencies suitable for biosensing applications. Besides the yellowish-brown color that is proof of generated nanoparticles, spectroscopic and electronic techniques were also used to study the nanoparticles, showing that objective one of this work was successfully achieved and the generated nanoparticles could effectively be applied in subsequent analytical studies.

The second set of results investigated the role of localized surface plasmon resonance spectroscopy in the detection of trenbolone acetate and by extension, other anabolic steroids. Silver nanoparticle plasmonic behavior was monitored using UV-VIS spectroscopy. It was observed that the plasmon band of silver nanoparticles red-shifts after the adsorption of trenbolone acetate. The LSPR band position varied inversely and exponentially with the concentration of trenbolone acetate. The change in the plasmon band was monitored to concentrations as less as 5ppm of the analyte. Besides the shift in plasmon band position, the bandwidth of the analyte/ nanoparticle complex was monitored. The results showed that trenbolone acetate adsorbs on the silver nanoparticles' core shell as depicted in the change in concentration of the mixture as monitored using energy dispersive spectroscopy. The change in the plasmon band at low concentrations showed the ability of localized surface plasmon resonance spectroscopy to detect low-analyte concentrations through the influence of refractive index and change in the dielectric field of the local environment. The results showed that the goal of the second objective was achieved.

Surface-enhanced Raman spectroscopy as a label-free analytical technique was also investigated in this study. Silver nanoparticles were used as substrates providing a localized electromagnetic field that enhanced the signal. Together with other vibrational techniques like FTIR and drop-coating deposition Raman, the trenbolone molecule was characterized. Density functional theory and vibrational energy density distribution (VEDA) proved to be effective tools in understanding the vibrational spectra of trenbolone acetate. To the best of our knowledge, this was pioneer research that provided molecular information about trenbolone acetate. In the fight against doping, the results are critical since they aid in building a spectral library that can be leveraged by the World Anti-doping Agency (WADA) in building a spectroscopy-based analytical laboratory in its anti-doping efforts. The characteristic assignment and functional groups specific to this molecule also form the basis for further research on steroids abused in sports.

The adsorption tendency of trenbolone acetate on silver nanoparticles was also evaluated with the help of SERS and the study of frontier molecular orbitals. The energy band gap obtained through the highest occupied molecular orbital (HOMO) and lowest unoccupied molecular orbital (LUMO) studies based on DFT showed that chemical potential energy is lower than the band gap energy demonstrating the ease with which the molecule can engage in chemical reaction. The DFT study showed that negatively charged oxygen molecule is the most active site that would allow the adsorption of silver nanoparticles. Electronegativity and electron affinity studies showed that trenbolone would easily donate its oxygen atom for a chemical reaction. In the molecule, the functional group responsible for the reaction is C=O which is within the wavenumber 1620cm^{-1} and 1750cm^{-1}. This region was the most active and would easily engage in reaction with silver. The Ag+ (proven using LIBS) would easily react with the oxygen to form a complex that influences both plasmon behavior and SERS behavior in terms of wavenumber shifts. The ketone group located in the acetate ester part is thus responsible for the drug's pharmacological activity, providing insights into the steps that WADA has to take when investigating the drug's doping tendency.

6.2 Future Studies

Future work for this study will focus on building and commercializing a novel prototype biosensor for detecting steroids and other performance-enhanced drugs based on the knowledge of localized surface plasmon resonance, surface-enhanced Raman/vibrational techniques, and the adhesion tendency of the analyte on silver nanoparticles. The biosensor will allow not only the detection but also quantification of performance-enhancement drugs with better sensitivity.

To achieve this goal, improved theoretical studies of drug/nanoparticle complexes will be achieved with the help of molecular dynamics (MD). MD simulations will provide better insights into the dynamic behavior of biomolecules and how they interact with the nanoparticles that are relevant to biosensing. MD simulations can predict how biomolecules recognize and bind to specific targets, aiding in the design of biosensors with high specificity and sensitivity by elucidating the molecular recognition processes. Other studies like surface interactions and the binding energies of the molecule on nanoparticles will also be understood better with the help of molecular dynamics.

Molecular dynamics will also come in handy in improving the sensitivity and selectivity of a biosensor, especially by elucidating structural changes of the molecule upon adsorbing on the nanoparticles. While knowledge of the localized surface plasmon resonance, molecular characterization, and signal enhancement tendency using SERS has already been demonstrated in this thesis, building a biosensor prototype will require knowledge of molecular dynamics.